Atlas of Formability

AD-A268 354

Haynes 556

DTIC
ELECTE
AUG 18 1993
S B D

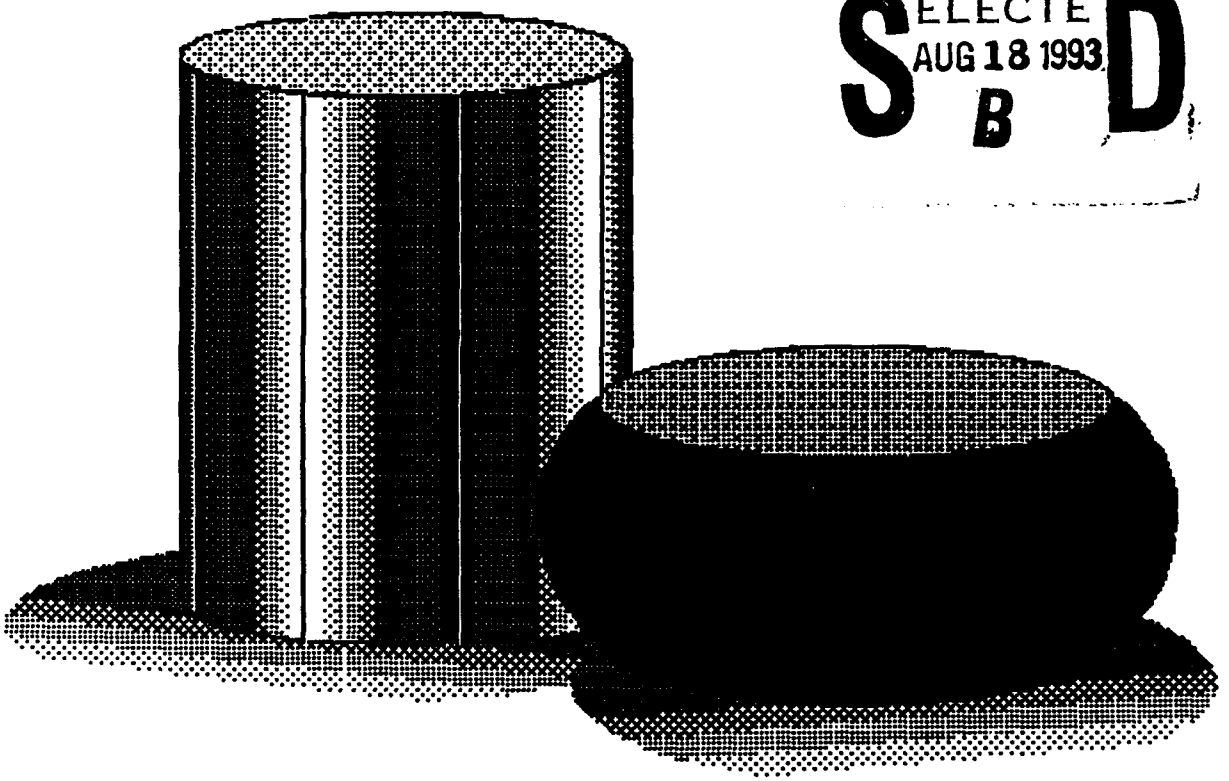

DISTRIBUTION STATEMENT A
Approved for public release;
Distribution Unlimited

NCEMT

93-18964

DISCLAIMER NOTICE

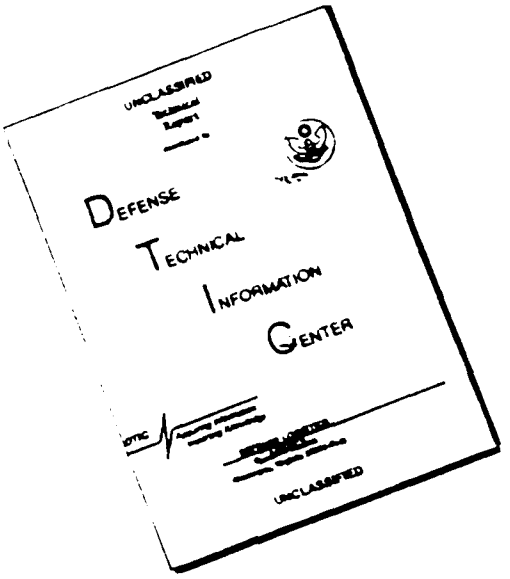

THIS DOCUMENT IS BEST QUALITY AVAILABLE. THE COPY FURNISHED TO DTIC CONTAINED A SIGNIFICANT NUMBER OF PAGES WHICH DO NOT REPRODUCE LEGIBLY.

ATLAS OF FORMABILITY

HAYNES 556

by

Prabir K. Chaudhury and Dan Zhao

National Center for Excellence in Metalworking Technology
1450 Scalp Avenue
Johnstown, PA 15904

for

Naval Industrial Resource Support Activity
Building 75-2, Naval Base
Philadelphia, PA 19112-5078

January 29, 1993

The views, opinions, and/or findings contained in this report are those of the authors and should not be construed as an official Department of the Navy position, policy, or decision, unless so designated by other documentation

REPORT DOCUMENTATION PAGE

Form Approved
OMB No. 0704-0188

Public reporting burden for this collection of information is estimated to average 1 hour per response, including the time for reviewing instructions, searching existing data sources, gathering and maintaining the data needed, and completing and reviewing the collection of information. Send comments regarding this burden estimate or any other aspect of this collection of information, including suggestions for reducing this burden, to Washington Headquarters Services, Directorate for information Operations and Reports, 1215 Jefferson Davis Highway, Suite 1204, Arlington, VA 22202-4302, and to the Office of Management and Budget, Paperwork Reduction Project (0704-0188), Washington, DC 20503.

1. AGENCY USE ONLY (Leave blank)	2. REPORT DATE	3. REPORT TYPE AND DATES COVERED
	January 29, 1993	Final, October 31, 1992 - January 29, 1993

4. TITLE AND SUBTITLE

ATLAS OF FORMABILITY
HAYNES 556

5. FUNDING NUMBERS

C-N00140-88-C-RC21

6. AUTHOR(S)

Prabir K. Chaudhury
Dan Zhao

7. PERFORMING ORGANIZATION NAME(S) AND ADDRESS(ES)

National Center for Excellence in Metalworking Technology (NCEMT)
1450 Scalp Avenue
Johnstown, PA 15904

8. PERFORMING ORGANIZATION REPORT NUMBER

9. SPONSORING/MONITORING AGENCY NAME(S) AND ADDRESS(ES)

Naval Industrial Resources Support Activity
Building 75-2, Naval Base
Philadelphia, PA 19112-5078

10. SPONSORING/MONITORING AGENCY REPORT NUMBER

11. SUPPLEMENTARY NOTES

12a. DISTRIBUTION/AVAILABILITY STATEMENT

12b. DISTRIBUTION CODE

13. ABSTRACT *(Maximum 200 words)*

In this investigation, flow behavior of Haynes 556 alloy was studied by conducting compression tests over a wide range of temperatures (950 - 1200 C) and strain rates (0.001 - 20 s^{-1}). The true stress-true strain flow curves are presented for each test conditions. Constitutive relations were determined from the flow behavior, and a dynamic material modeling was performed on this alloy. Thus, the optimum processing condition in terms of temperature and strain rate was identified as 1125 C and 0.001 s^{-1} for this alloy. Microstructural changes during high temperature deformation were also characterized, and selective micrographs are presented together with corresponding flow curves. Dynamic recrystallization and grain growth occurred during high temperature deformation over the range of temperatures tested. This report supplies ample mechanical property and microstructure data on Haynes 556 alloy for mechanical and materials engineers in the field of metalworking process design. The data presented here are also very helpful in finite element analysis of metalworking processes.

14. SUBJECT TERMS

Haynes 556, Deformation Processing, High Temperature Deformation, Processing Map, Metalworking, Microstructure

15. NUMBER OF PAGES

68

16. PRICE CODE

17. SECURITY CLASSIFICATION OF REPORT	18. SECURITY CLASSIFICATION OF THIS PAGE	19. SECURITY CLASSIFICATION OF ABSTRACT	20. LIMITATION OF ABSTRAC
Unclassified	Unclassified	Unclassified	

TABLE OF CONTENTS

Introduction 1

Experimental Procedure 1

Results 1

Summary 64

Implenmentation of Data Provided by the Atlas of Formability 64

ST #A, AUTH USNAVIRSA (MR PLONSKY 8/443-6684)
PER TELECON, 17 AUG 93 CB

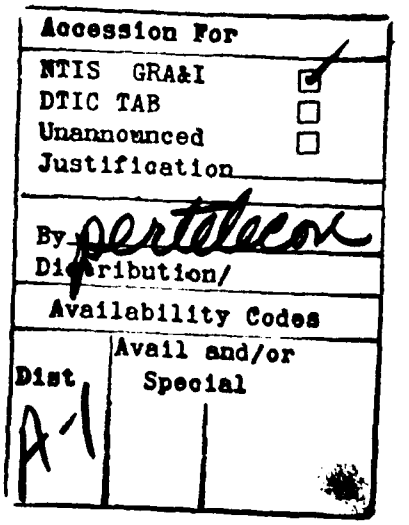

DTIC QUALITY INSPECTED 8

LIST OF TABLE

Table 1. List of figures, testing conditions and microstructural observations for Haynes 566 2

Haynes 556

Introduction

Haynes 556 alloy has good oxidation resistance, fabricability, excellent high-temperature strength and effective resistance to sulfidizing, carburizing and chlorine-bearing environments at high temperatures. The understanding of mechanical and microstructural behavior during high temperature deformation is very important for the forming processes of this material. In this investigation, flow behavior of Haynes 556 was studied by conducting compression tests over a range of temperatures and strain rates. Constitutive relations were determined from the flow behavior and a dynamic material modeling for this alloy was performed. Thus, the optimum processing condition in terms of temperature and strain rate was determined. Microstructural changes during high temperature deformation were also characterized to aid process design engineers to select processing conditions which results in desired microstructure.

Experimental Procedure

The material used in this investigation was commercially available Haynes 556 wrought bars with about 15 mm diameter in annealed condition. The typical microstructure of the as-received material consists of equiaxed grains with an average grain size of 45.3 μm and much twinning as shown in Figure 1. The chemical composition is as follows (wt%, bal. Fe):

C	S	Mn	Si	Cr	B	Al	Co	Ni
0.10	<.003	0.93	0.39	21.89	<.002	0.16	18.04	22.07

W	Zr	Ta	Mo	N	Cb	La	P
2.28	0.014	0.61	2.79	0.17	0.10	0.049	<.007

Cylindrical compression test specimens with a diameter of 12.7 mm and a height of 15.9 mm were machined from the bars. Isothermal compression tests were conducted in vacuum to a true strain of 0.8 on an MTS testing machine. The test matrix was as follows:

Temperature, C (F): 950 (1742), 1000 (1832), 1050 (1922), 1100 (2012), 1150 (2102), 1175 (2147), and 1200 (2192)

Strain rate, s^{-1}: 0.001, 0.01, 0.05, 0.1, 0.5, 1, 5 and 20.

Load and stroke data from the tests were acquired by a computer and later converted to true stress-true strain curves. Immediately after the compression test, the specimens were quenched with forced helium gas in order to retain the deformed microstructure. Longitudinal sections of the specimens were examined by optical microscopy. The photomicrographs presented here were taken from the center of the longitudinal section of the specimens.

Results

Table 1 is a list of the figures, test conditions and the observed microstructures. The true stress-true strain flow curves with selective corresponding deformed microstructure are shown in Figure 2 to Figure 57. True stress versus strain rate was plotted in log-log scale in Figure 58 at a true strain of 0.5. The slope of the plot gives the strain rate sensitivity m, which is not constant over the ranges of strain rate and temperature tested. Log stress vs. 1/T at the same true strain is shown in Figure 59. A processing map at this strain was developed and is shown in Figure 60. The optimum processing condition from the map can be obtained by selecting the temperature and strain rate combination which provides the maximum efficiency in the stable region. This condition is approximately 1106 C and 0.001 s^{-1} for this material.

Table 1. List of figures, testing conditions and microstructural observations for Haynes 556

Figure No	Temperature C (F)	Strain Rate s^{-1}	Microstructure Optical Microscopy	Page No
1	As-received		Equiaxed grains with an average grain size of 45.3 μm, some multiple twins.	4
2	950 (1742)	0.001	Severely deformed grains with very few (~25%) dynamically recrystallized (DRX) grains, some necklacing.	5
3	950 (1742)	0.01		6
4	950 (1742)	0.05		7
5	950 (1742)	0.1	Mostly elongated grains with some necklacing and twinning.	8
6	950 (1742)	0.5		9
7	950 (1742)	1		10
8	950 (1742)	5	Same as above, but with higher amounts of both recrystallized grains and necklacing.	11
9	950 (1742)	20	Same as above, with still higher amounts (~60%) of DRX grains and necklacing.	12
10	1000 (5562)	0.001	~50% DRX equiaxed grains with an average grain size of ~4.5 μm, along with deformed grains with very small amount of necklacing.	13
11	1000 (5562)	0.01	Same as above, but with higher amount (~65%) of recrystallized grains and more necklacing.	14
12	1000 (5562)	0.05		15
13	1000 (5562)	0.1		16
14	1000 (5562)	0.5	Mostly elongated grains (aspect ratio of 1:3) with the onset of necklacing at few grain boundaries, etch pits.	17
15	1000 (5562)	1	Same as above.	18
16	1000 (5562)	5		19
17	1000 (5562)	20	~90% recrystallized very fine subgrains within the deformed original grains.	20
18	1050 (1922)	0.001	~60% recrystallized equiaxed grains with a non-uniform grain size (average ~ 8μm).	21
19	1050 (1922)	0.01		22
20	1050 (1922)	0.05	~50% recrystallized equiaxed subgrains with a non-uniform grain size (average ~7.5μm) within the deformed original grains.	23
21	1050 (1922)	0.1		24
22	1050 (1922)	0.5		25
23	1050 (1922)	1	Same as above, but less amount of subgrains with an average grain size of ~6μm.	26
24	1050 (1922)	5	~90% recrystallized grains, majority (~80%) of which are very fine in size.	27
25	1050 (1922)	20	Same as above, but the proportion of very fine grains is higher (~90%.).	28
26	1100 (1212)	0.001	100% recrystallized equiaxed grains with a wide range of grain size (average size ~28 μm), some twins mostly in larger grains.	29
27	1100 (1212)	0.01	Same as above, with smaller size equiaxed grains, and much less twinning.	30
28	1100 (1212)	0.05		31

29	1100 (1212)	0.1	~100% fine recrystallized grains with an average size of 13.6 μm, some twinning.	32
30	1100 (1212)	0.5		33
31	1100 (1212)	1	~100% recrystallized equiaxed fine grains.	34
32	1100 (1212)	5		35
33	1100 (1212)	20	~100% recrystallized grains with a non-uniform size (average ~9.7 μm), some grain growth.	36
34	1150 (2102)	0.001	100% recrystallized equiaxed grains with larger grain size, twins in some of the larger grains, much more grain growth.	37
35	1150 (2102)	0.01		38
36	1150 (2102)	0.05		39
37	1150 (2102)	0.1		40
38	1150 (2102)	0.5	100% recrystallized equiaxed non-uniform sized grains with multiple twins present in both small and large grains.	41
39	1150 (2102)	1		42
40	1150 (2102)	5	Same as above.	43
41	1150 (2102)	20	Same as above, but less amount of twinning.	44
42	1175 (2147)	0.001	Same as in Figure 34, but with a larger grain size and less amount of twinning.	45
43	1175 (2147)	0.01	~100% recrystallized and grown grains with multiple twins and some fine intragranular precipitates.	46
44	1175 (2147)	0.05	Same as above, but the average grain size is smaller.	47
45	1175 (2147)	0.1		48
46	1175 (2147)	0.5		49
47	1175 (2147)	1	Same as above, but the average grain size is still smaller.	50
48	1175 (2147)	5		51
49	1175 (2147)	20	Similar to Figure 44.	52
50	1200 (2192)	0.001	100% recrystallized and grown grains with an average grain size of ~64 μm.	53
51	1200 (2192)	0.01		54
52	1200 (2192)	0.05		55
53	1200 (2192)	0.1	100% recrystallized and grown grains with an average grain size of 25.9 μm, twins in some grains.	56
54	1200 (2192)	0.5		57
55	1200 (2192)	1	100% recrystallized equiaxed grains with a large grain size variation, very few twins.	58
56	1200 (2192)	5	Same as above, but with less amount of twinning.	59
57	1200 (2192)	20	100% recrystallized equiaxed grains with an average grain size of ~24.6 μm.	60

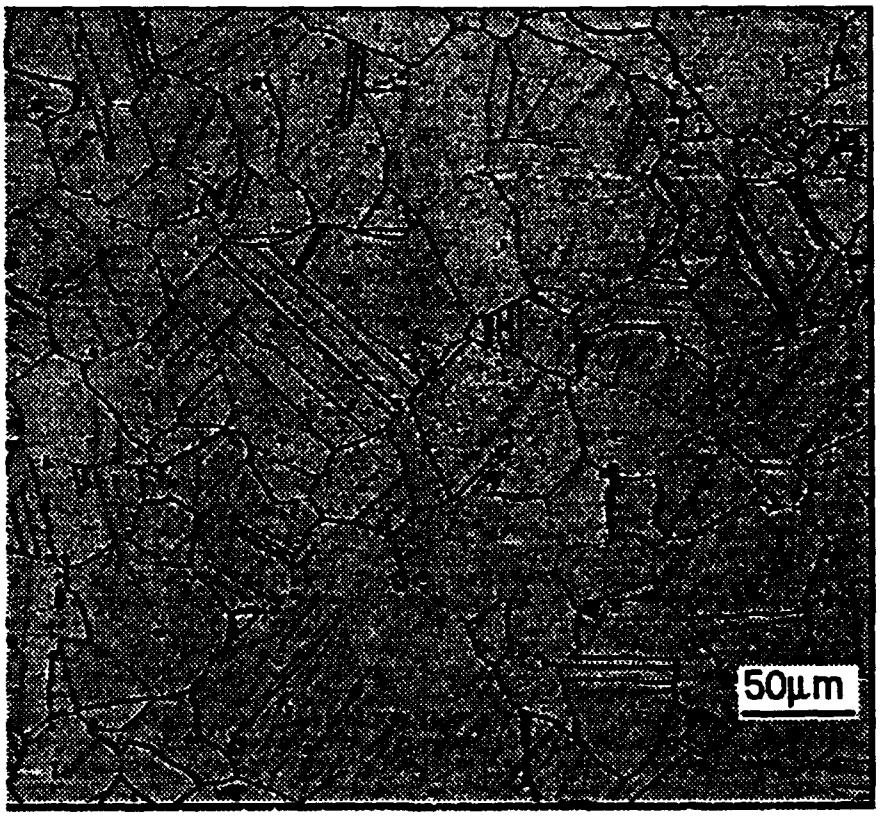

Figure 1. As-received microstructure of Haynes 556.

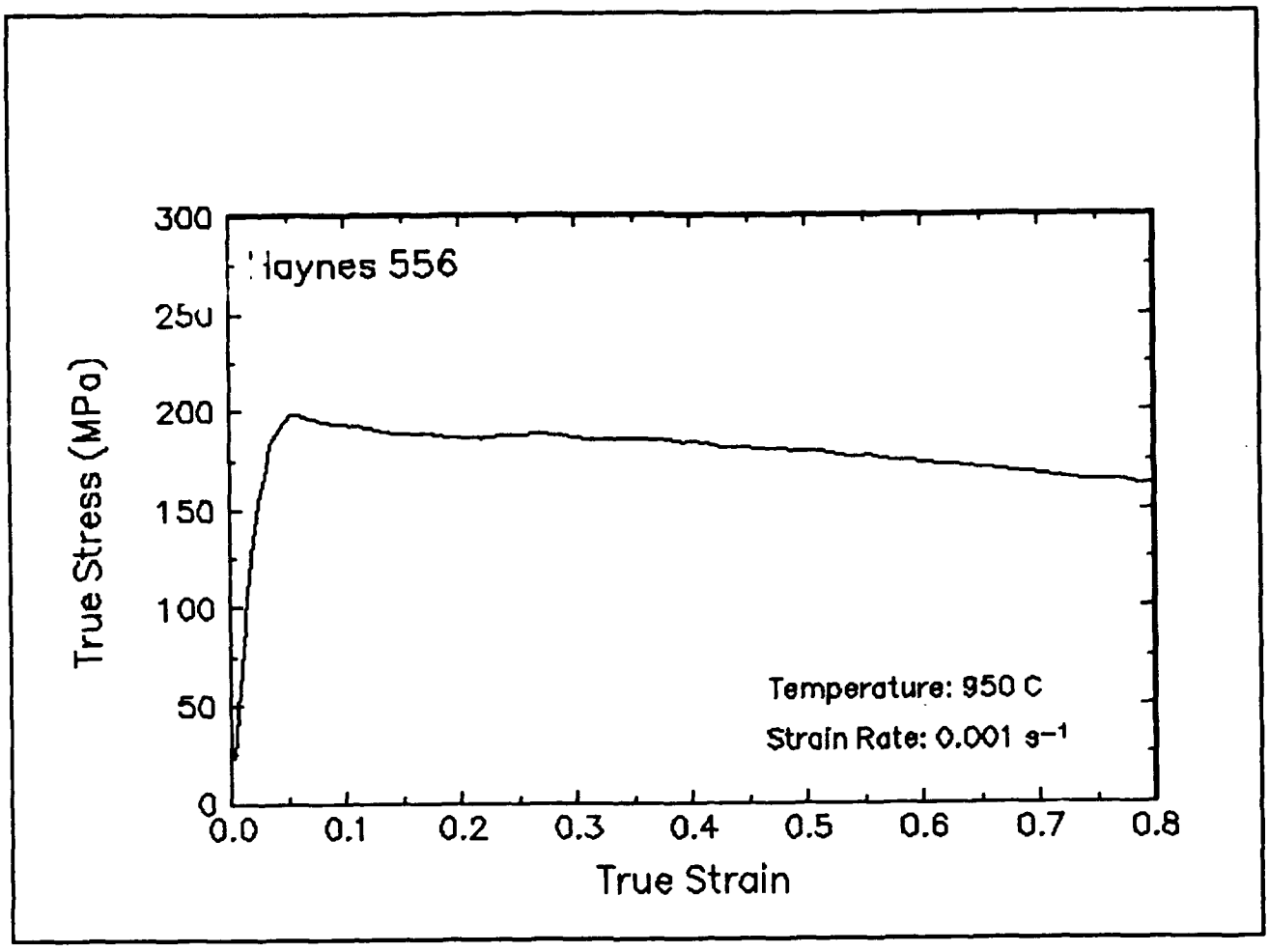

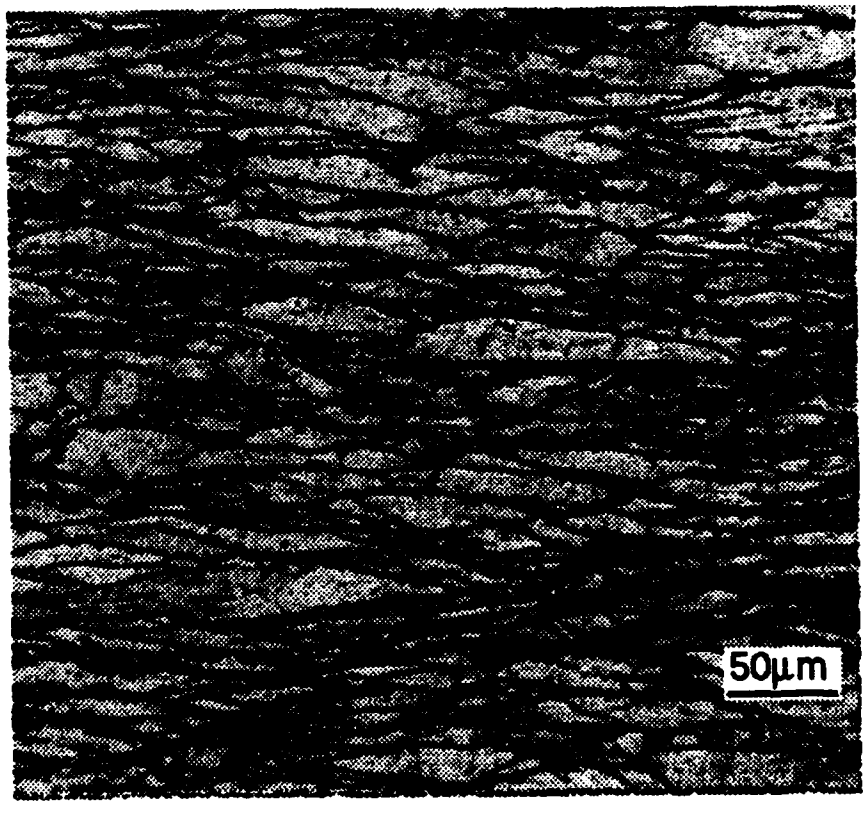

Figure 2. True stress-true strain curve and an optical micrograph from the center of the compressed sample cut through the compression axis, 950 C and 0.001 s^{-1}.

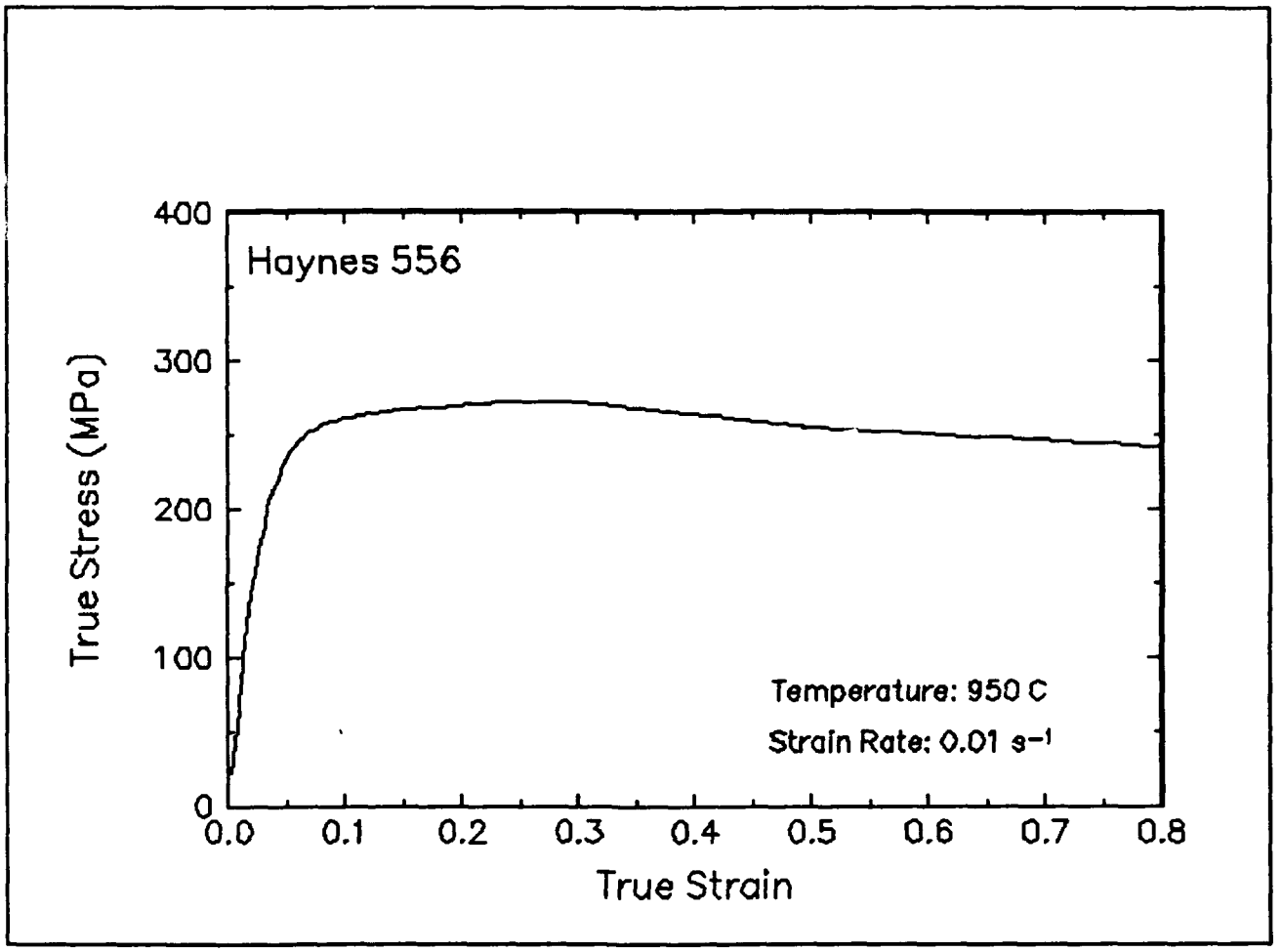

Figure 3. True stress-true strain curve, 950 C and 0.01 s^{-1}.

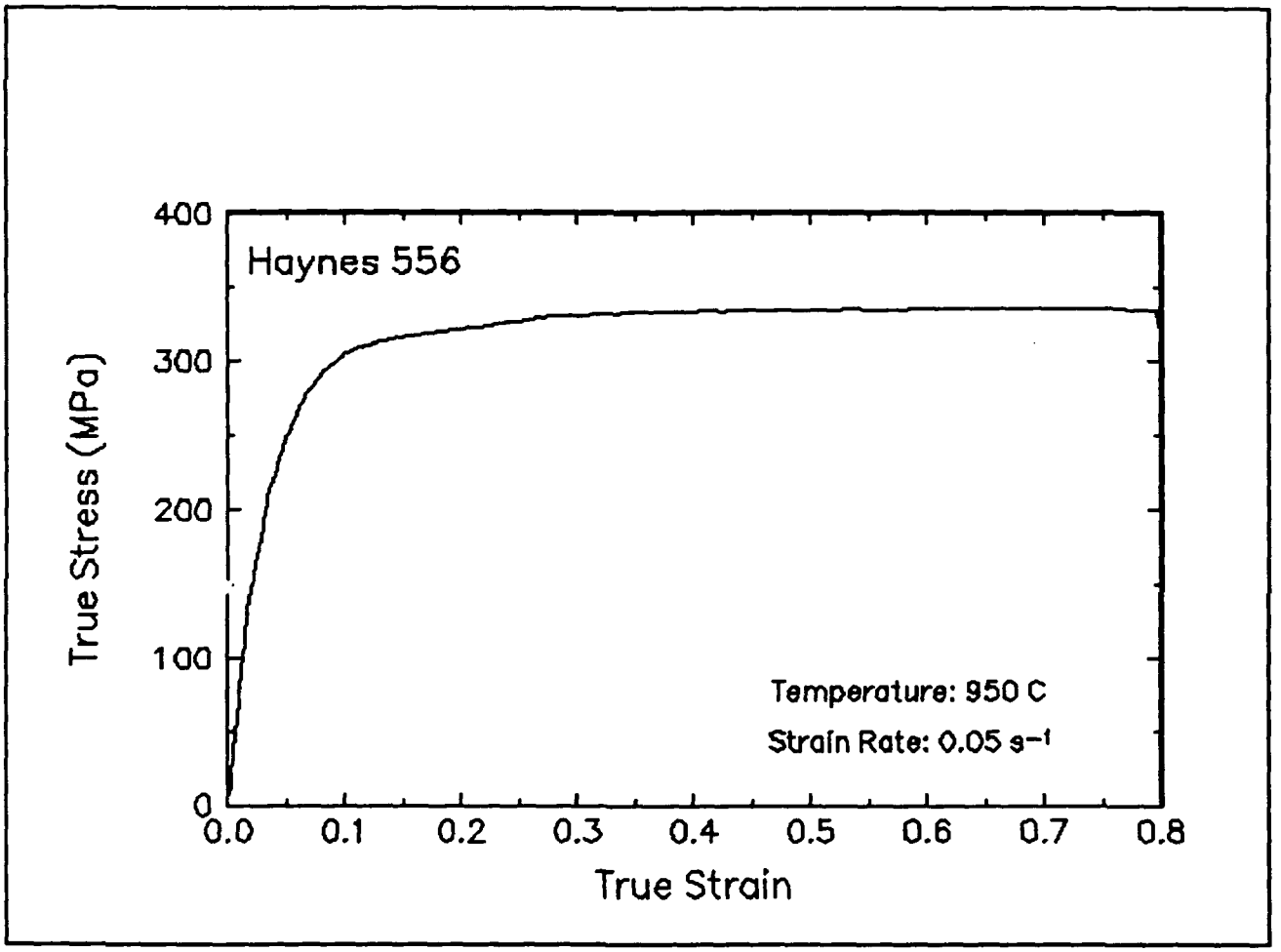

Figure 4. True stress-true strain curve, 950 C and 0.05 s^{-1}.

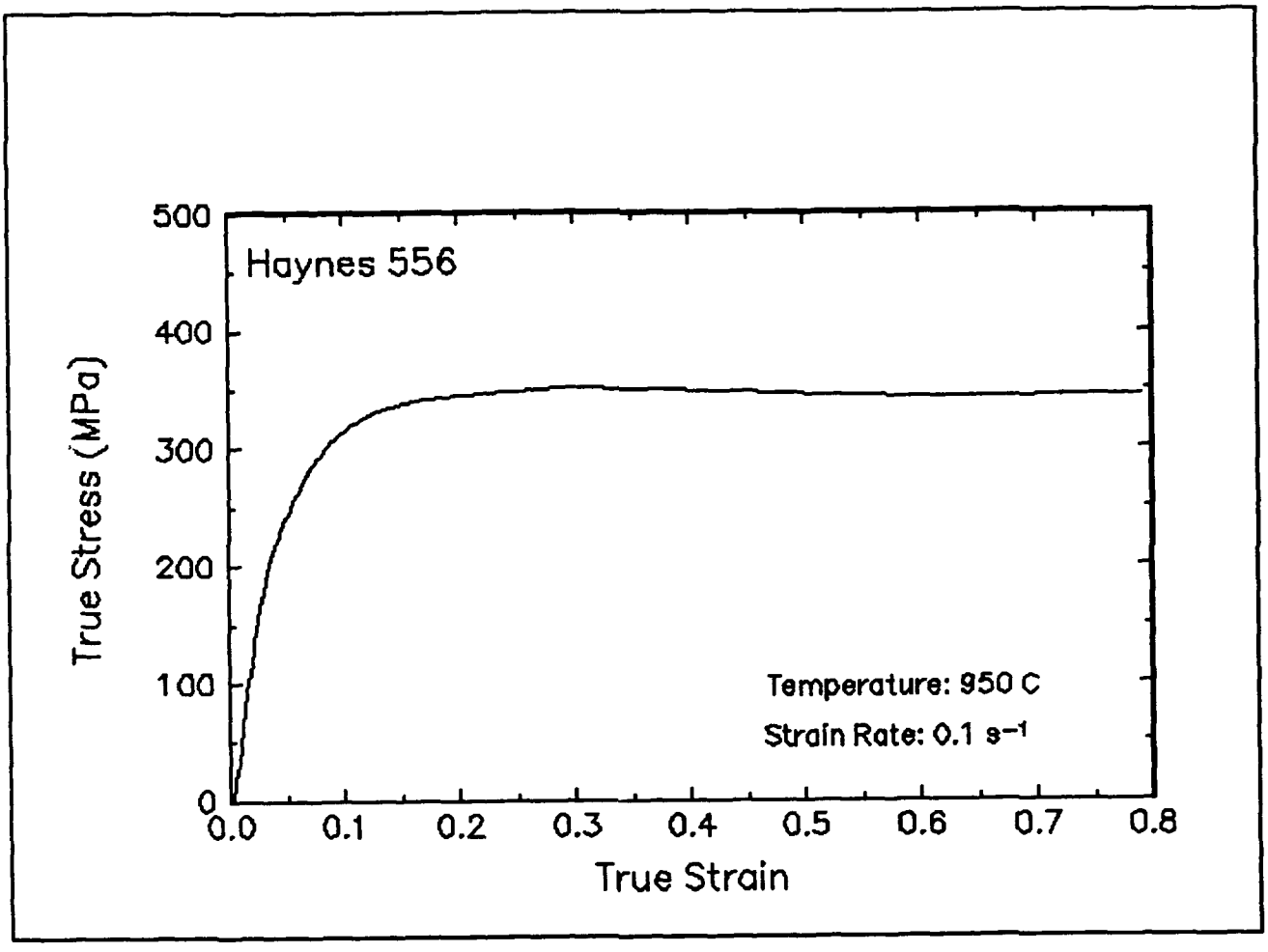

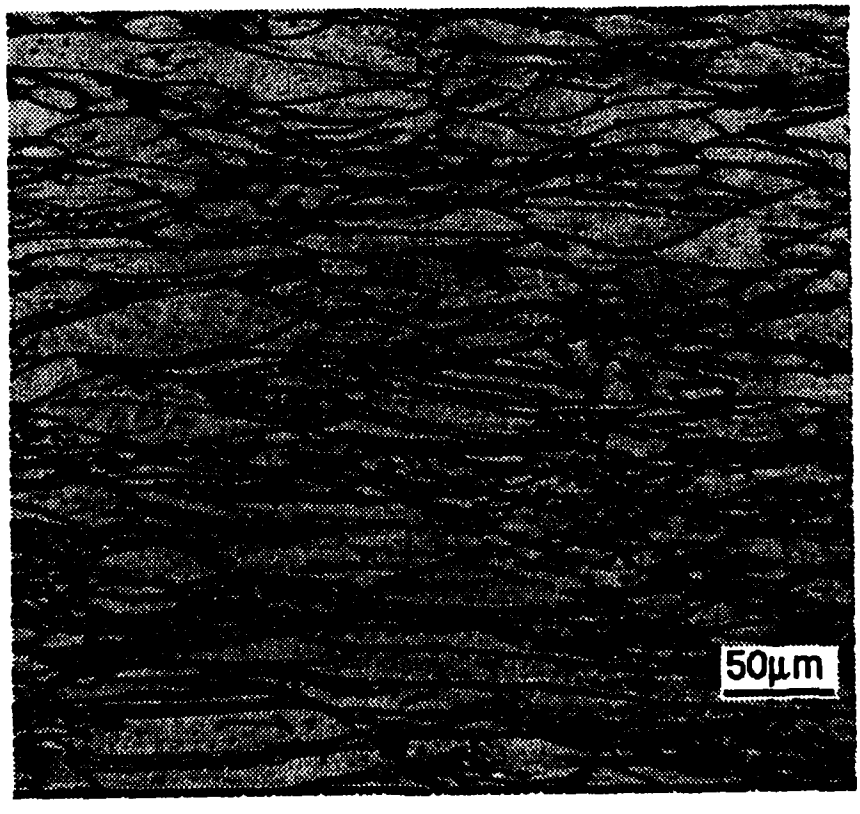

Figure 5. True stress-true strain curve and an optical micrograph from the center of the compressed sample cut through the compression axis, 950 C and 0.1 s^{-1}.

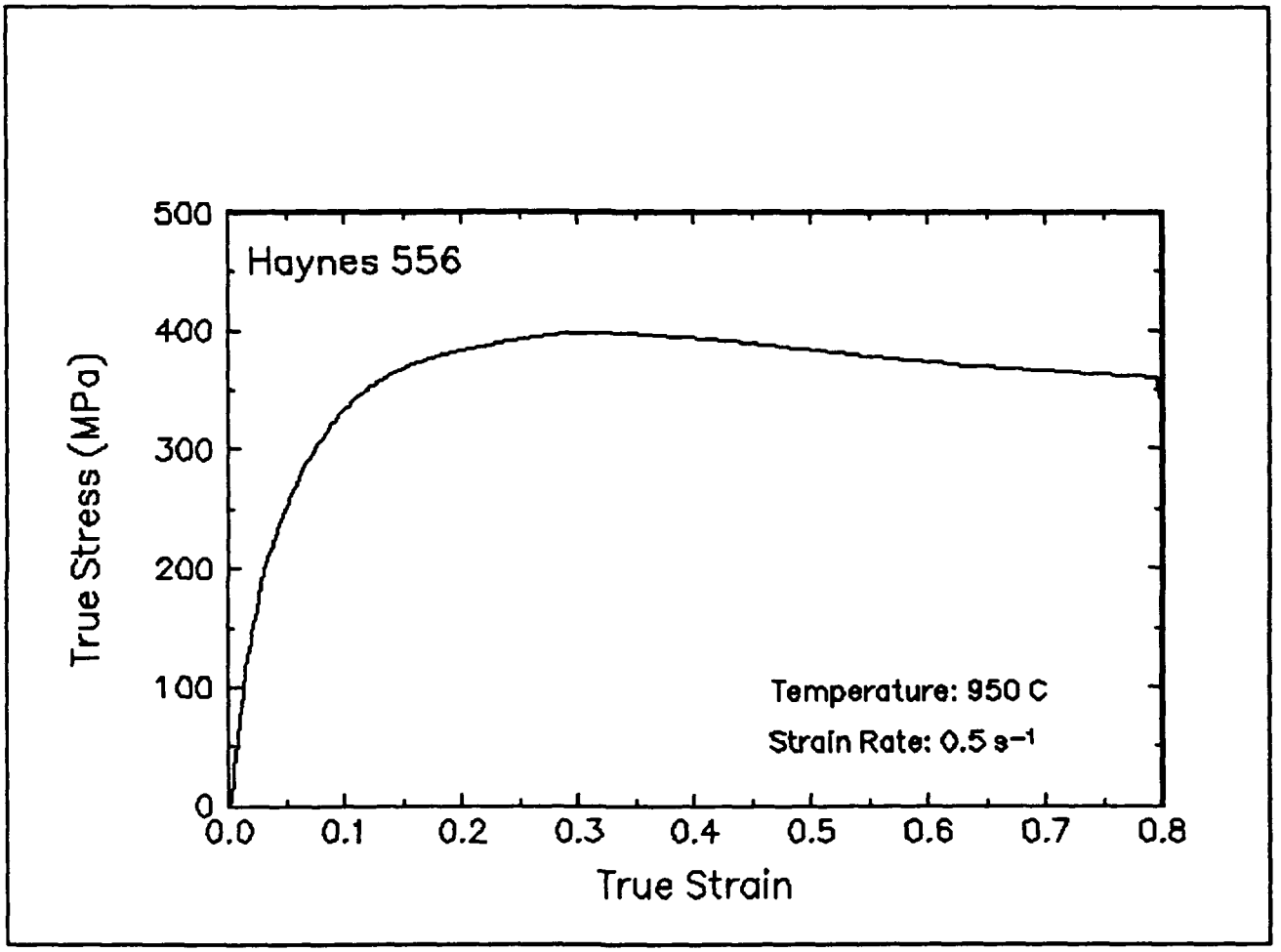

Figure 6. True stress-true strain curve, 950 C and 0.5 s^{-1}.

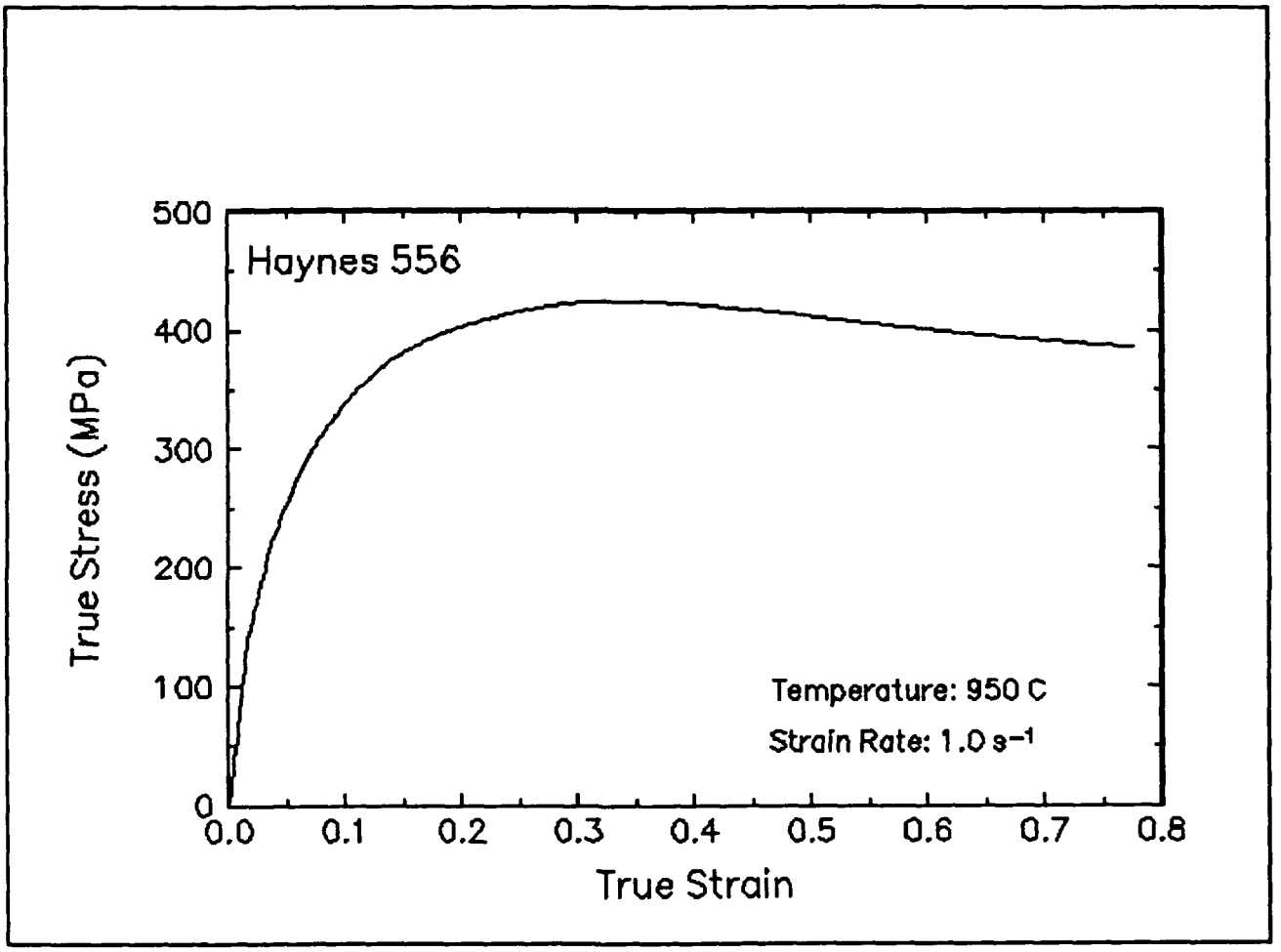

Figure 7. True stress-true strain curve, 950 C and 1 s^{-1}.

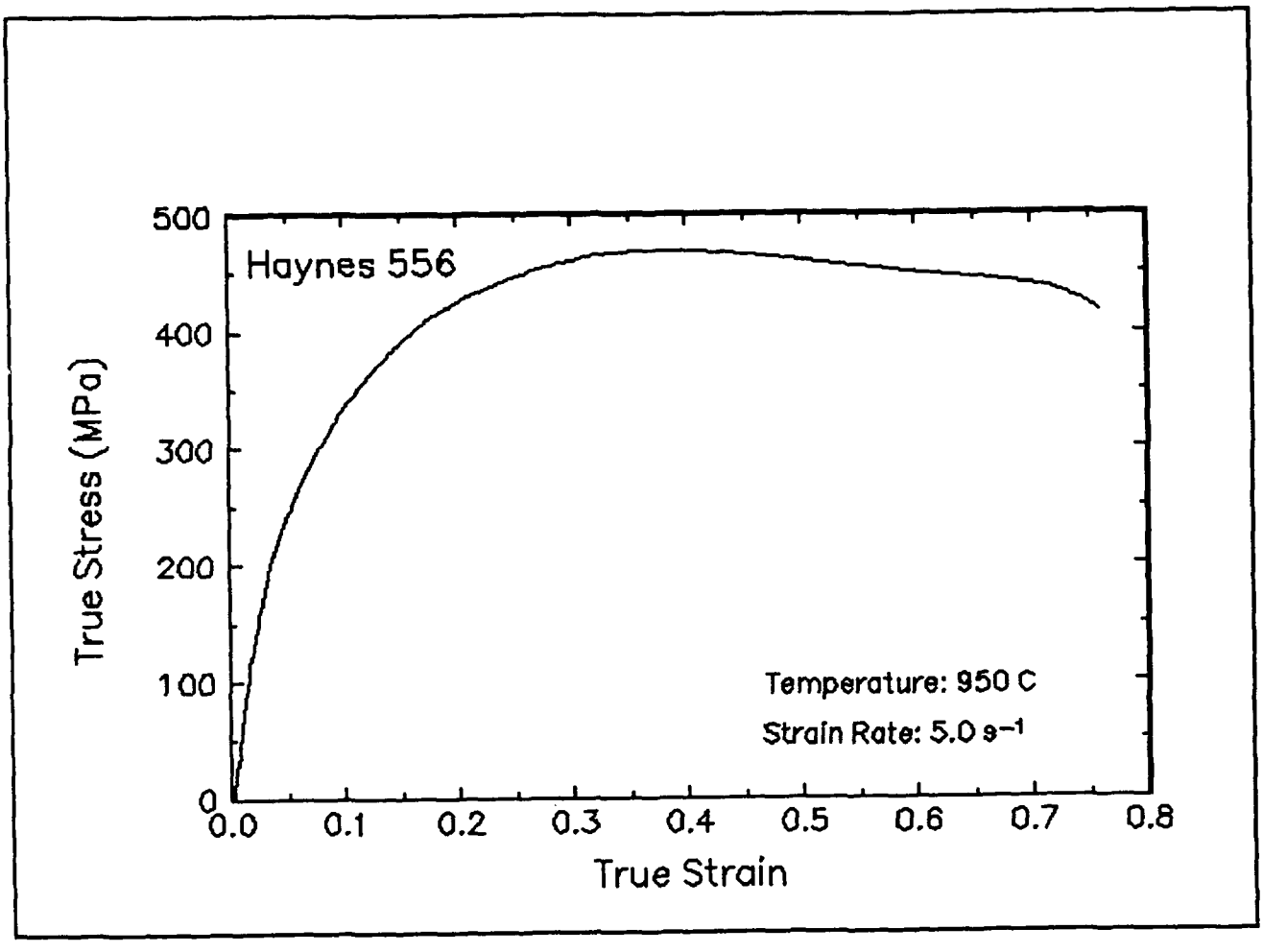

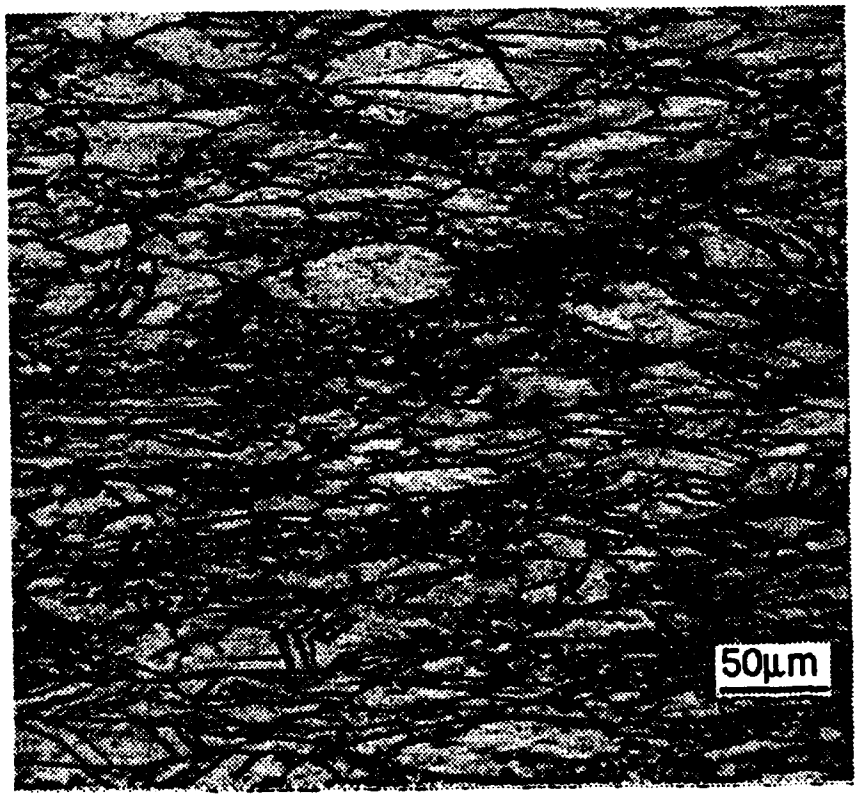

Figure 8. True stress-true strain curve and an optical micrograph from the center of the compressed sample cut through the compression axis, 950 C and 5 s^{-1}.

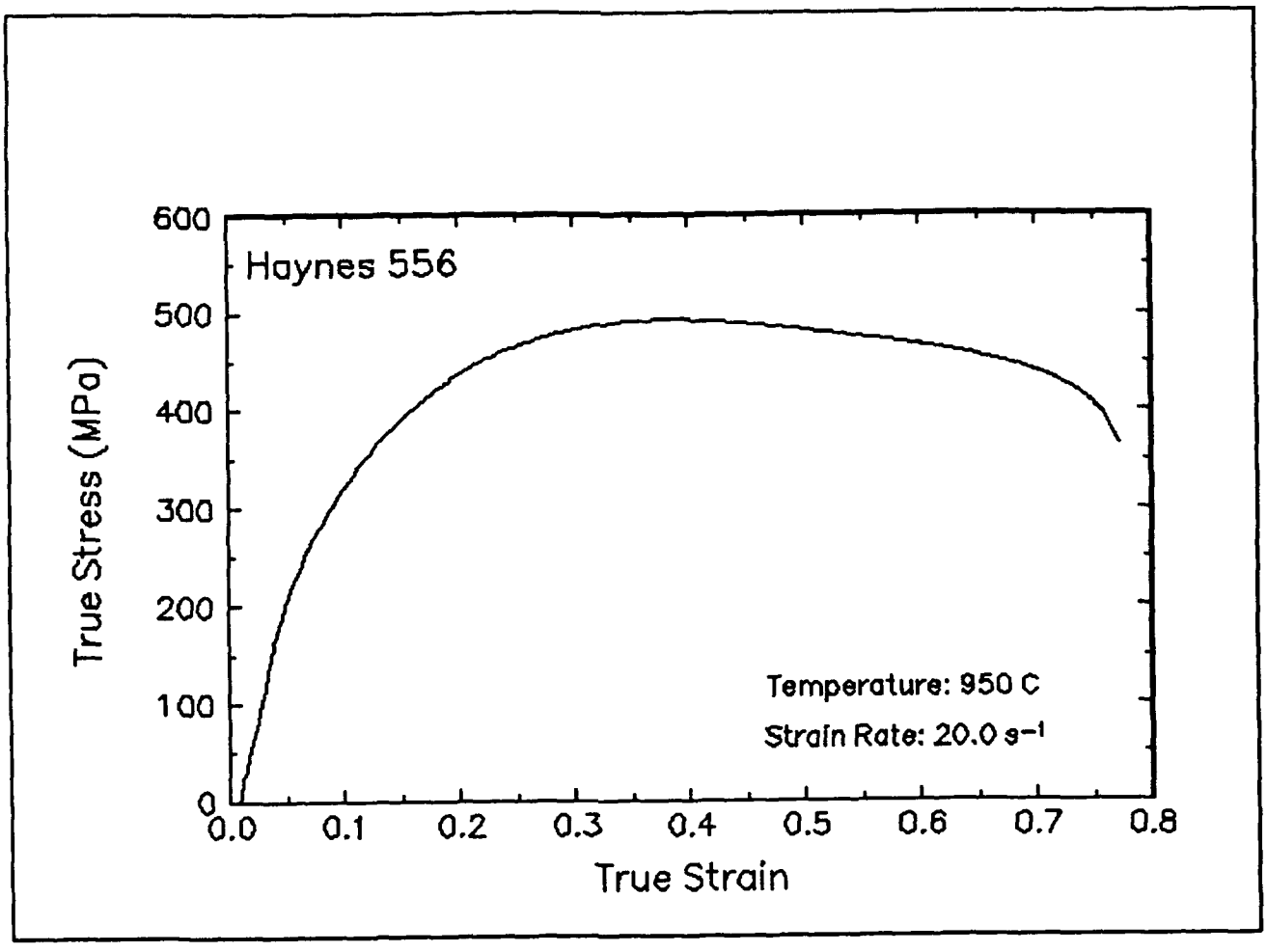

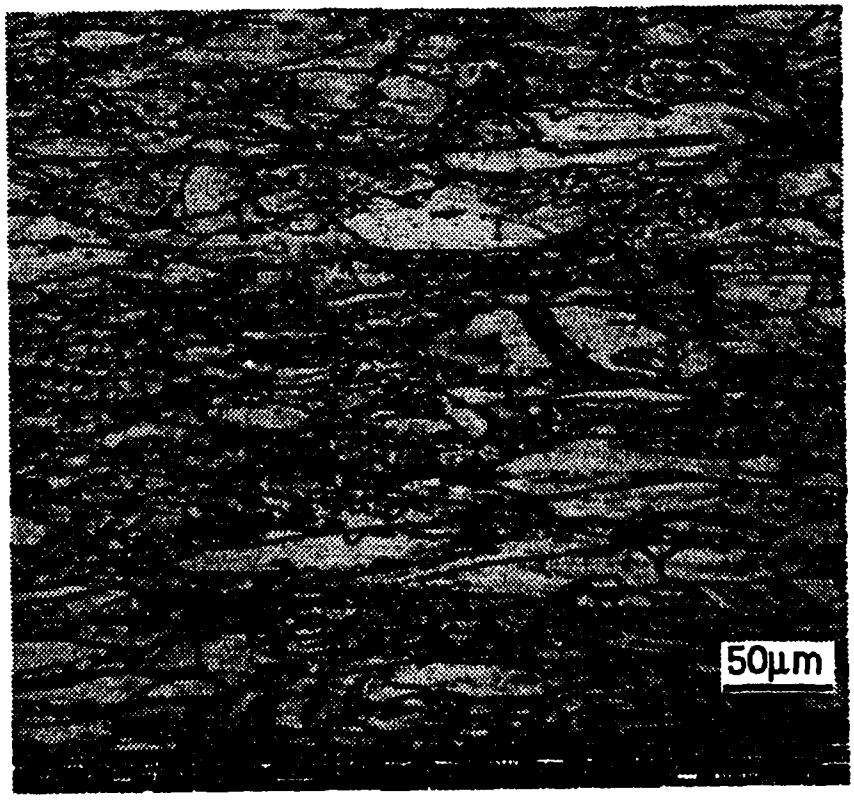

Figure 9. True stress-true strain curve and an optical micrograph from the center of the compressed sample cut through the compression axis, 950 C and 20 s^{-1}.

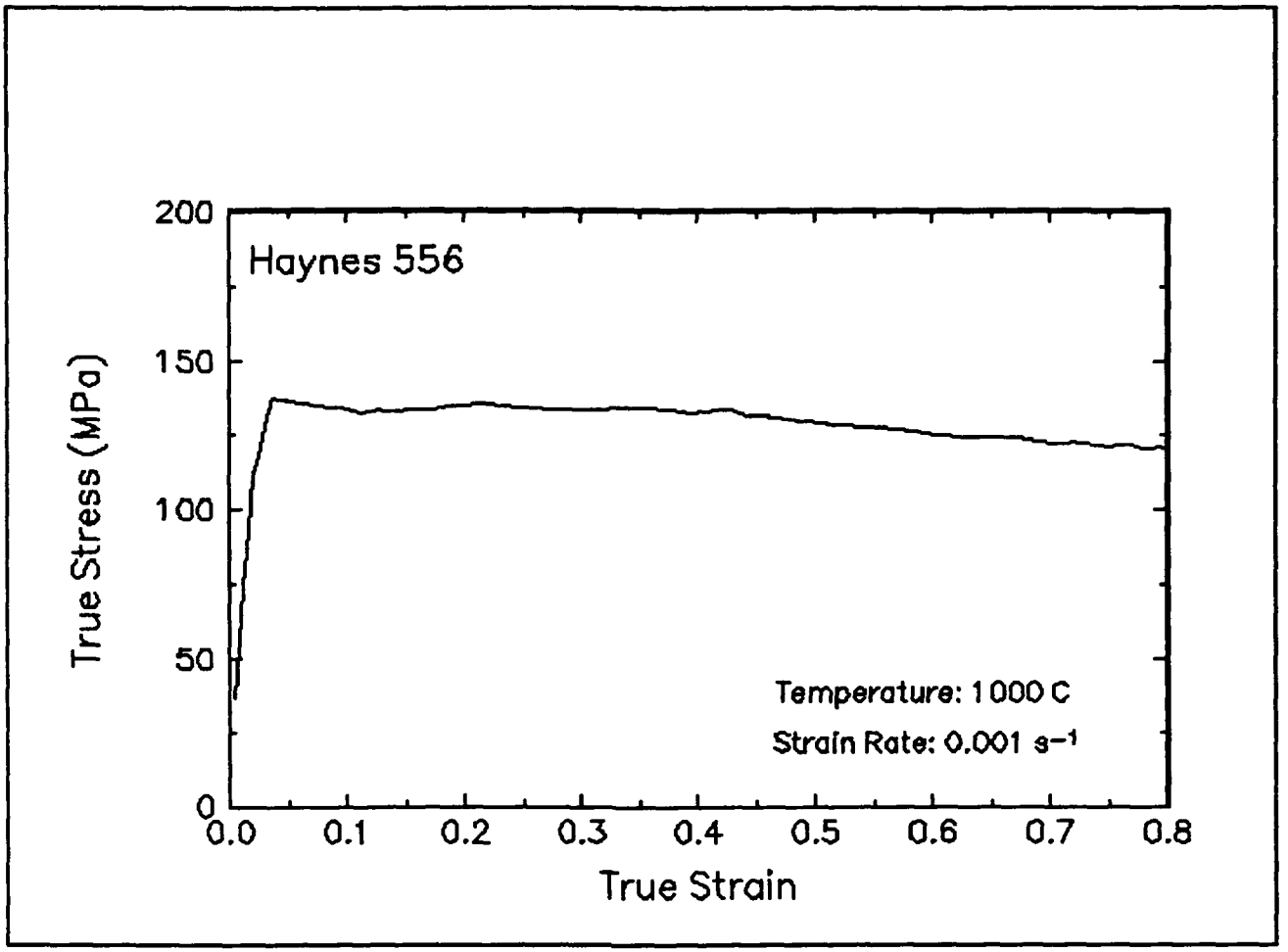

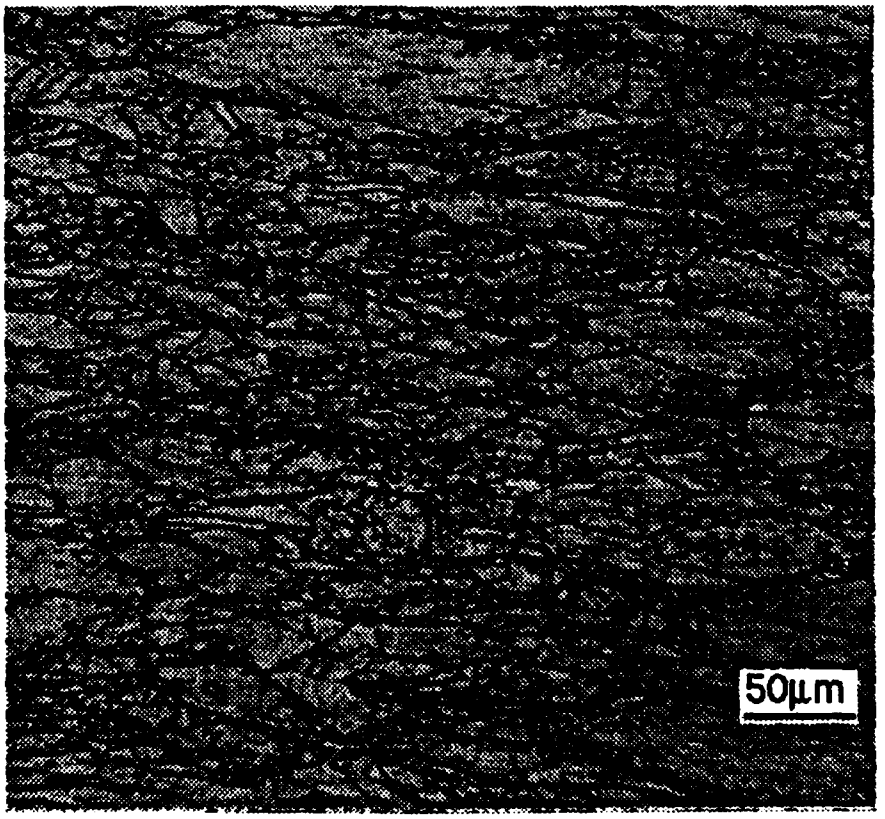

Figure 10. True stress-true strain curve and an optical micrograph from the center of the compressed sample cut through the compression axis, 1000 C and 0.001 s^{-1}.

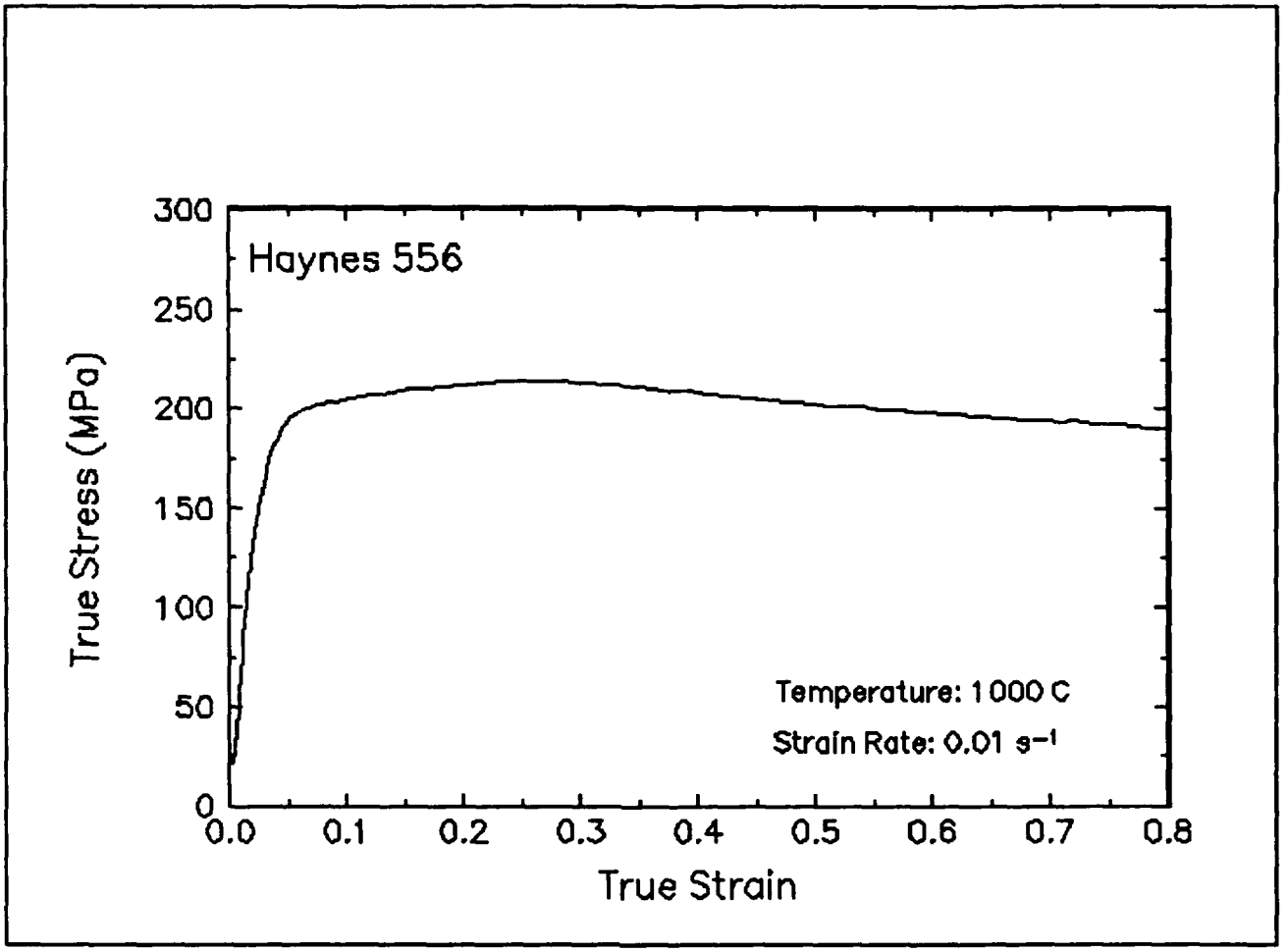

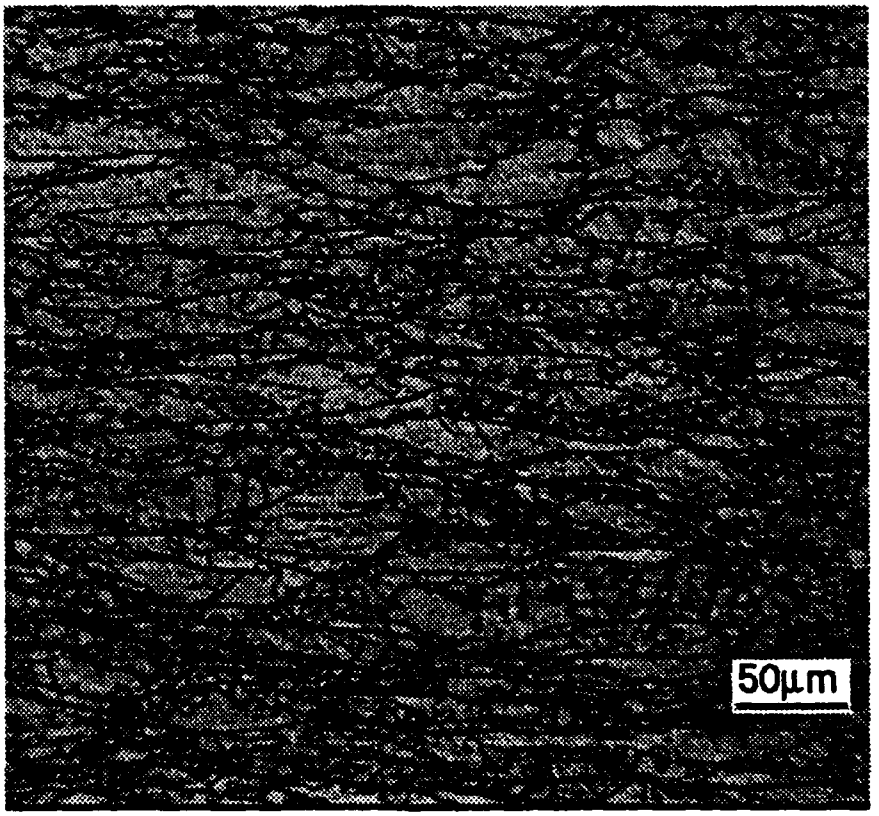

Figure 11. True stress-true strain curve and an optical micrograph from the center of the compressed sample cut through the compression axis, 1000 C and 0.01 s^{-1}.

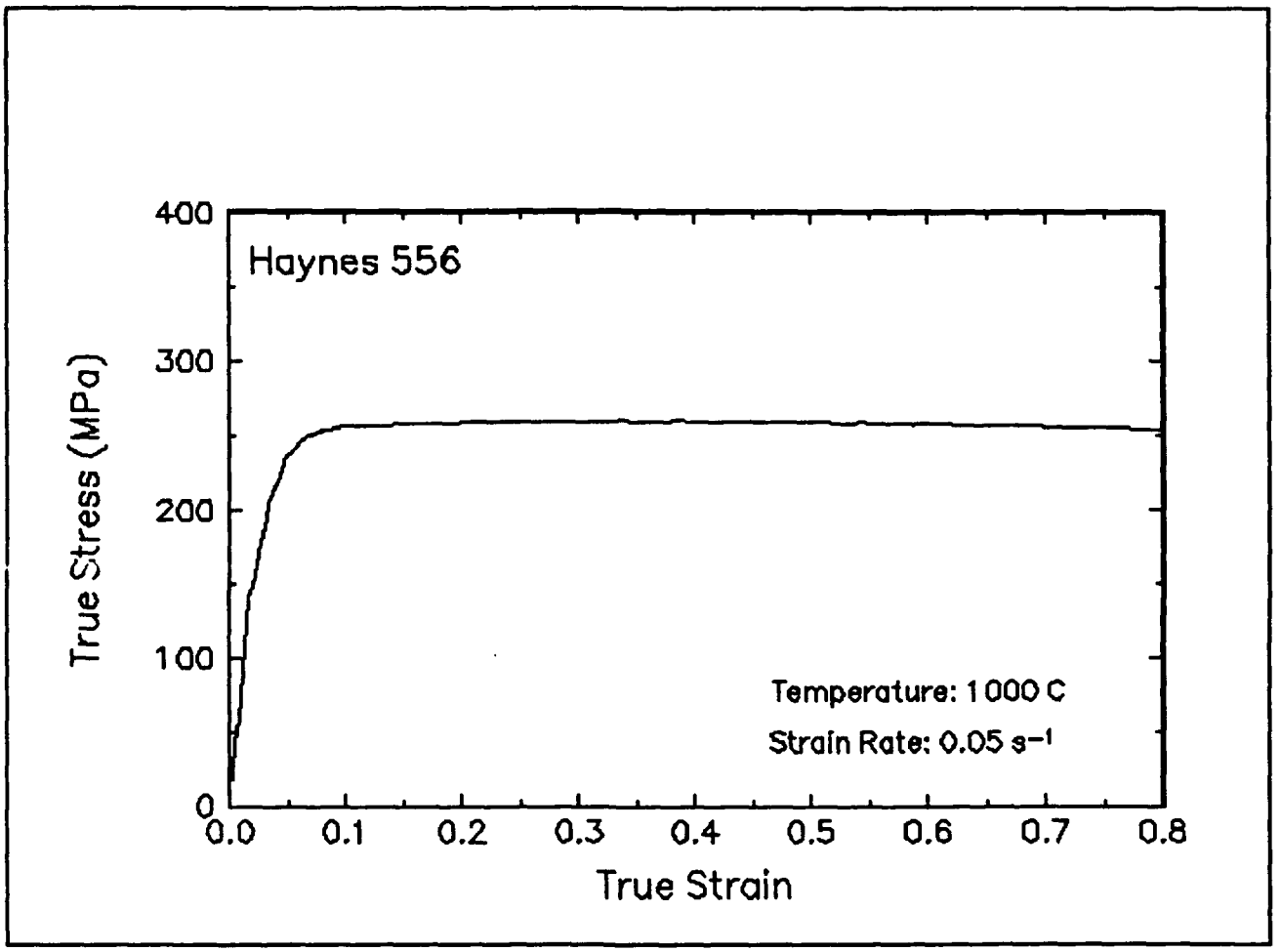

Figure 12. True stress-true strain curve, 1000 C and 0.05 s^{-1}.

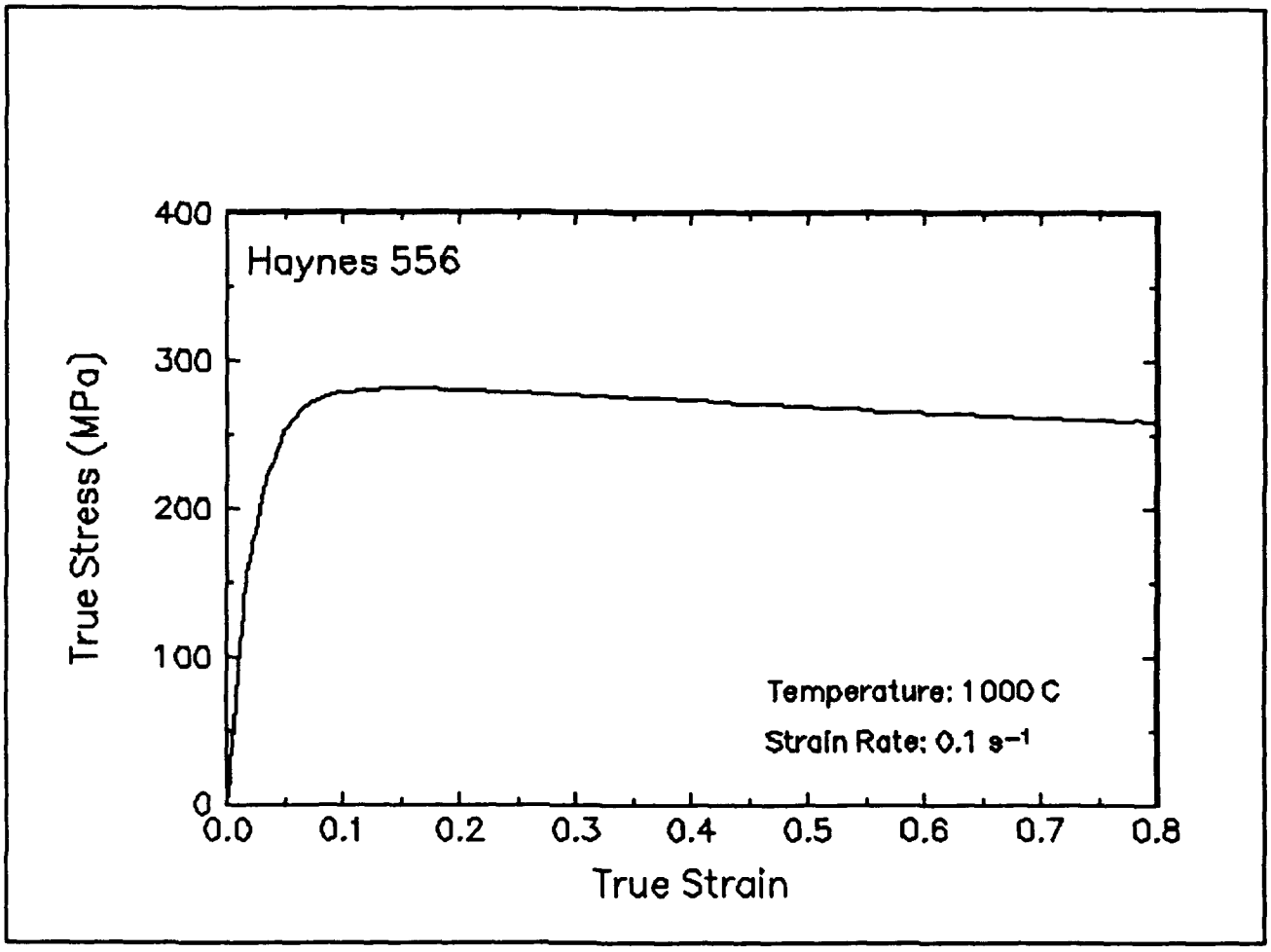

Figure 13. True stress-true strain curve, 1000 C and 0.1 s^{-1}.

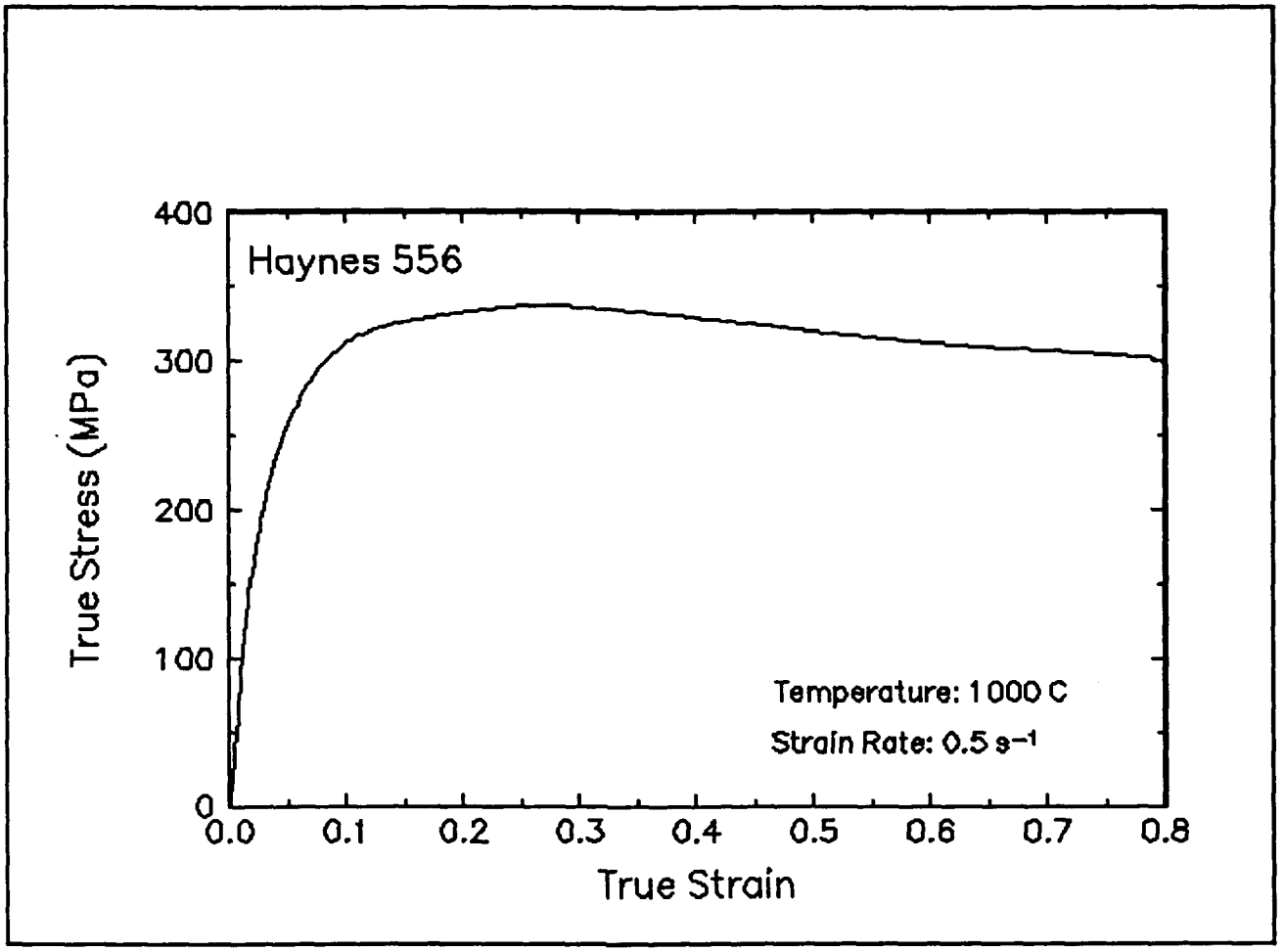

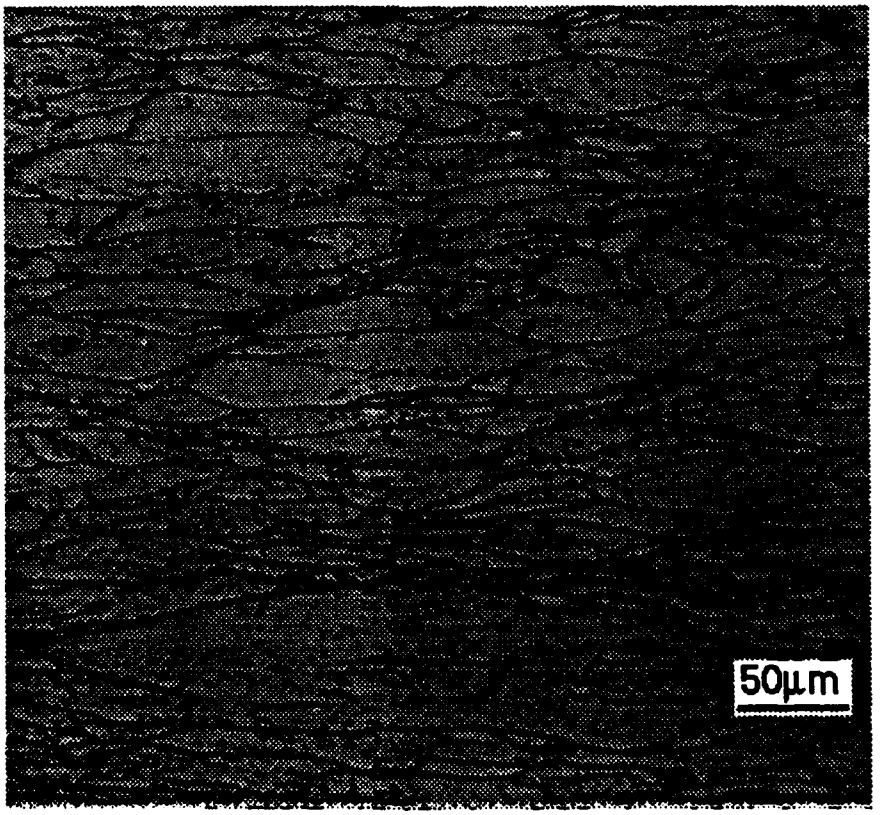

Figure 14. True stress-true strain curve and an optical micrograph from the center of the compressed sample cut through the compression axis, 1000 C and 0.5 s^{-1}.

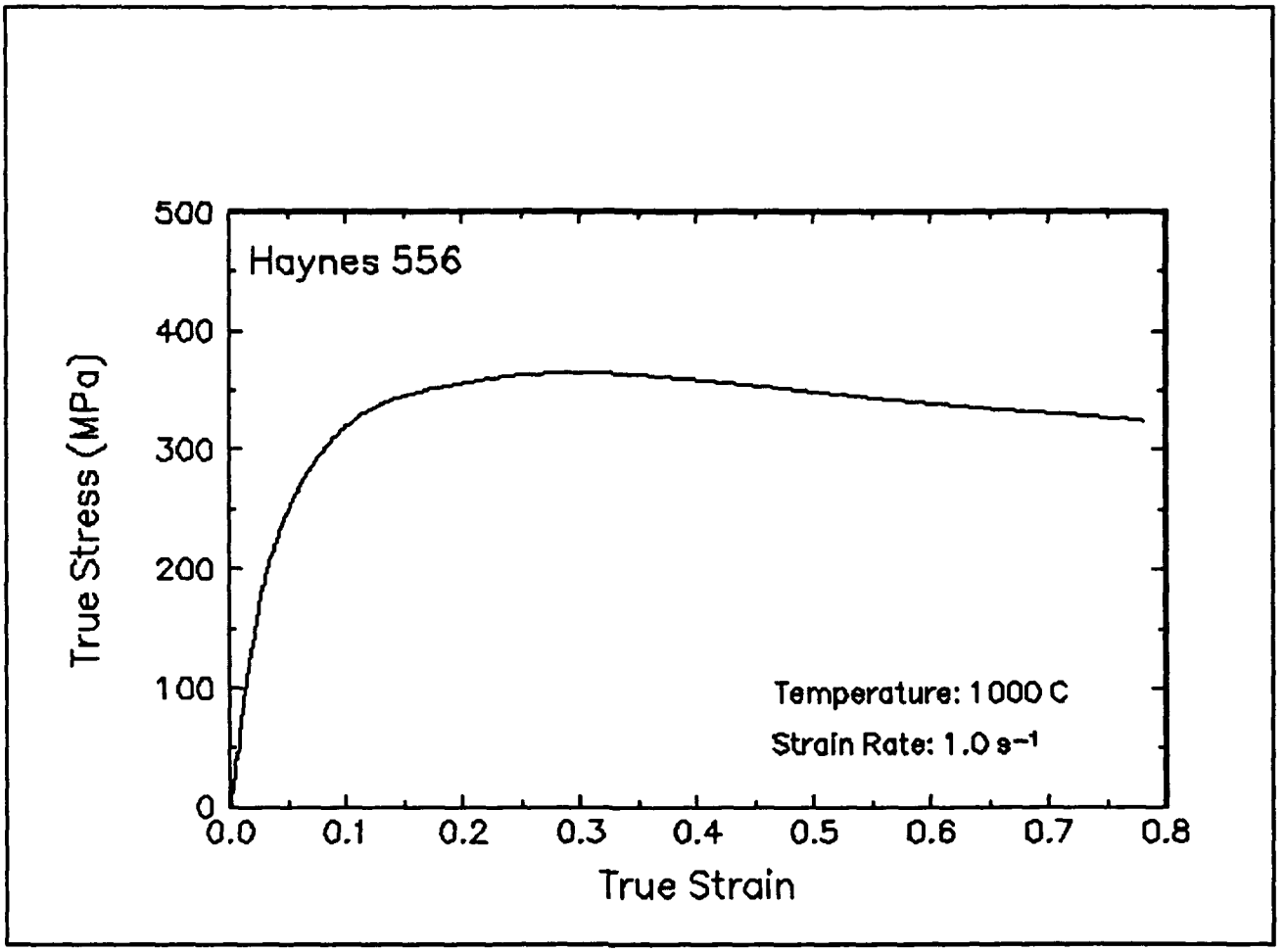

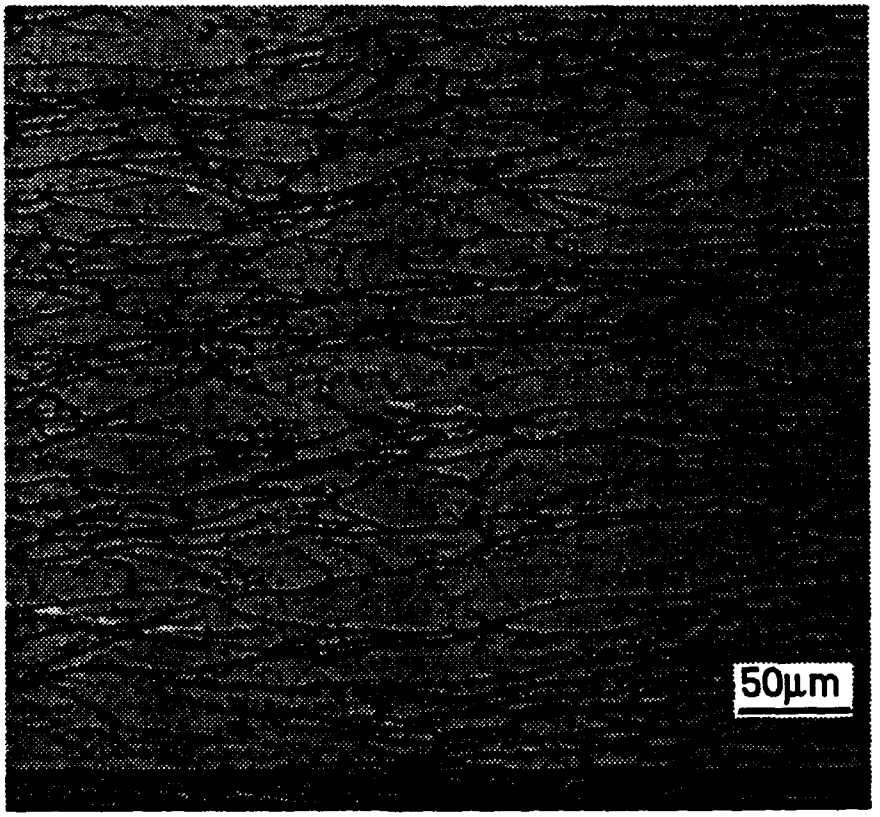

Figure 15. True stress-true strain curve and an optical micrograph from the center of the compressed sample cut through the compression axis, 1000 C and 1 s^{-1}.

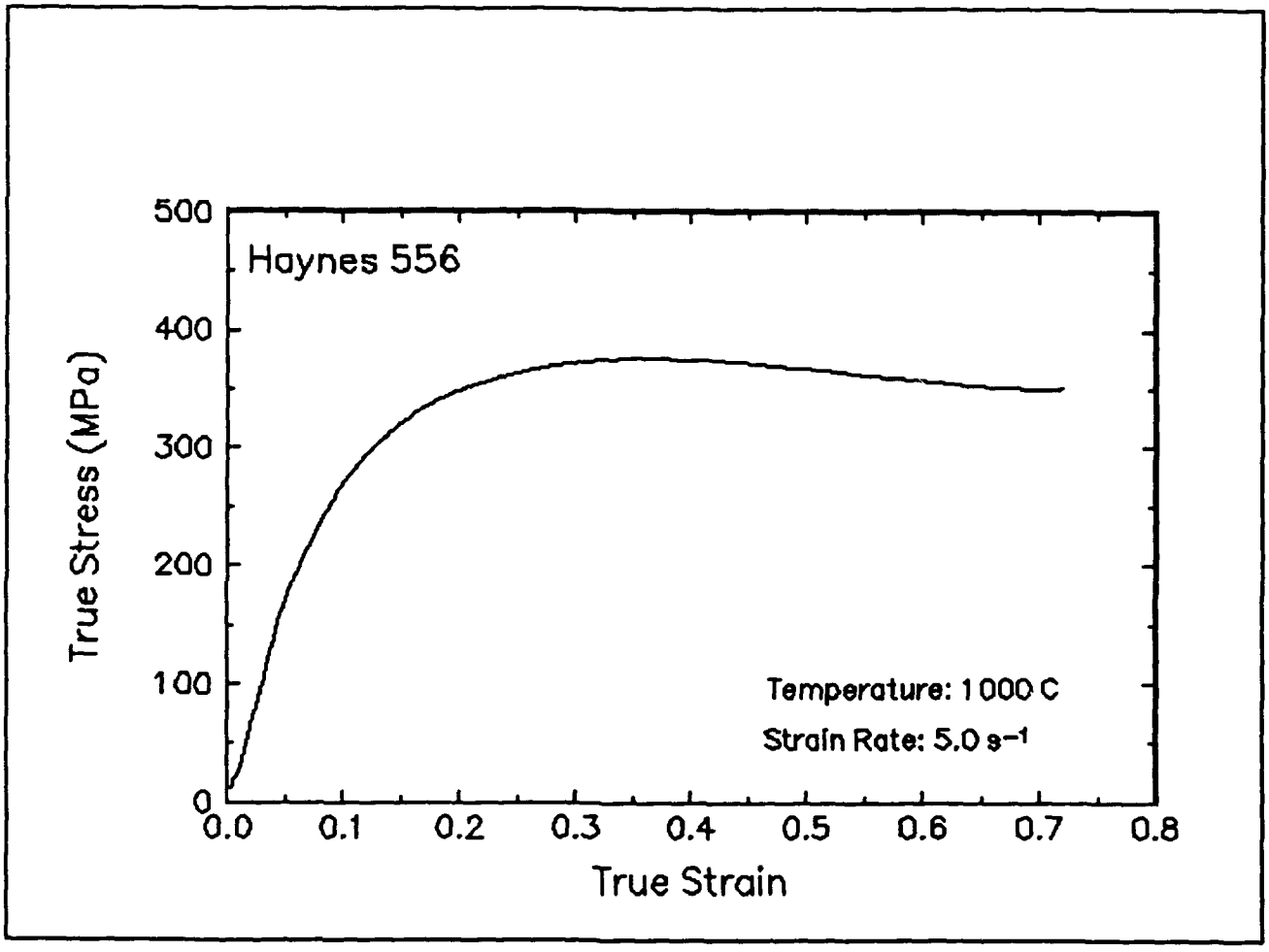

Figure 16. True stress-true strain curve, 1000 C and 5 s^{-1}.

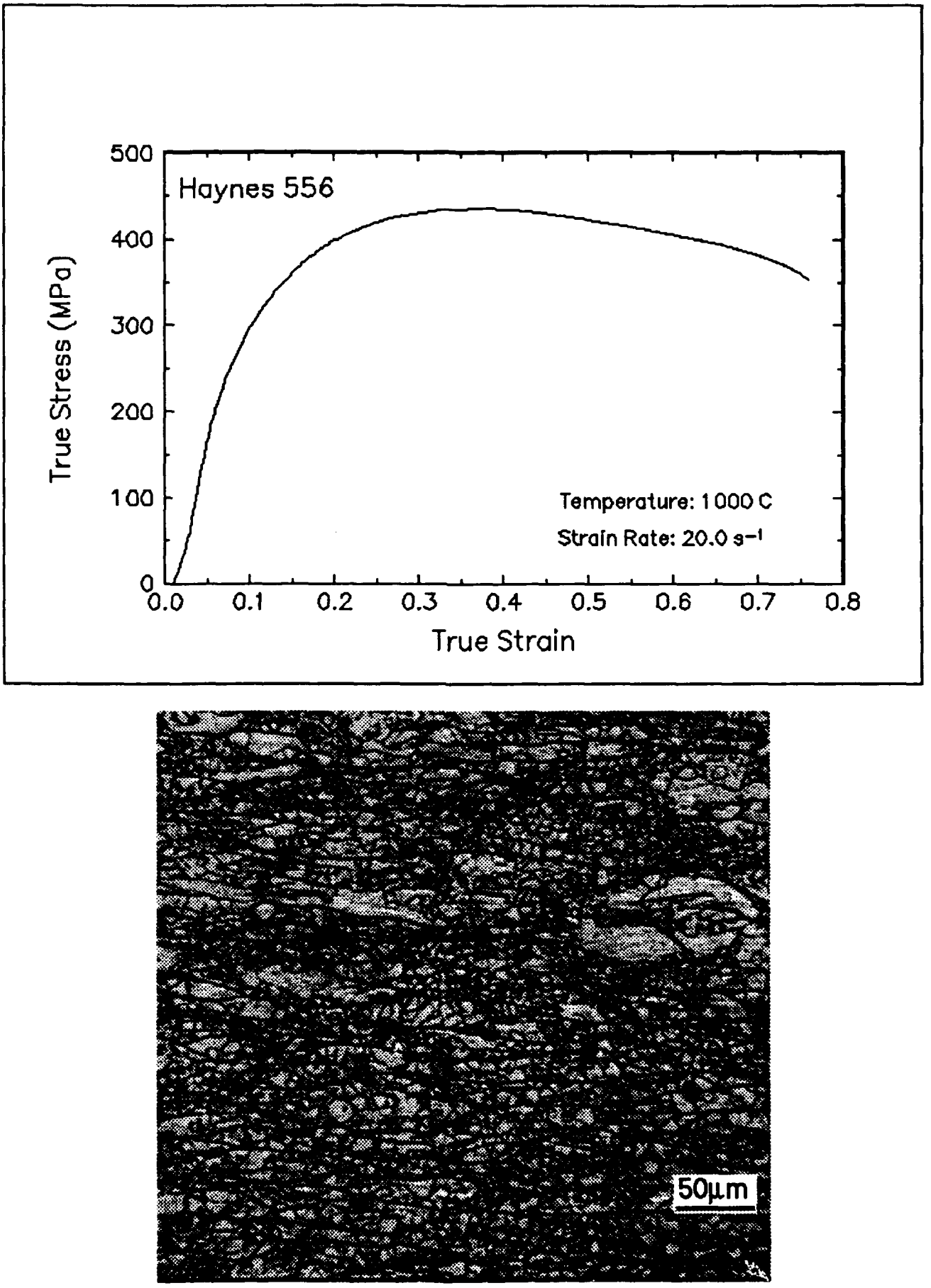

Figure 17. True stress-true strain curve and an optical micrograph from the center of the compressed sample cut through the compression axis, 1000 C and 20 s^{-1}.

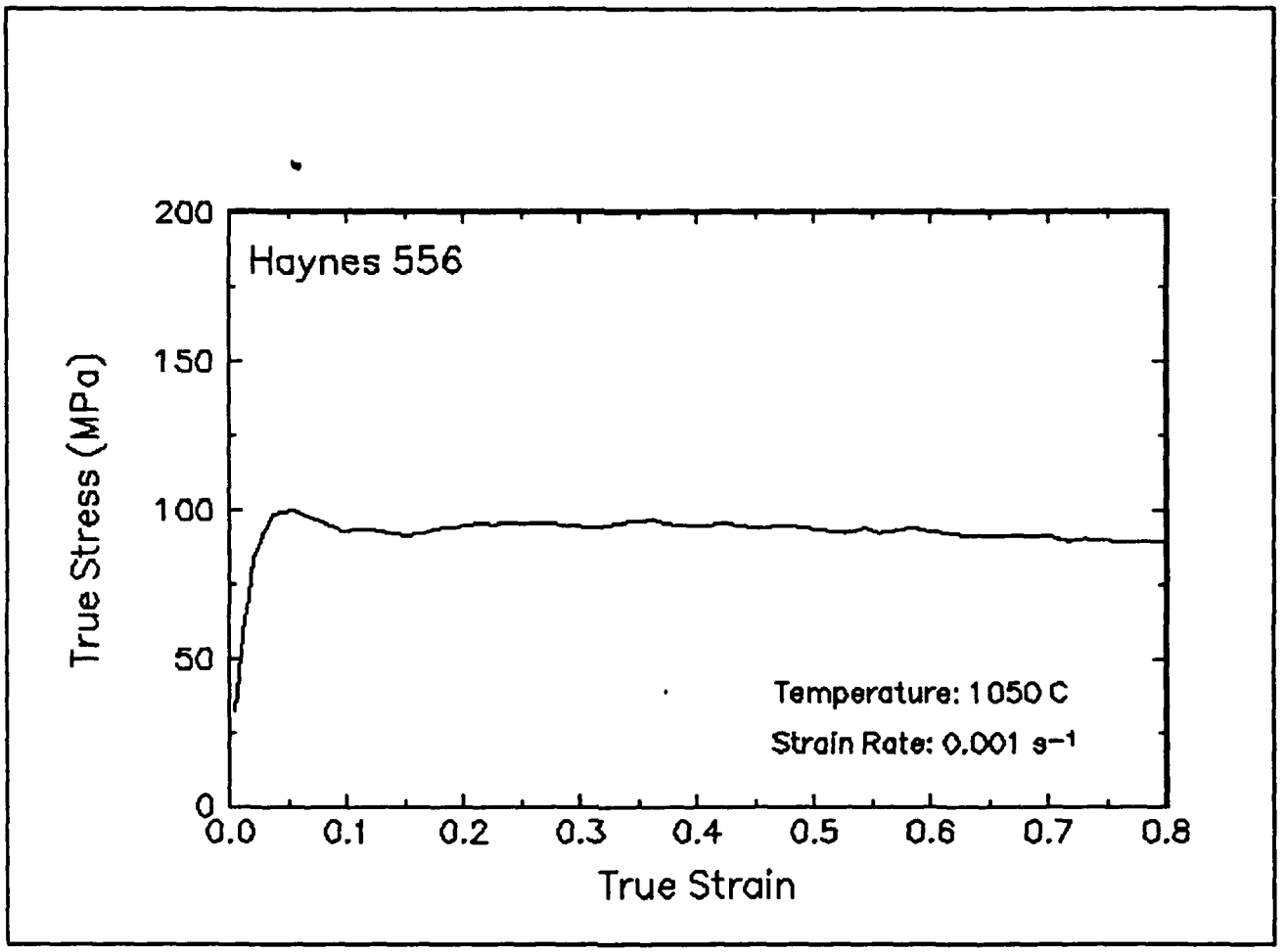

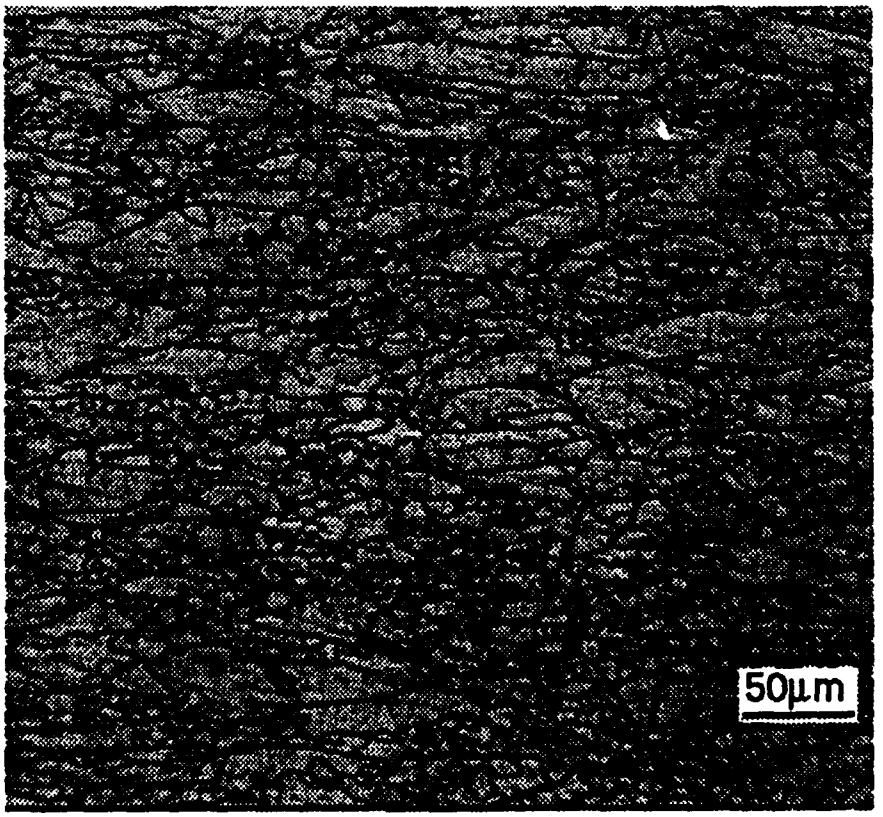

Figure 18. True stress-true strain curve and an optical micrograph from the center of the compressed sample cut through the compression axis, 1050 C and 0.001 s^{-1}.

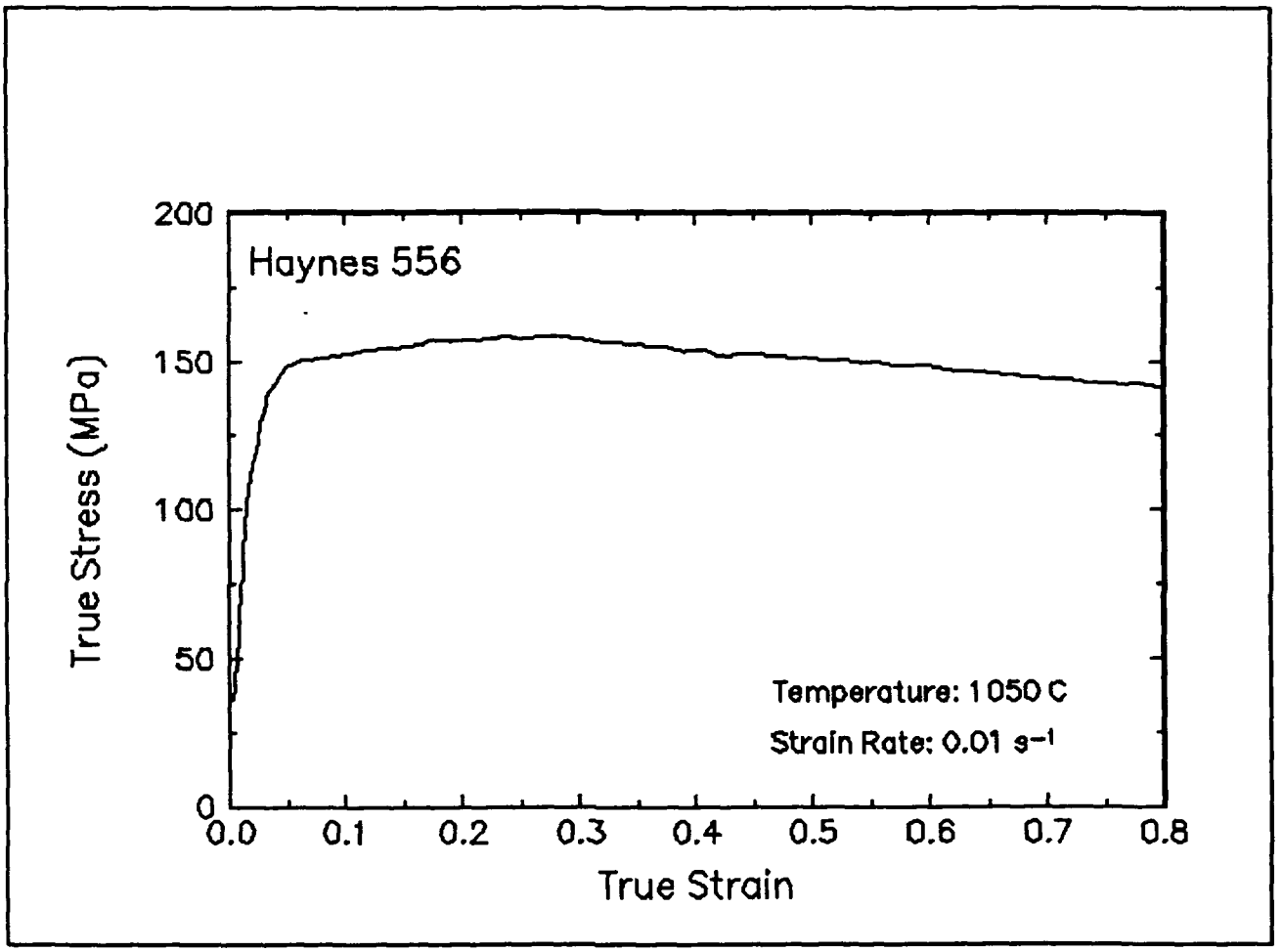

Figure 19. True stress-true strain curve, 1050 C and 0.01 s^{-1}.

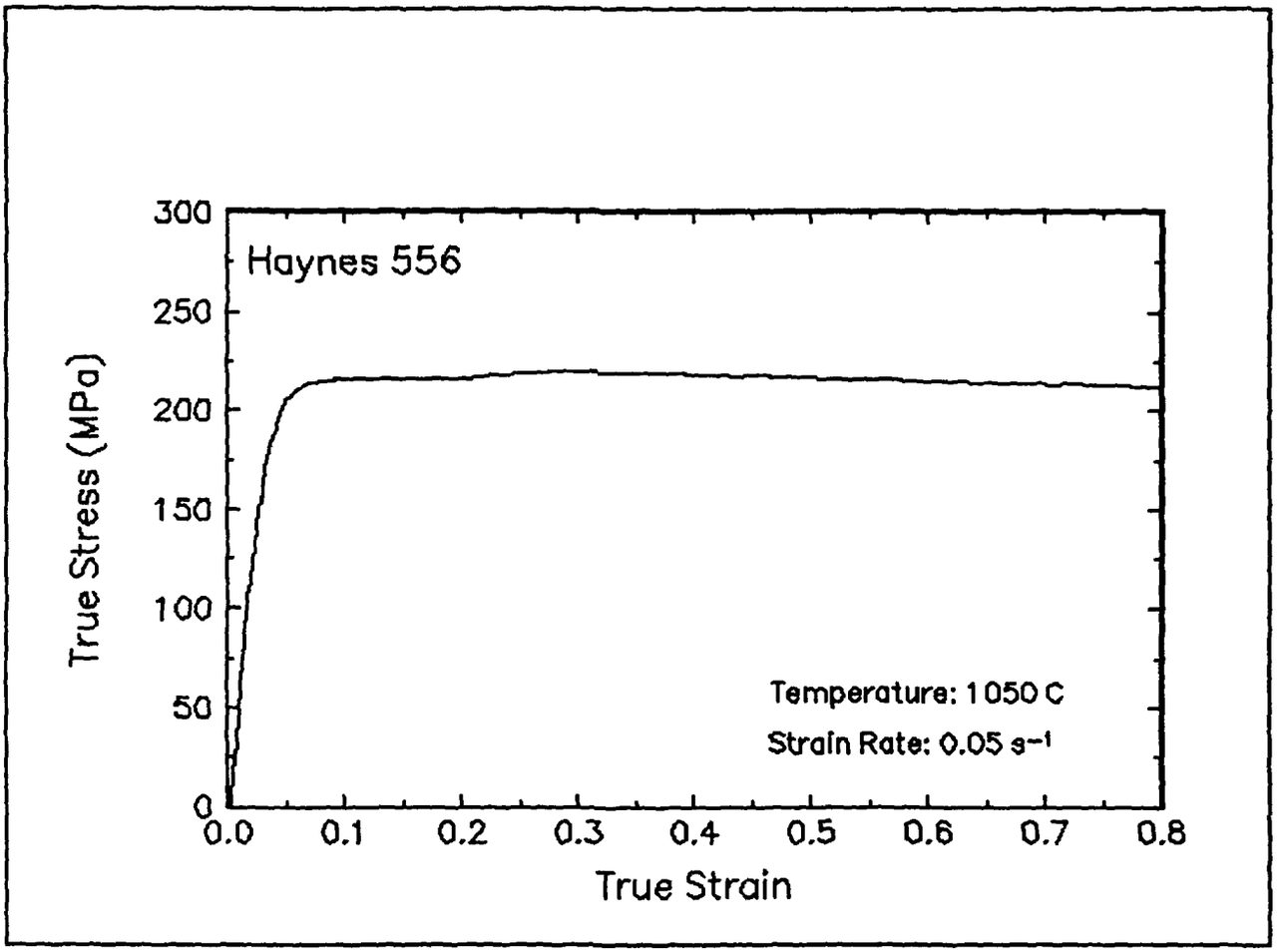

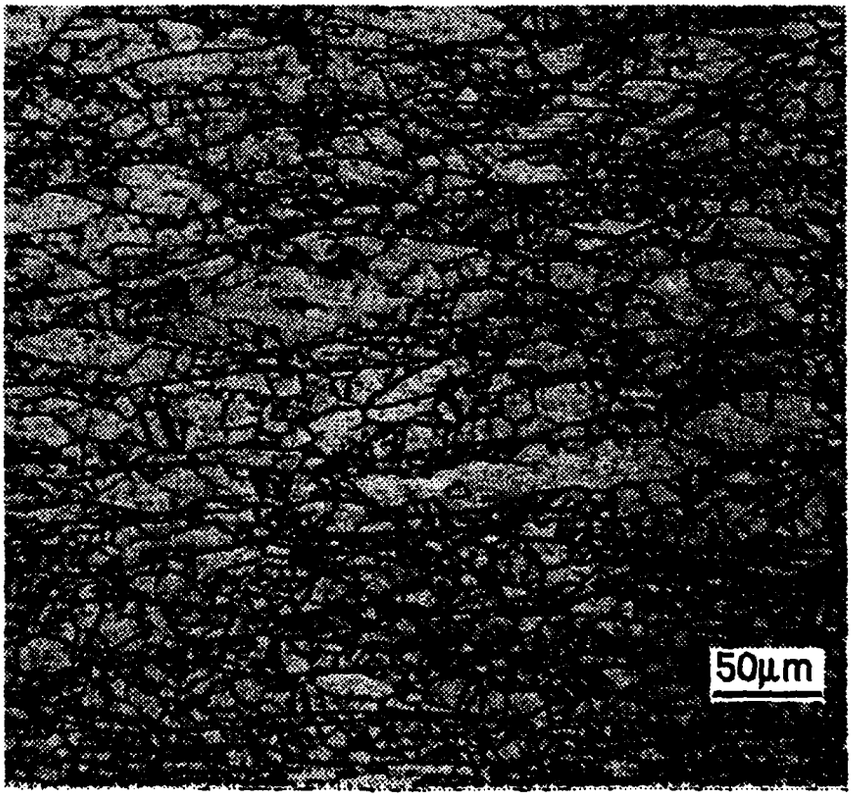

Figure 20. True stress-true strain curve and an optical micrograph from the center of the compressed sample cut through the compression axis, 1050 C and 0.05 s^{-1}.

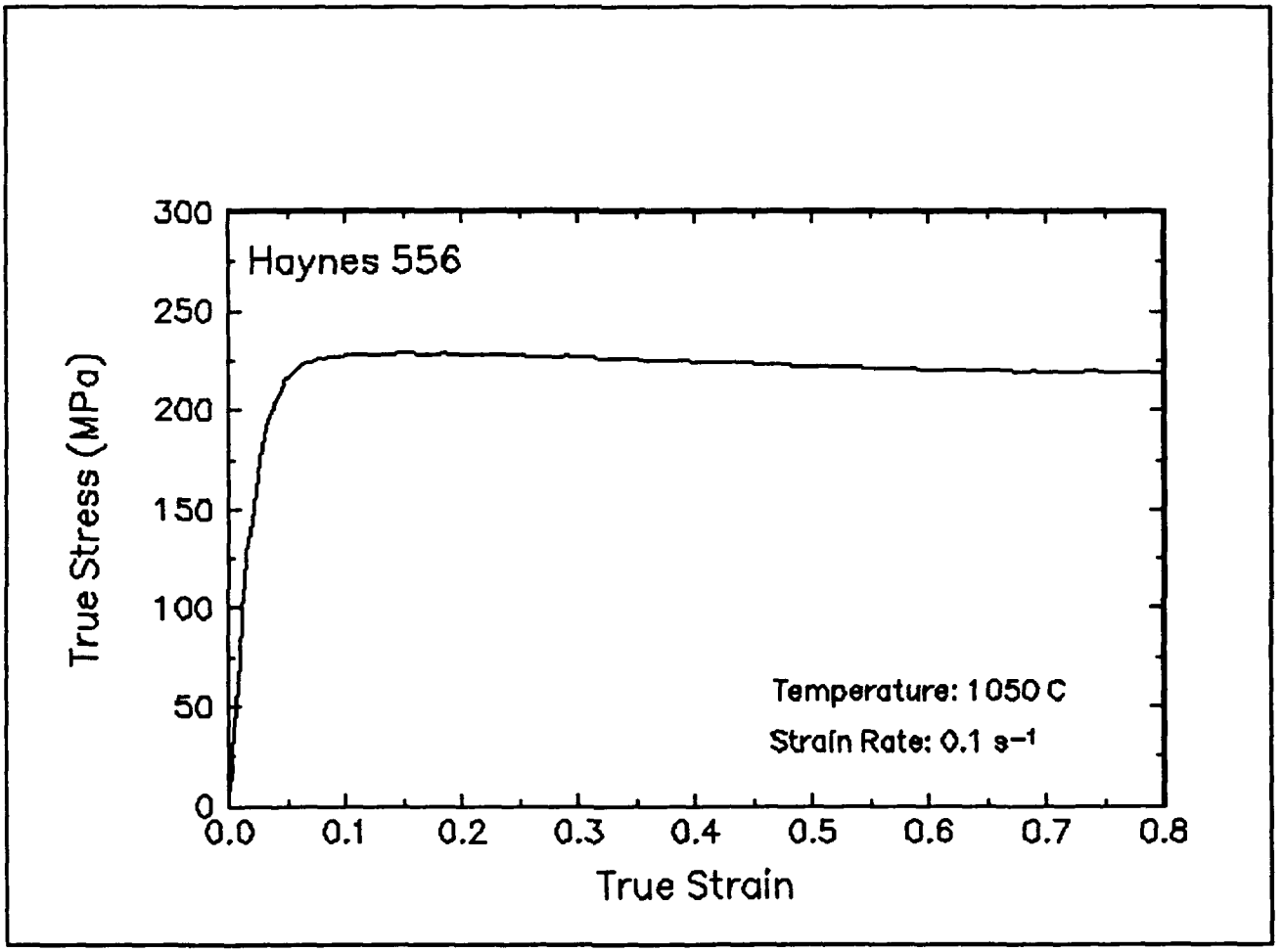

Figure 21. True stress-true strain curve, 1050 C and 0.1 s^{-1}.

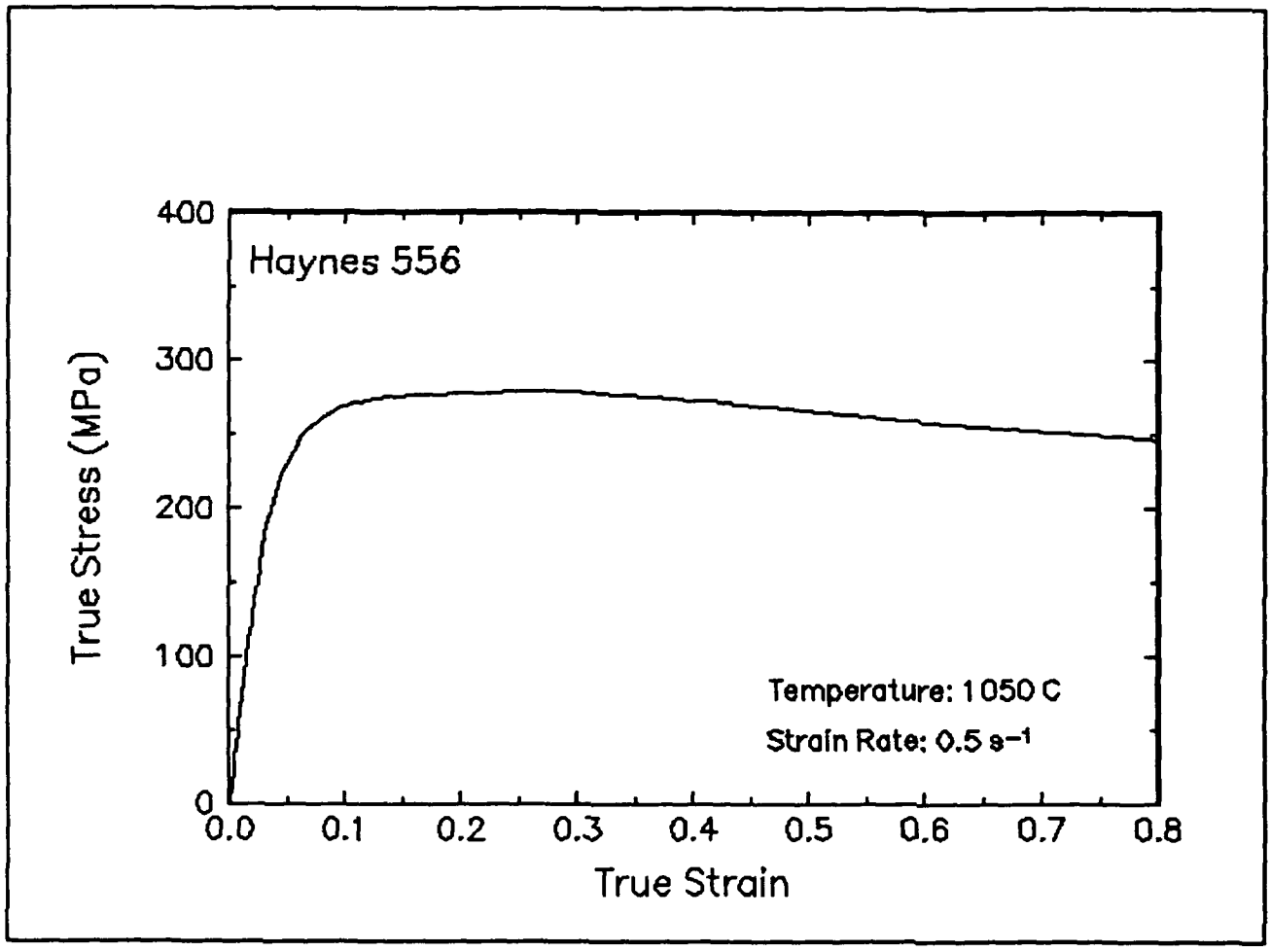

Figure 22. True stress-true strain curve, 1050 C and 0.5 s^{-1}.

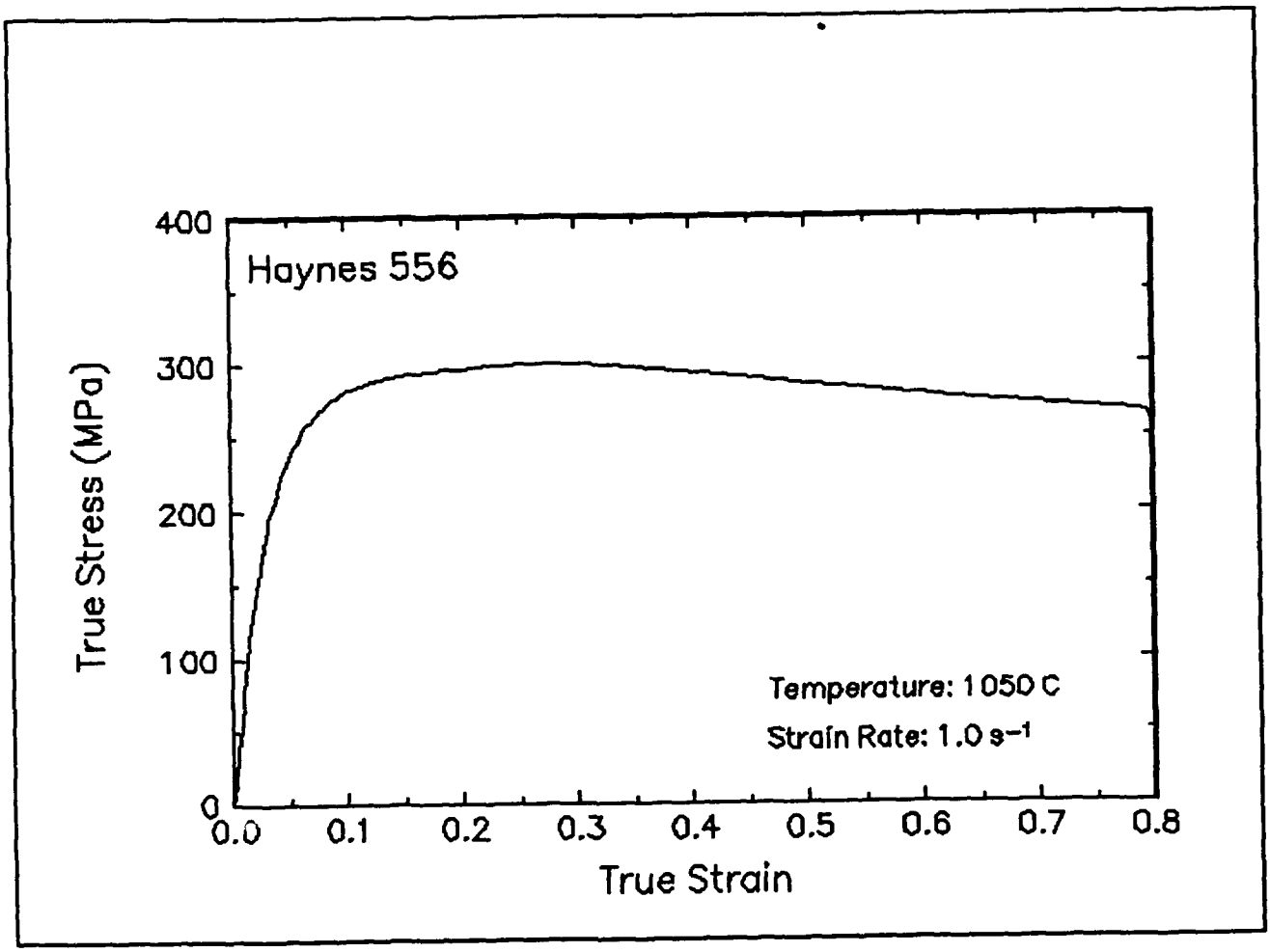

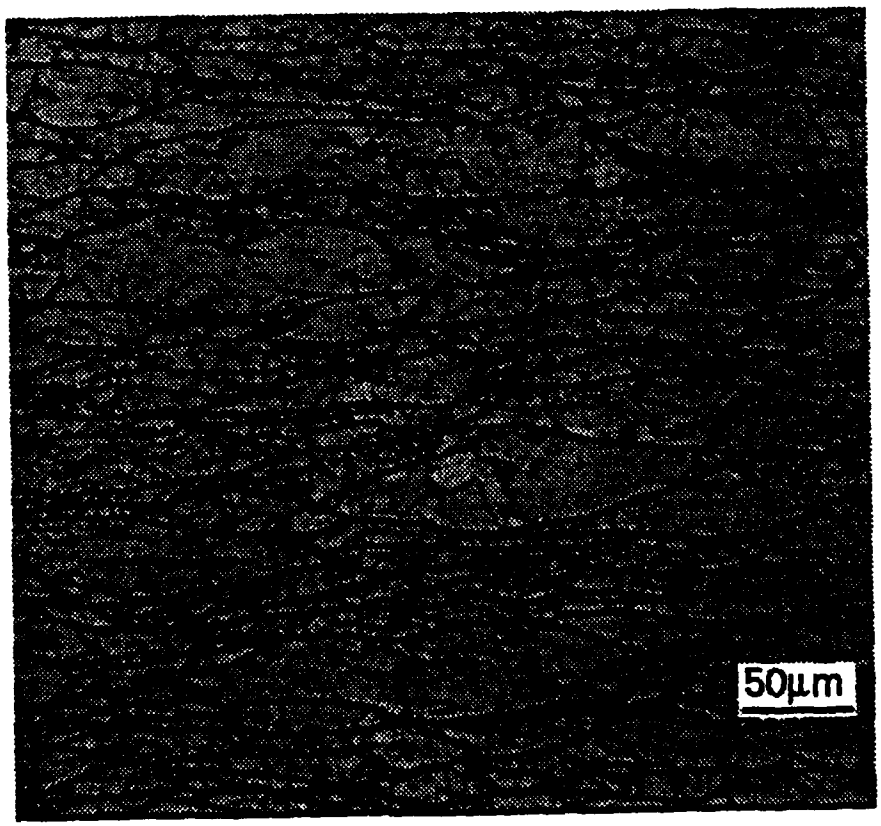

Figure 23. True stress-true strain curve and an optical micrograph from the center of the compressed sample cut through the compression axis, 1050 C and 1 s^{-1}.

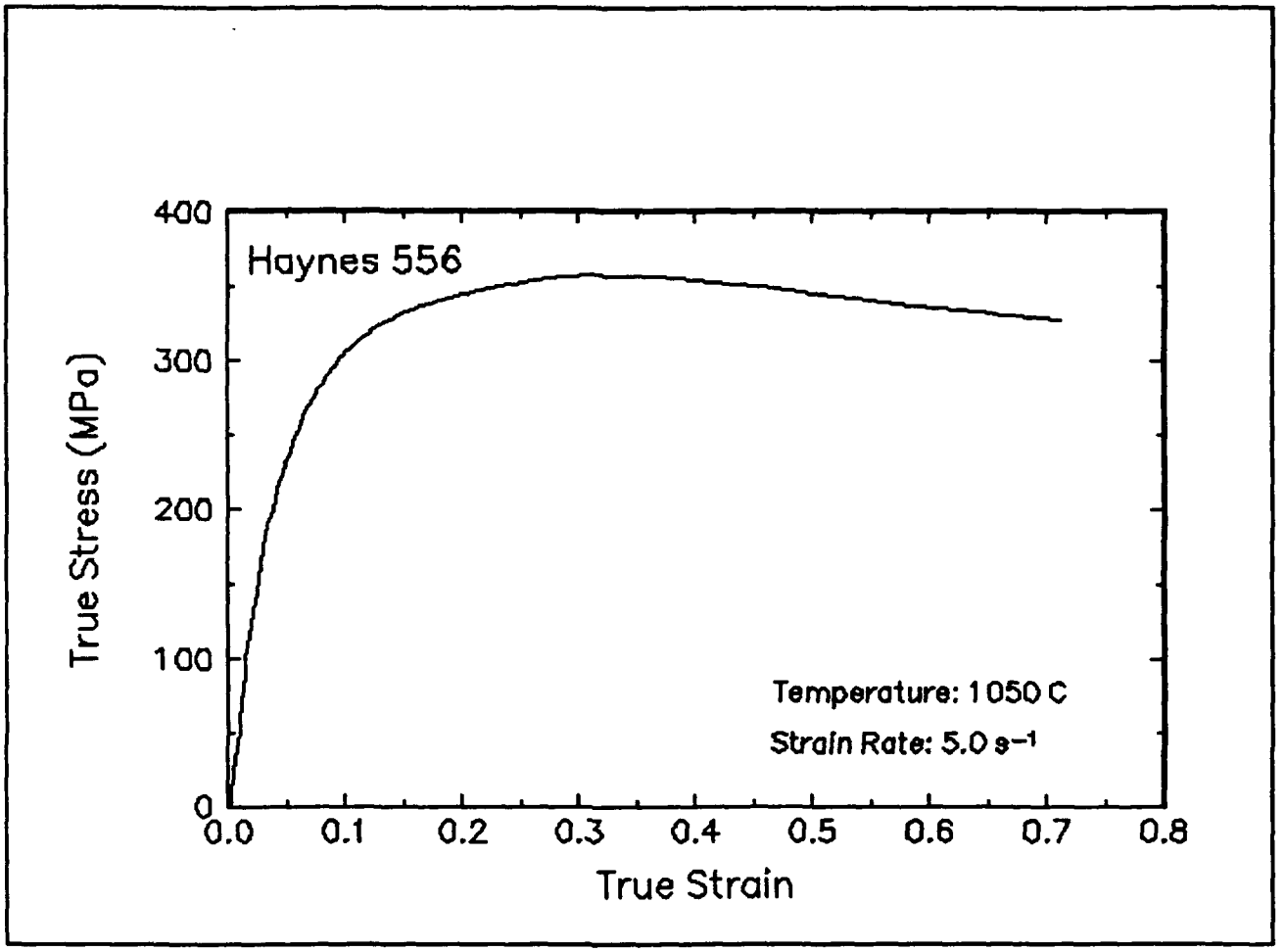

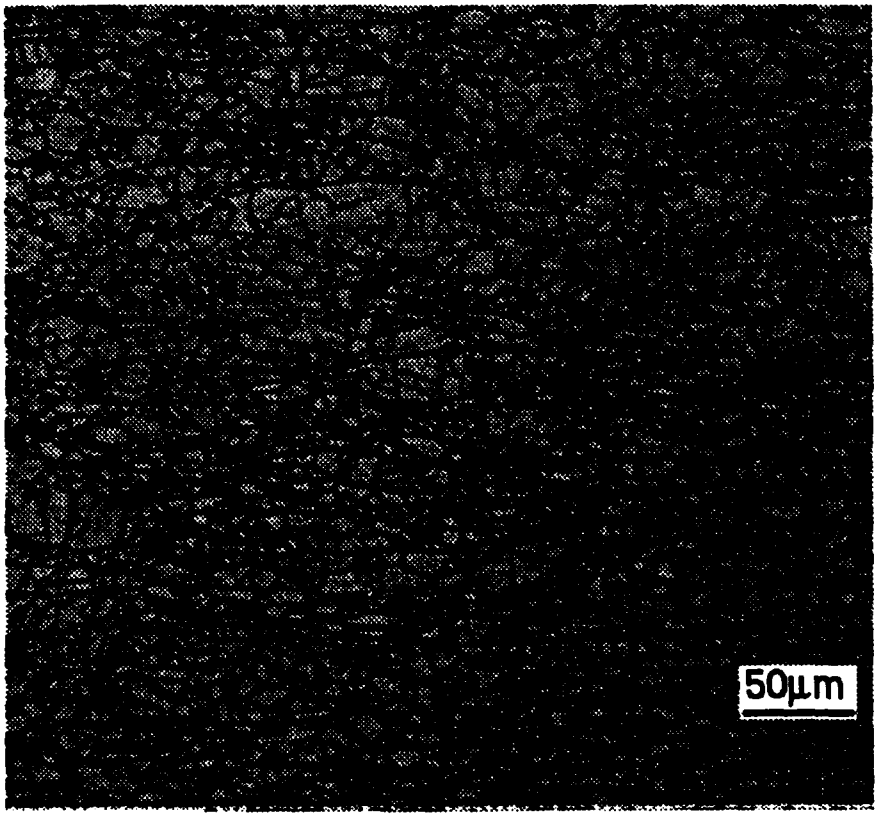

Figure 24. True stress-true strain curve and an optical micrograph from the center of the compressed sample cut through the compression axis, 1050 C and 5 s^{-1}.

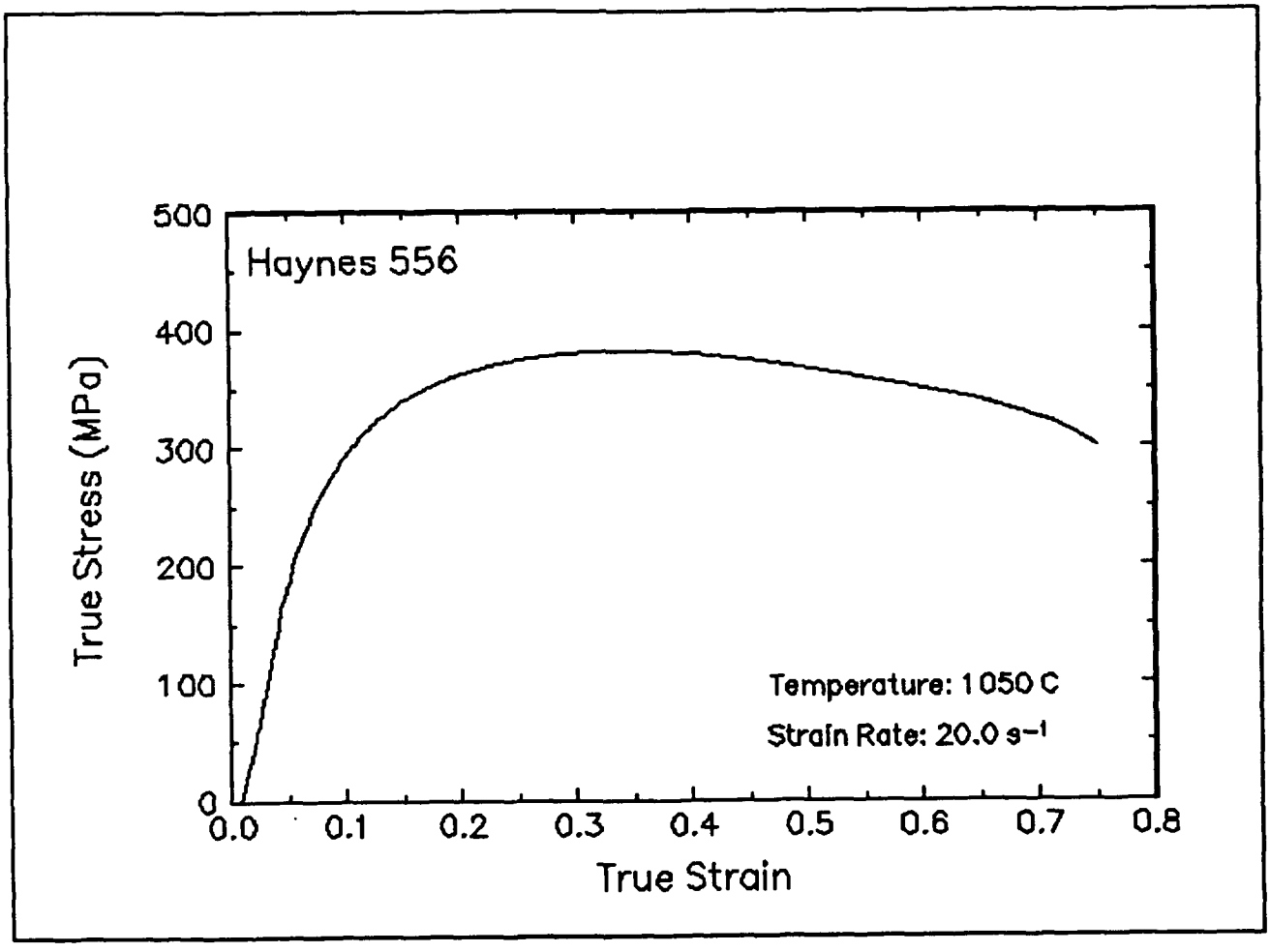

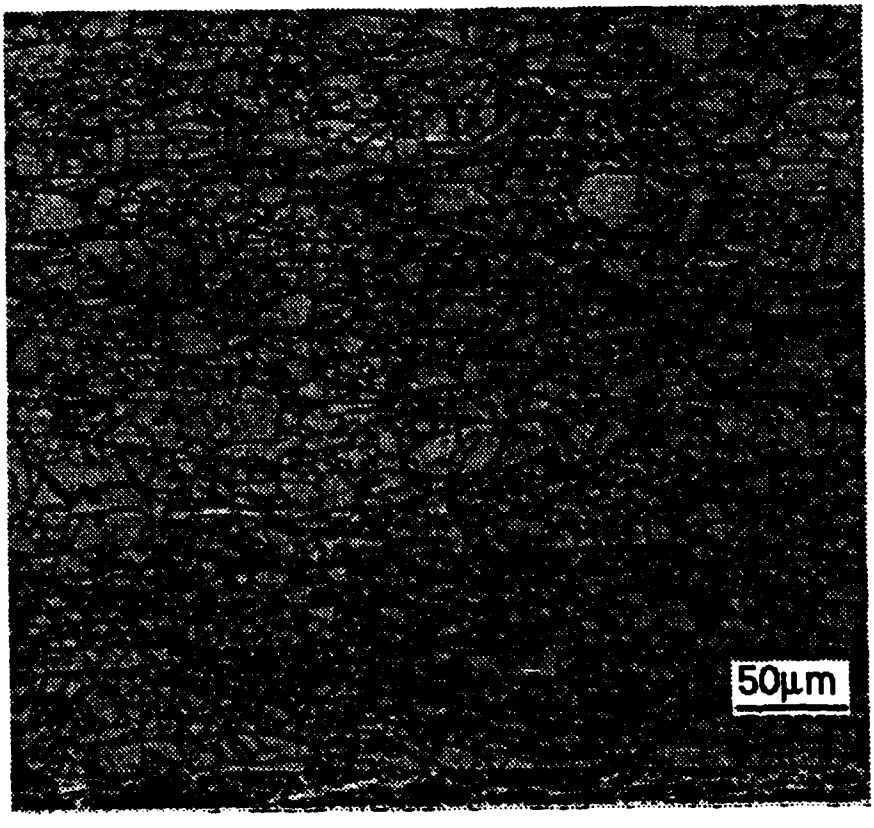

Figure 25. True stress-true strain curve and an optical micrograph from the center of the compressed sample cut through the compression axis, 1050 C and 20 s^{-1}.

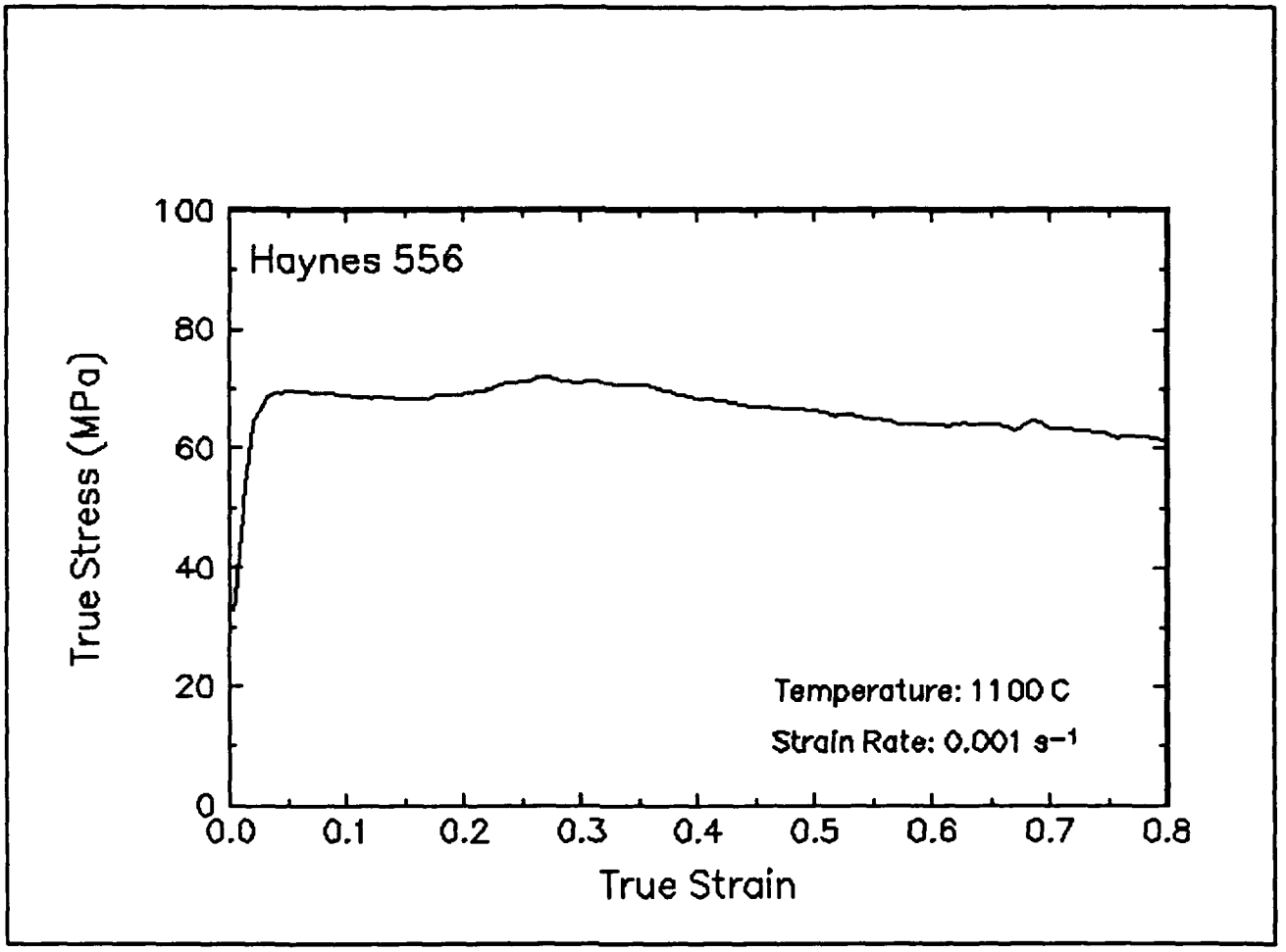

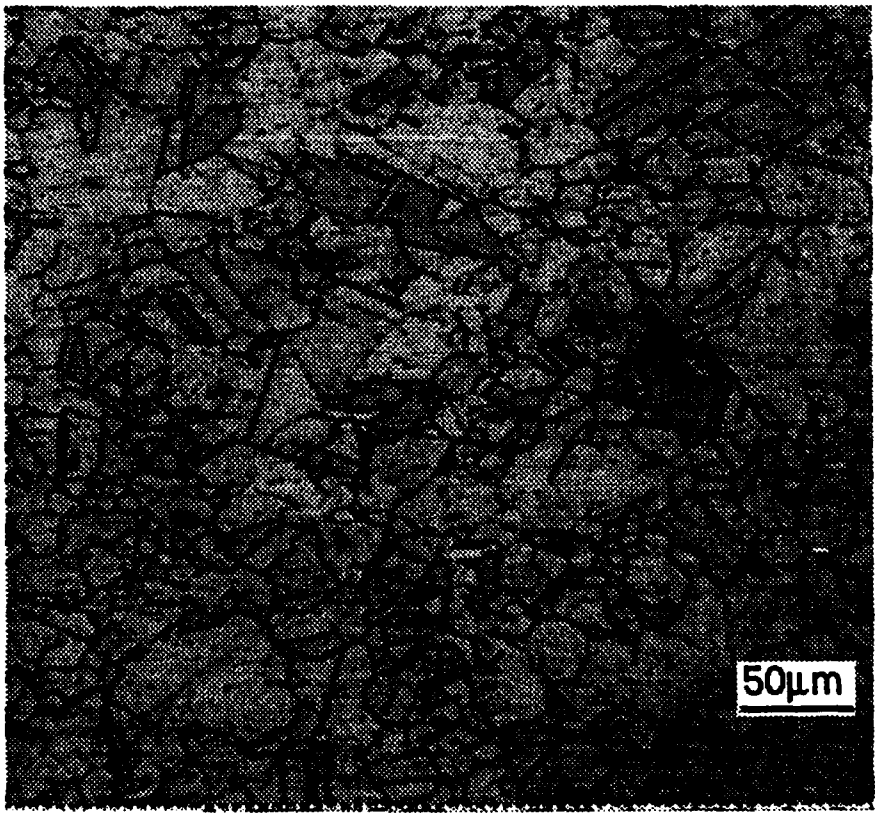

Figure 26. True stress-true strain curve and an optical micrograph from the center of the compressed sample cut through the compression axis, 1100 C and 0.001 s^{-1}.

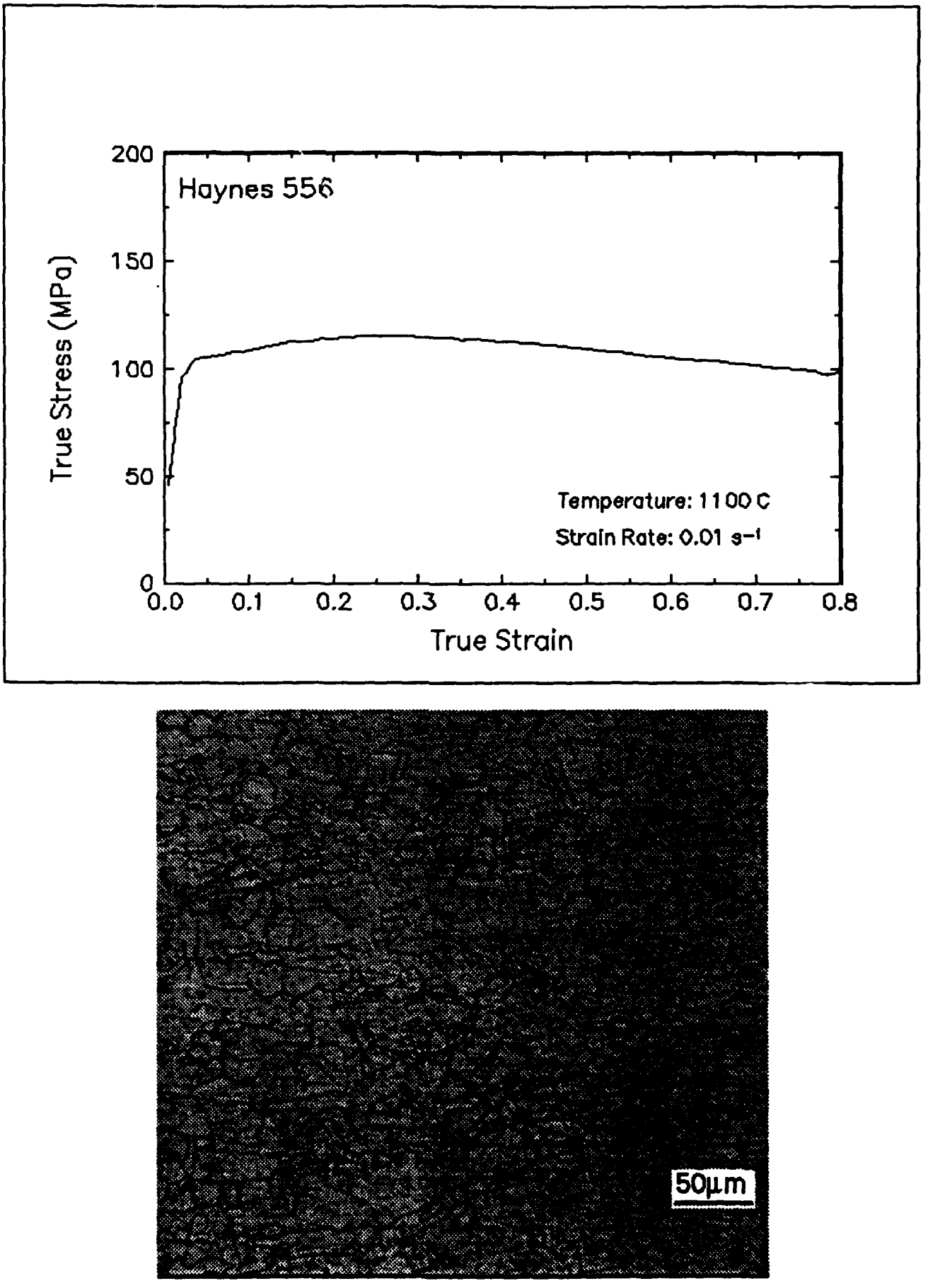

Figure 27. True stress-true strain curve and an optical micrograph from the center of the compressed sample cut through the compression axis, 1100 C and 0.01 s^{-1}.

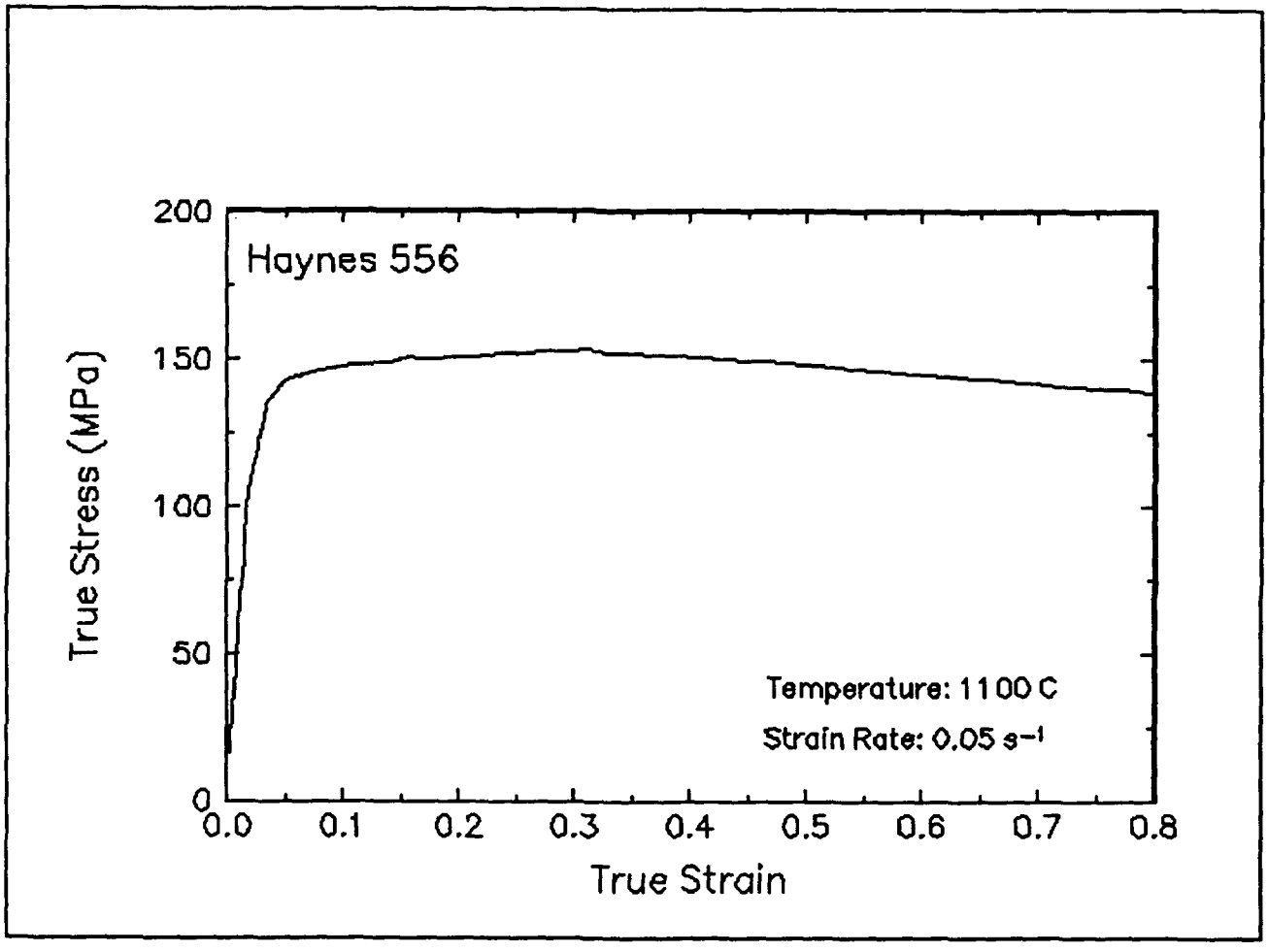

Figure 28. True stress-true strain curve, 1100 C and 0.05 s^{-1}.

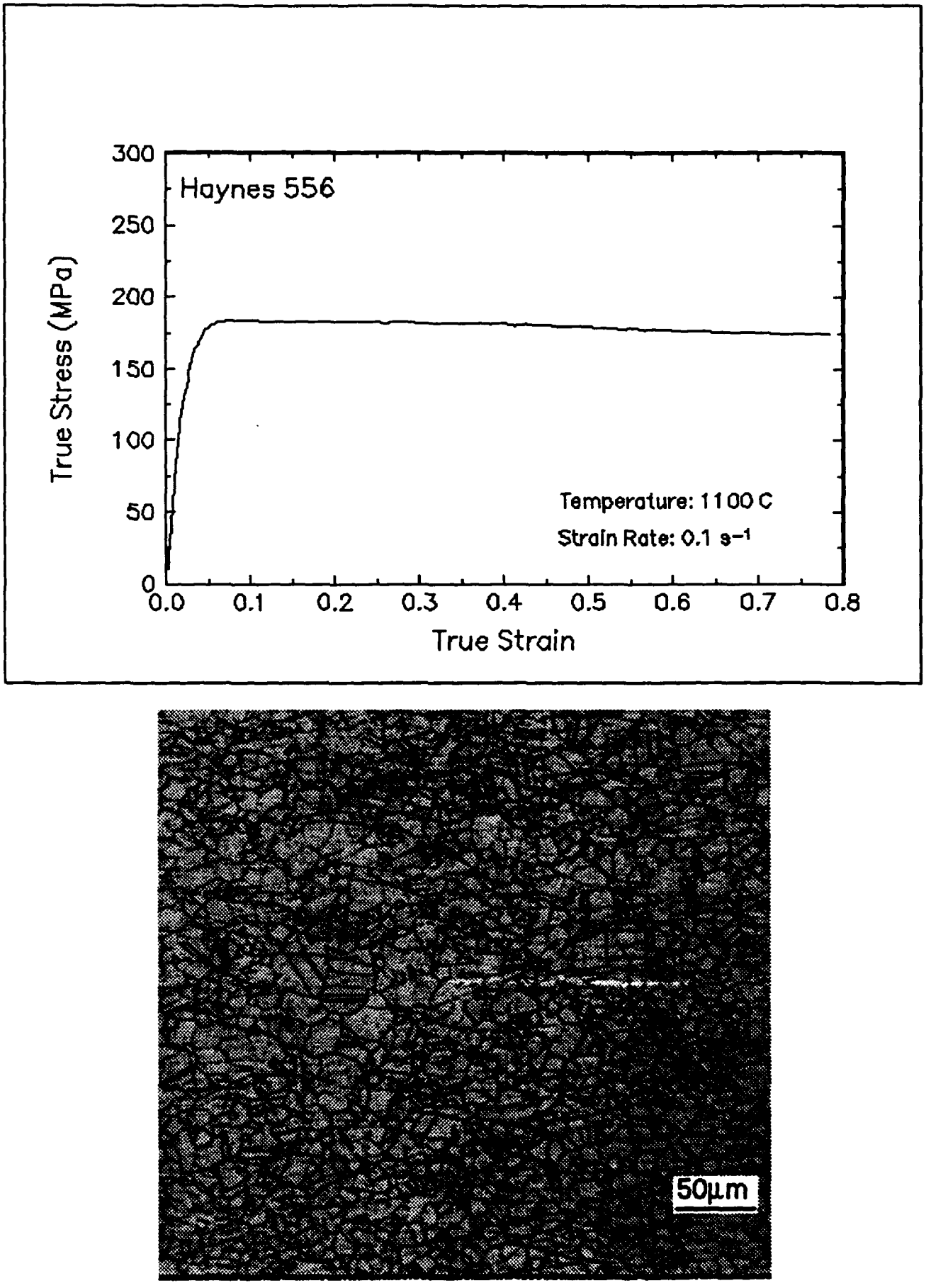

Figure 29. True stress-true strain curve and an optical micrograph from the center of the compressed sample cut through the compression axis, 1100 C and 0.1 s^{-1}.

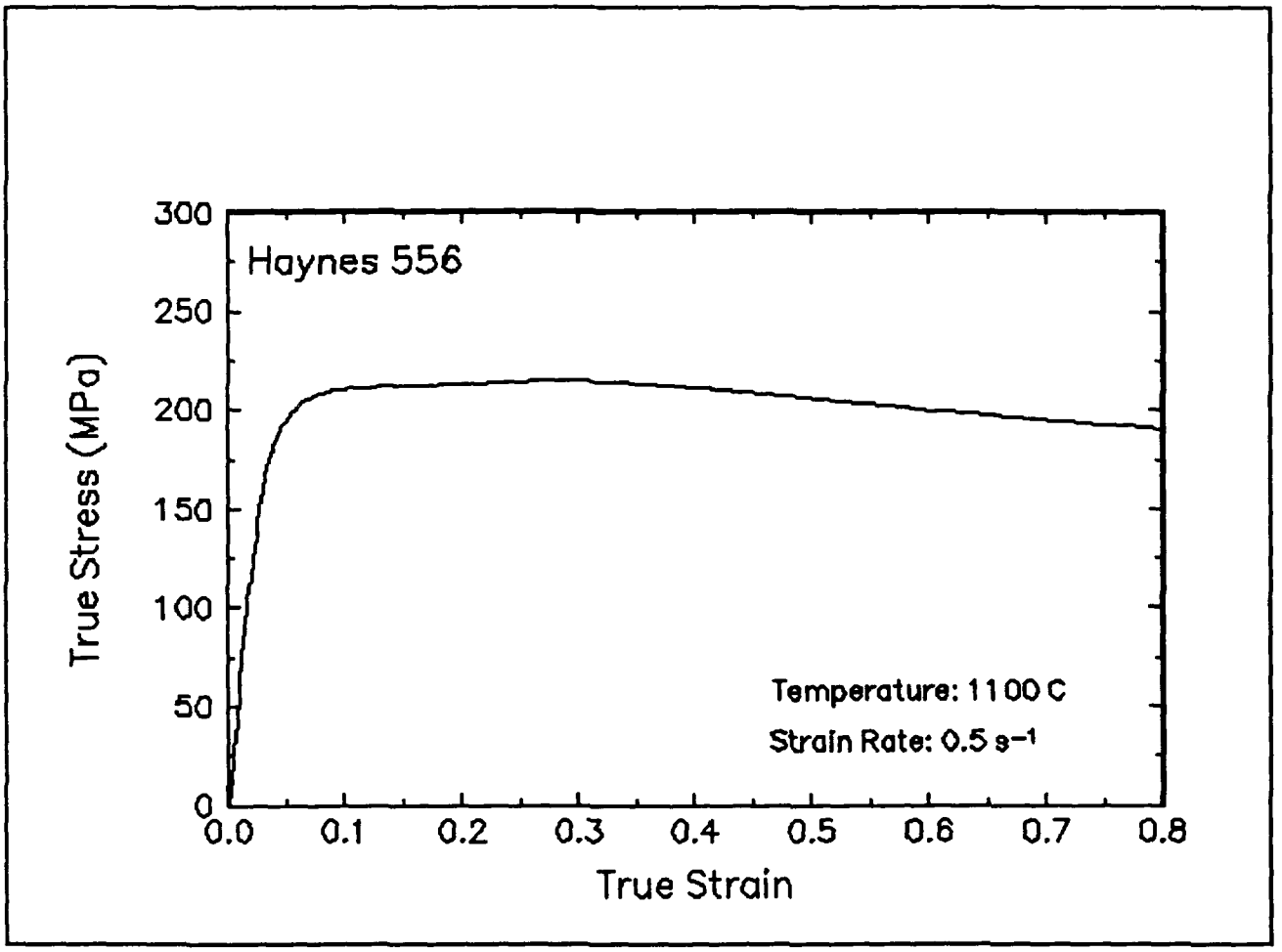

Figure 30. True stress-true strain curve, 1100 C and 0.5 s^{-1}.

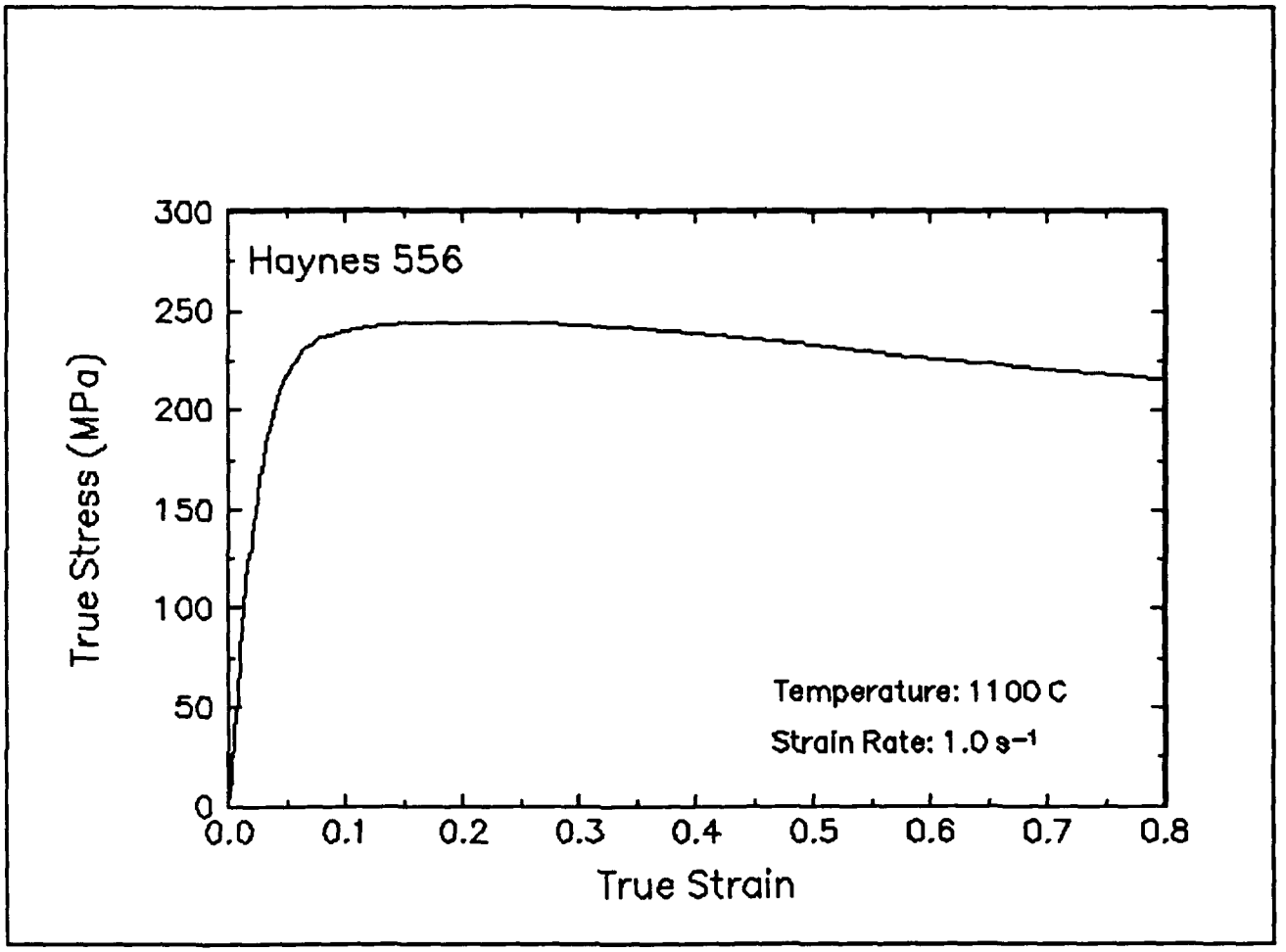

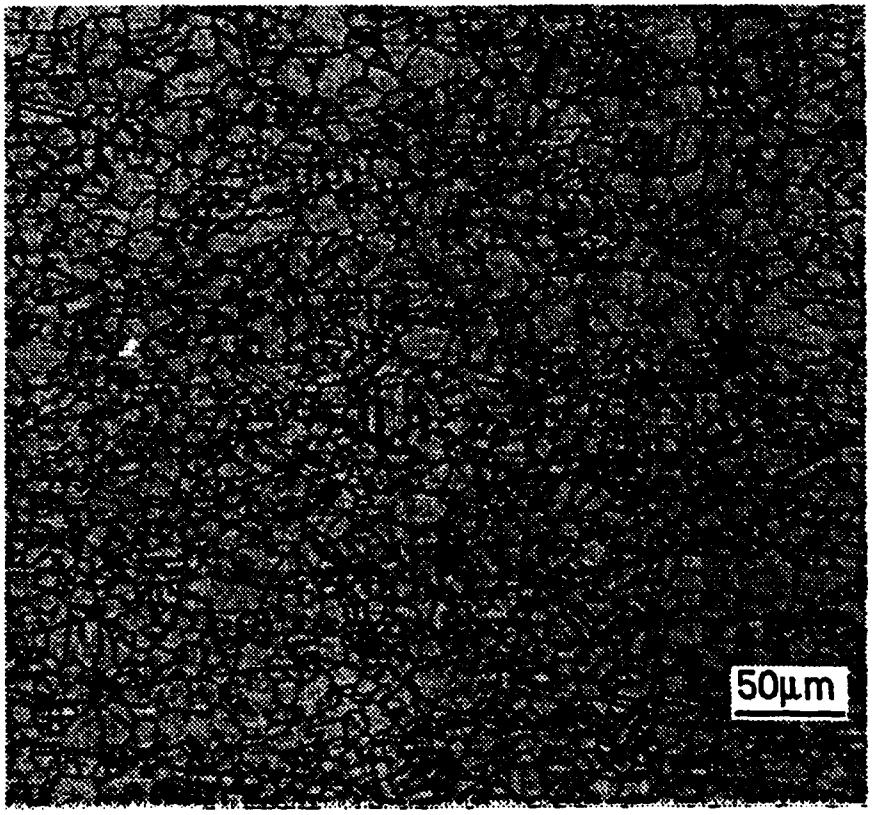

Figure 31. True stress-true strain curve and an optical micrograph from the center of the compressed sample cut through the compression axis, 1100 C and 1 s^{-1}.

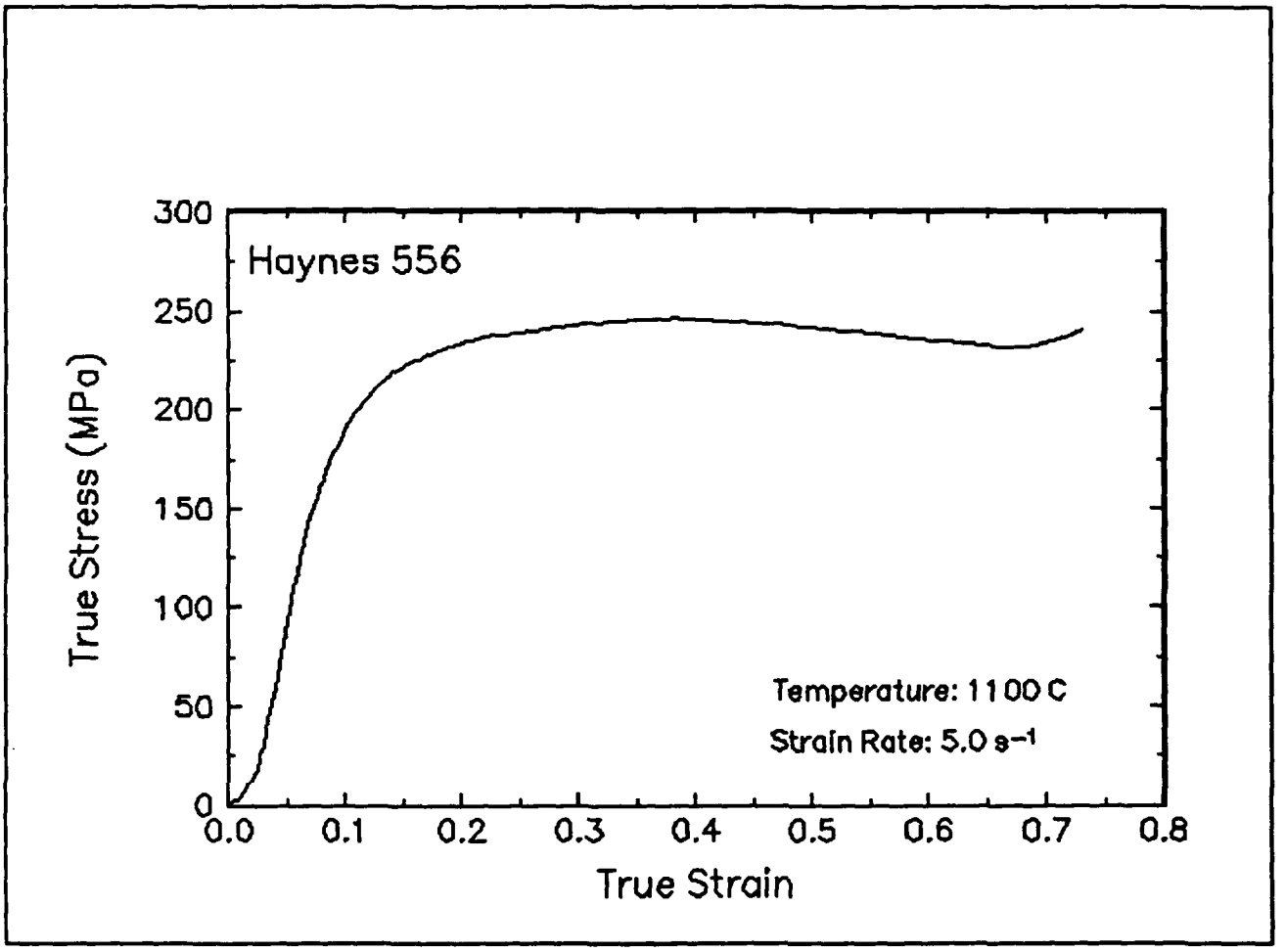

Figure 32. True stress-true strain curve, 1100 C and 5 s^{-1}.

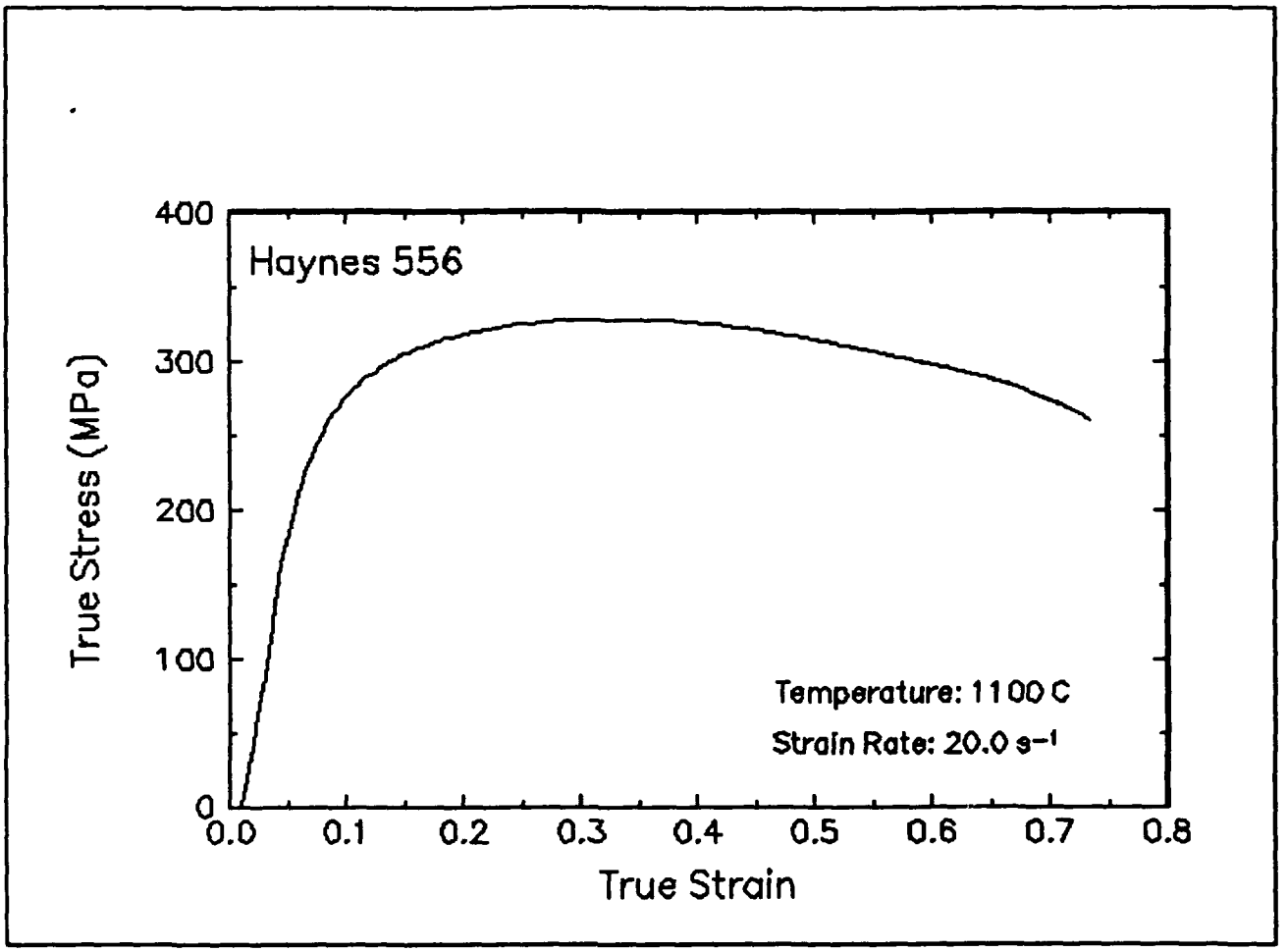

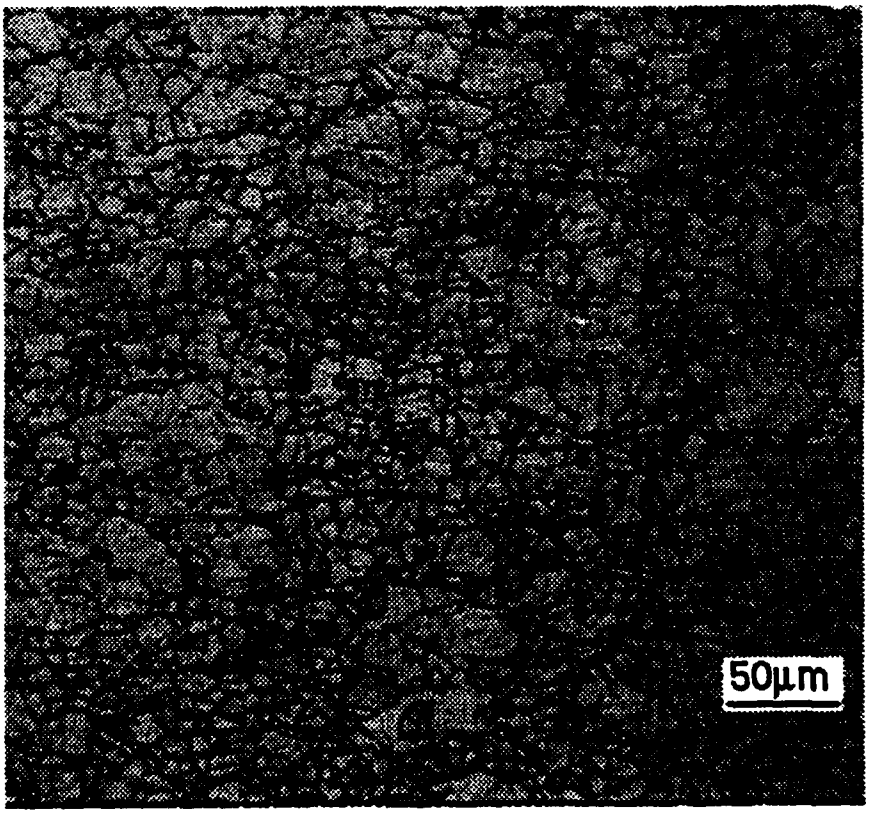

Figure 33. True stress-true strain curve and an optical micrograph from the center of the compressed sample cut through the compression axis, 1100 C and 20 s^{-1}.

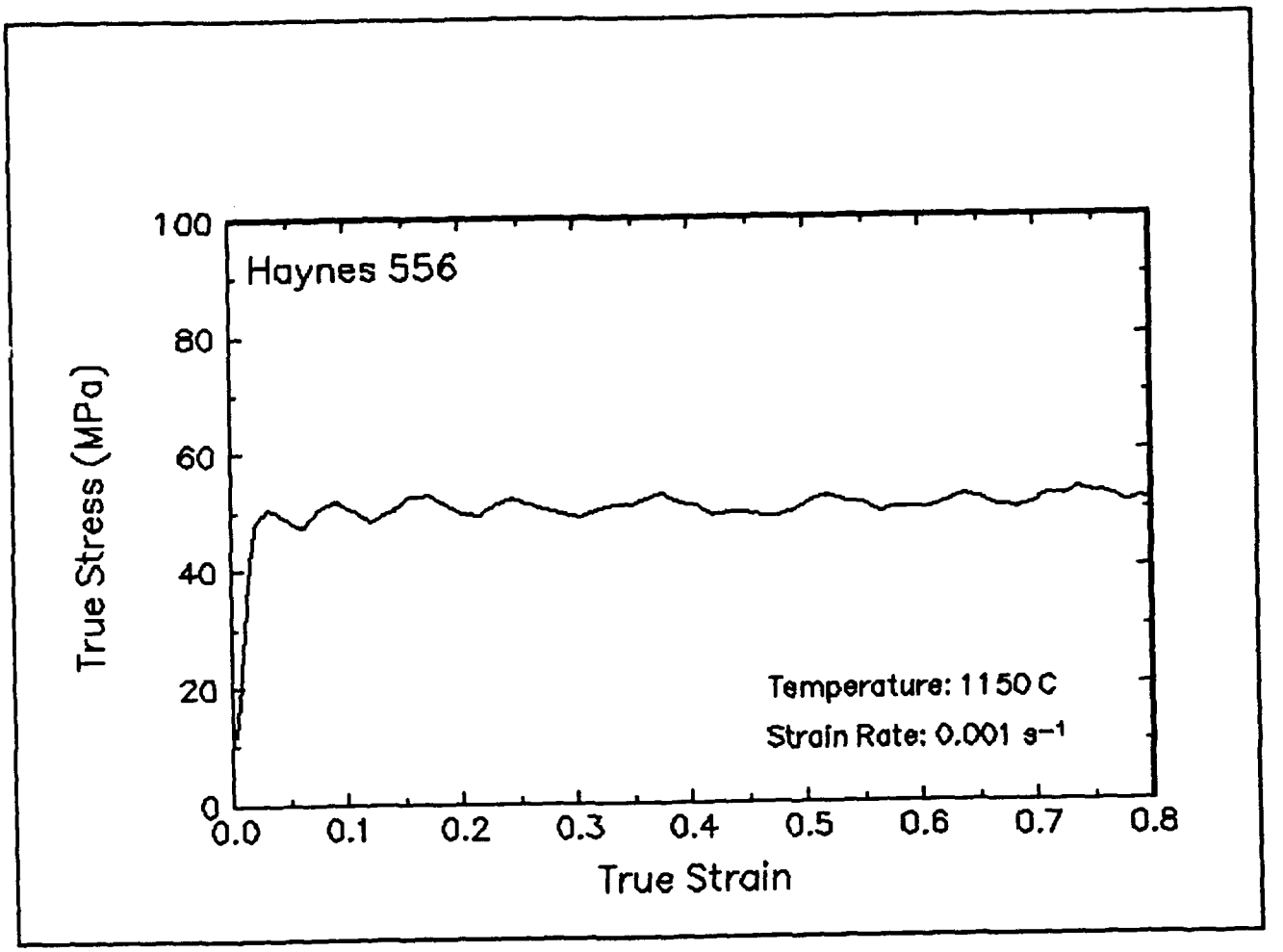

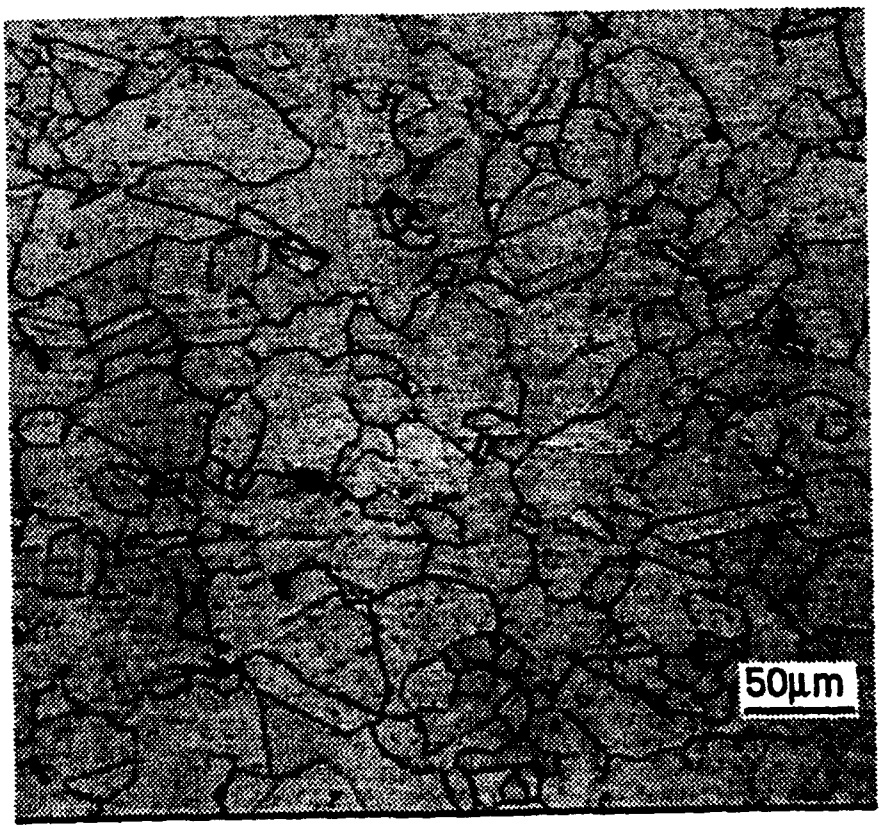

Figure 34. True stress-true strain curve and an optical micrograph from the center of the compressed sample cut through the compression axis, 1150 C and 0.001 s^{-1}.

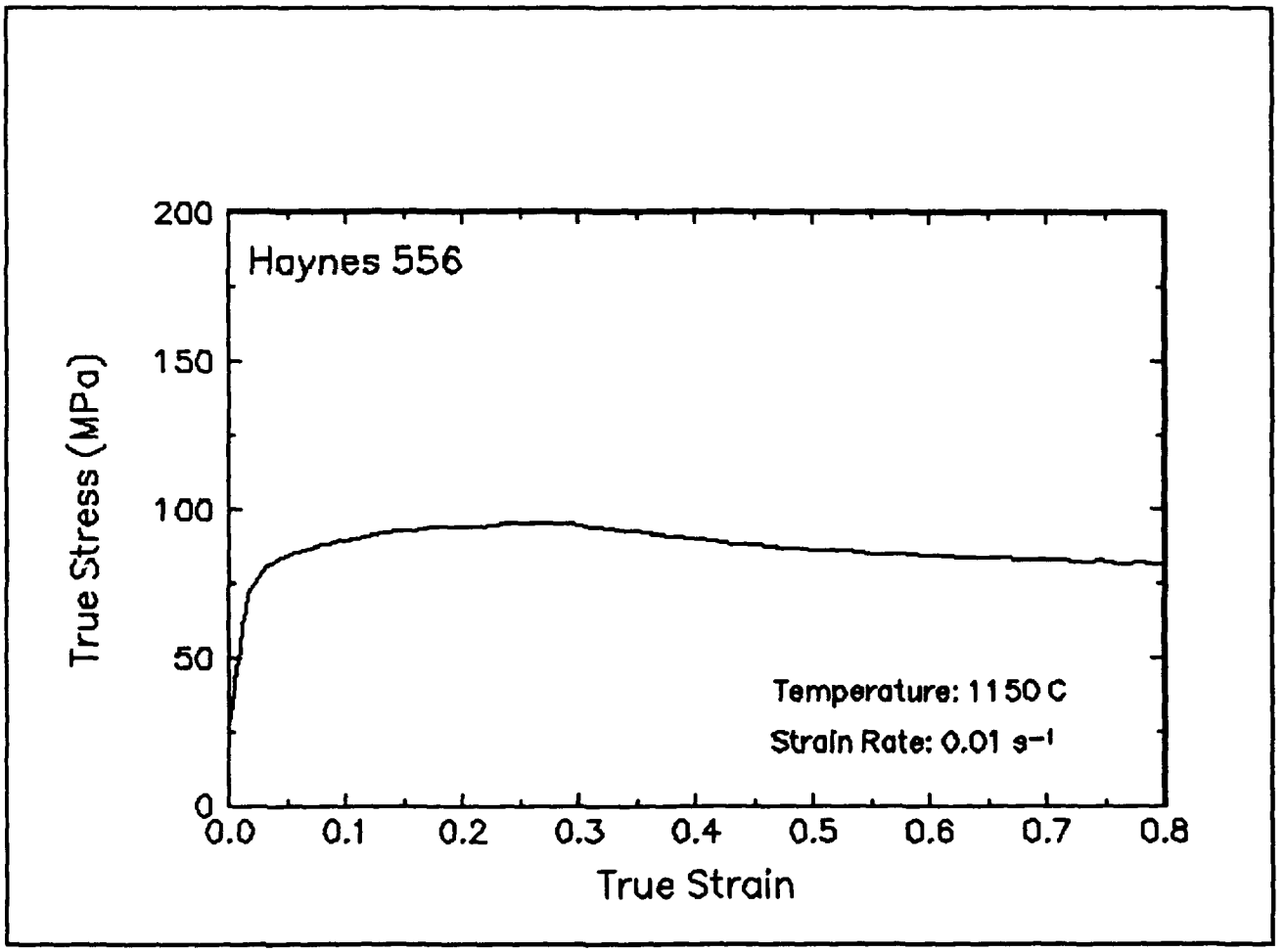

Figure 35. True stress-true strain curve, 1150 C and 0.01 s^{-1}.

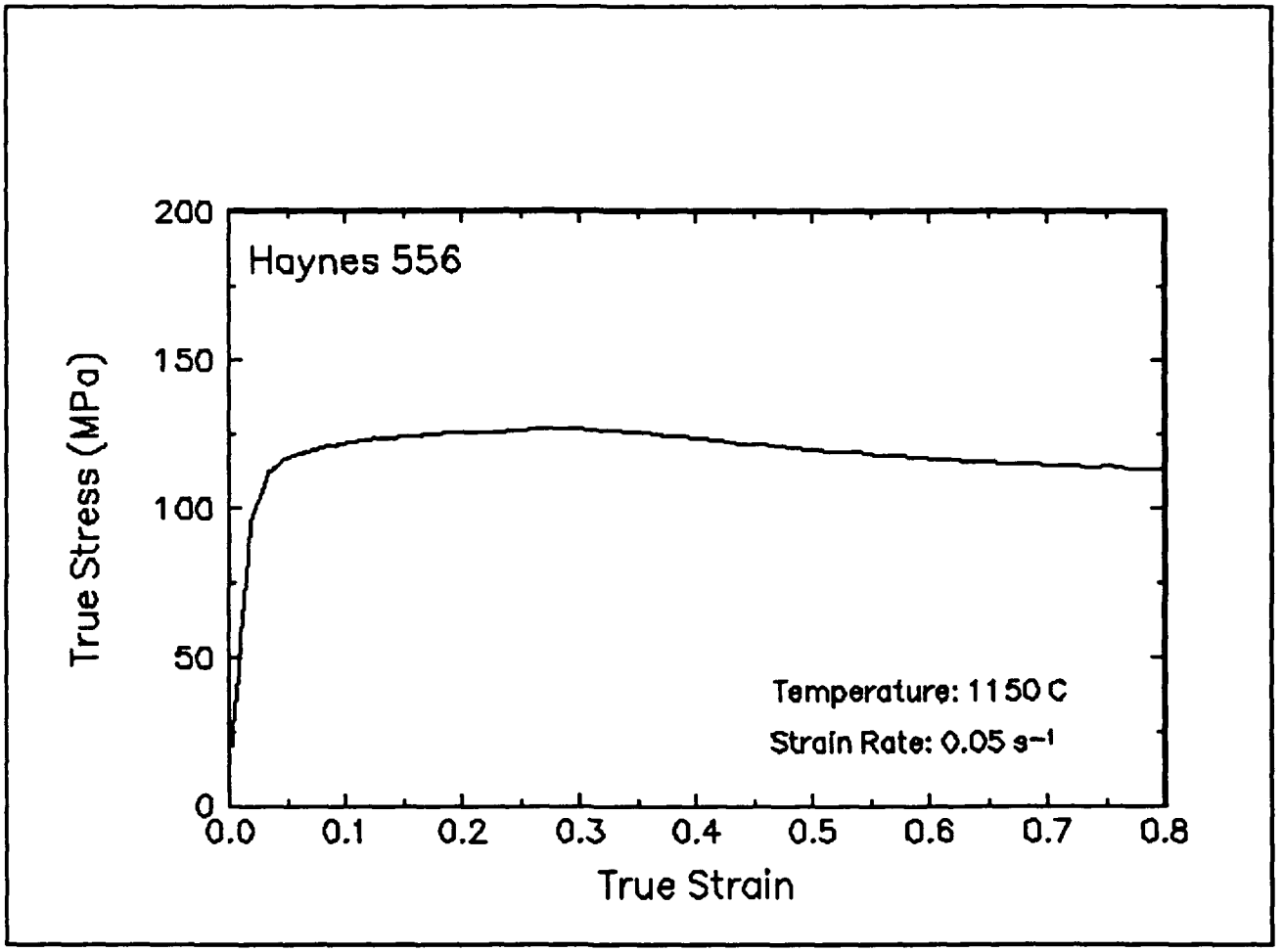

Figure 36. True stress-true strain curve, 1150 C and 0.05 s^{-1}.

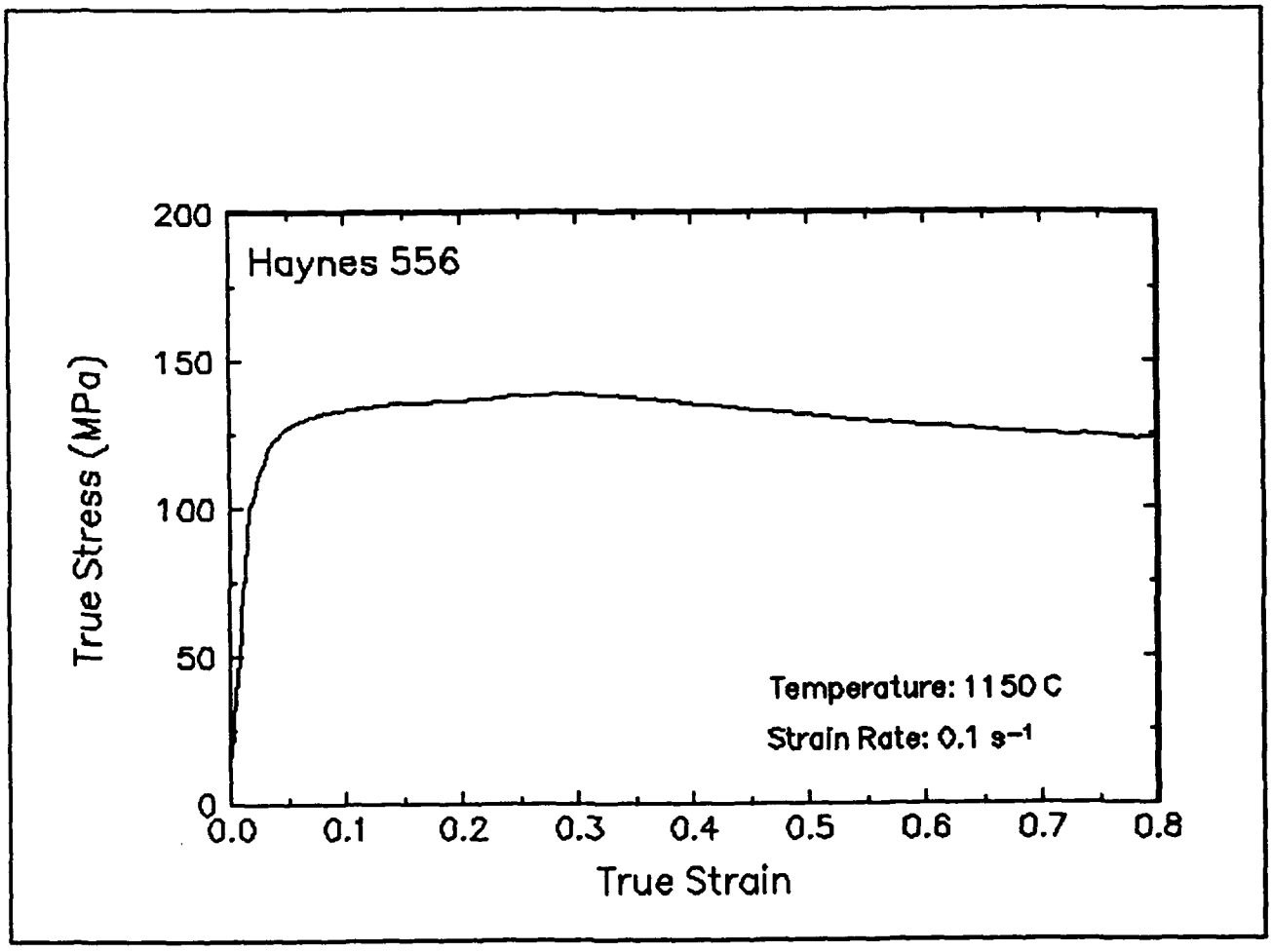

Figure 37. True stress-true strain curve, 1150 C and 0.1 s^{-1}.

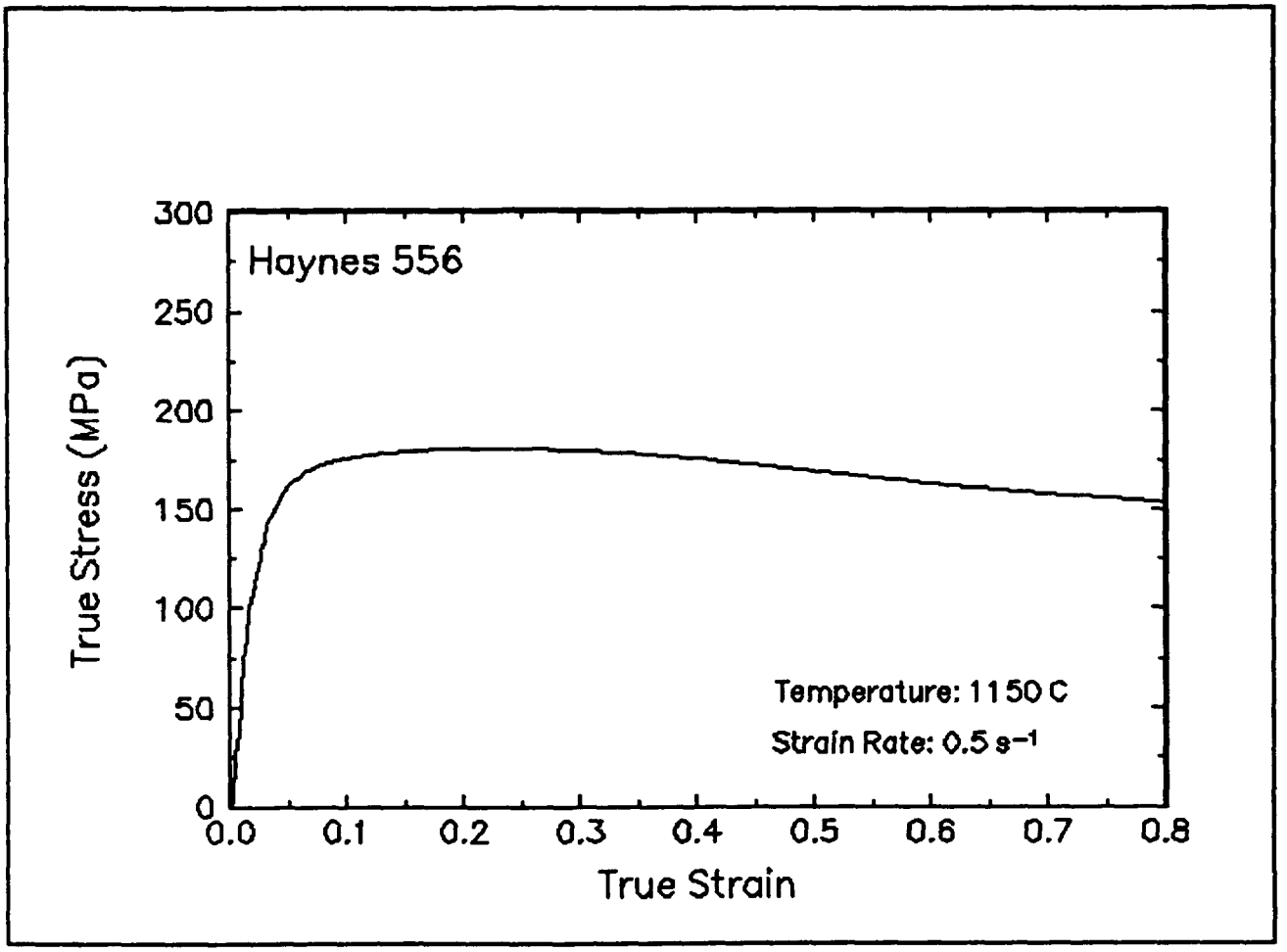

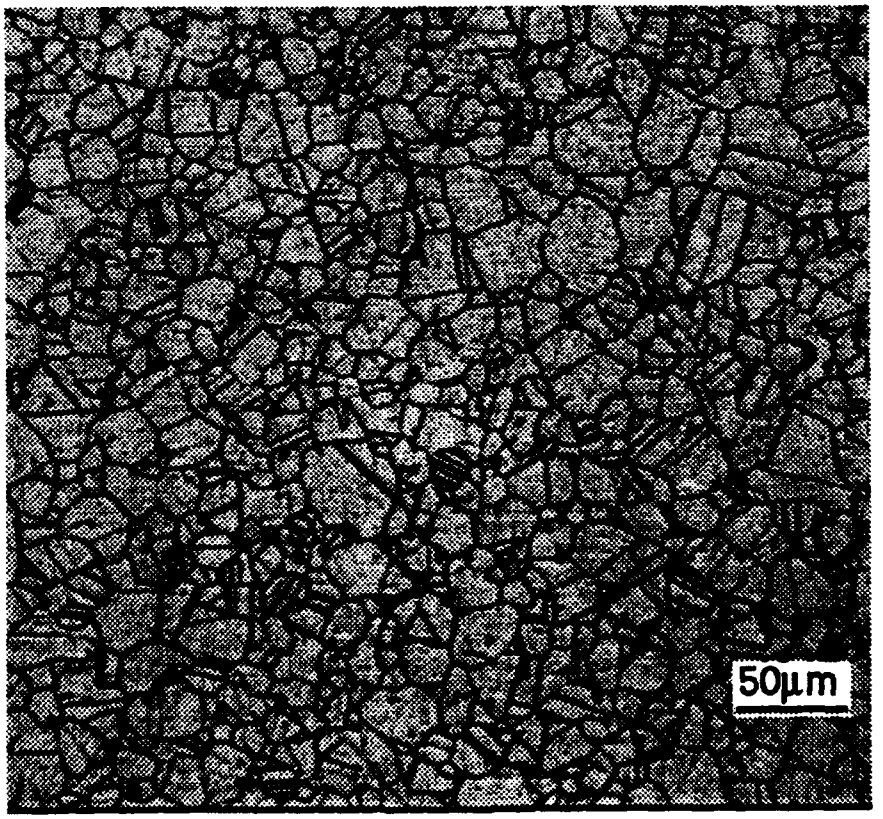

Figure 38. True stress-true strain curve and an optical micrograph from the center of the compressed sample cut through the compression axis, 1150 C and 0.5 s^{-1}.

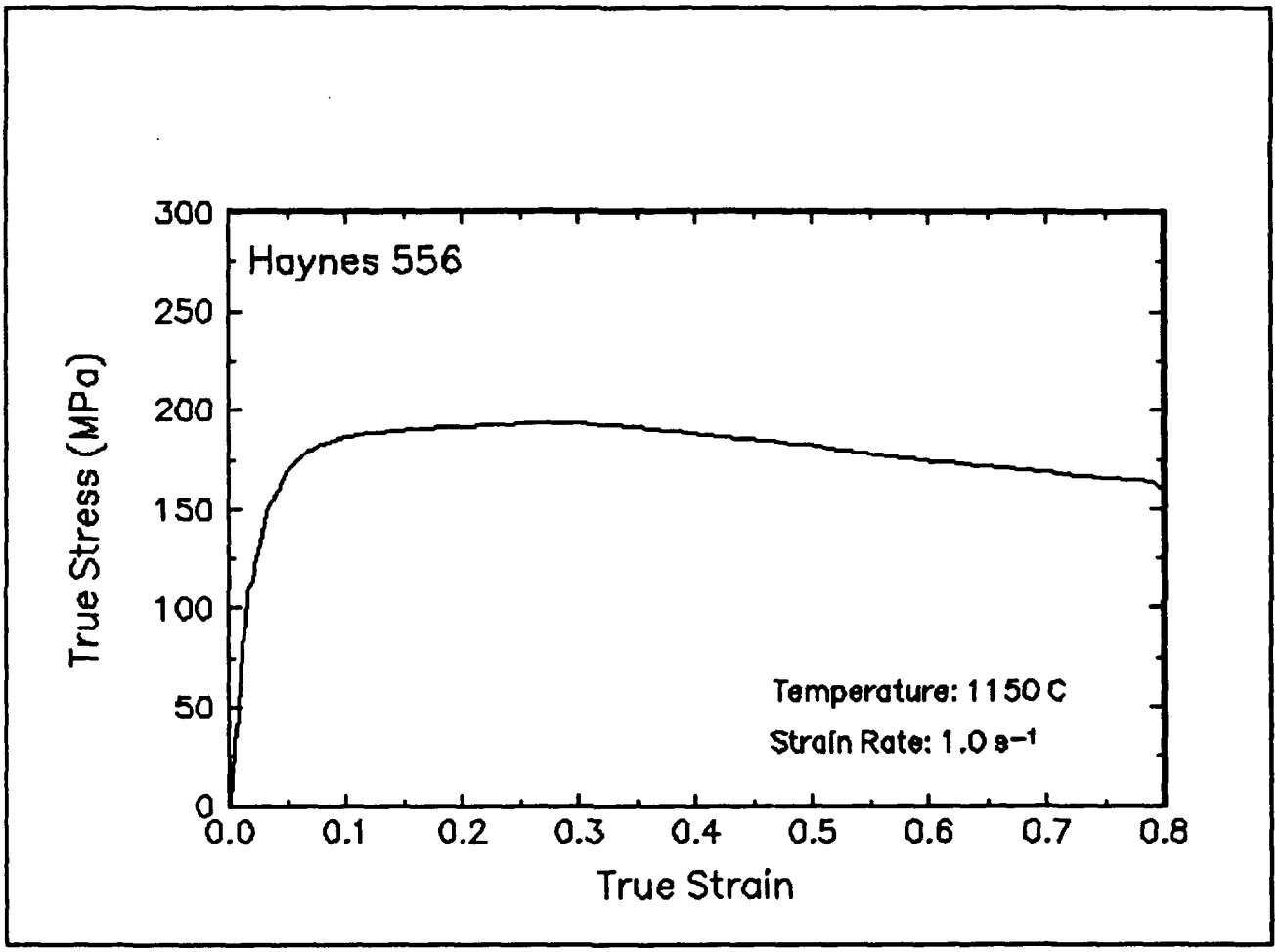

Figure 39. True stress-true strain curve, 1150 C and 1 s^{-1}.

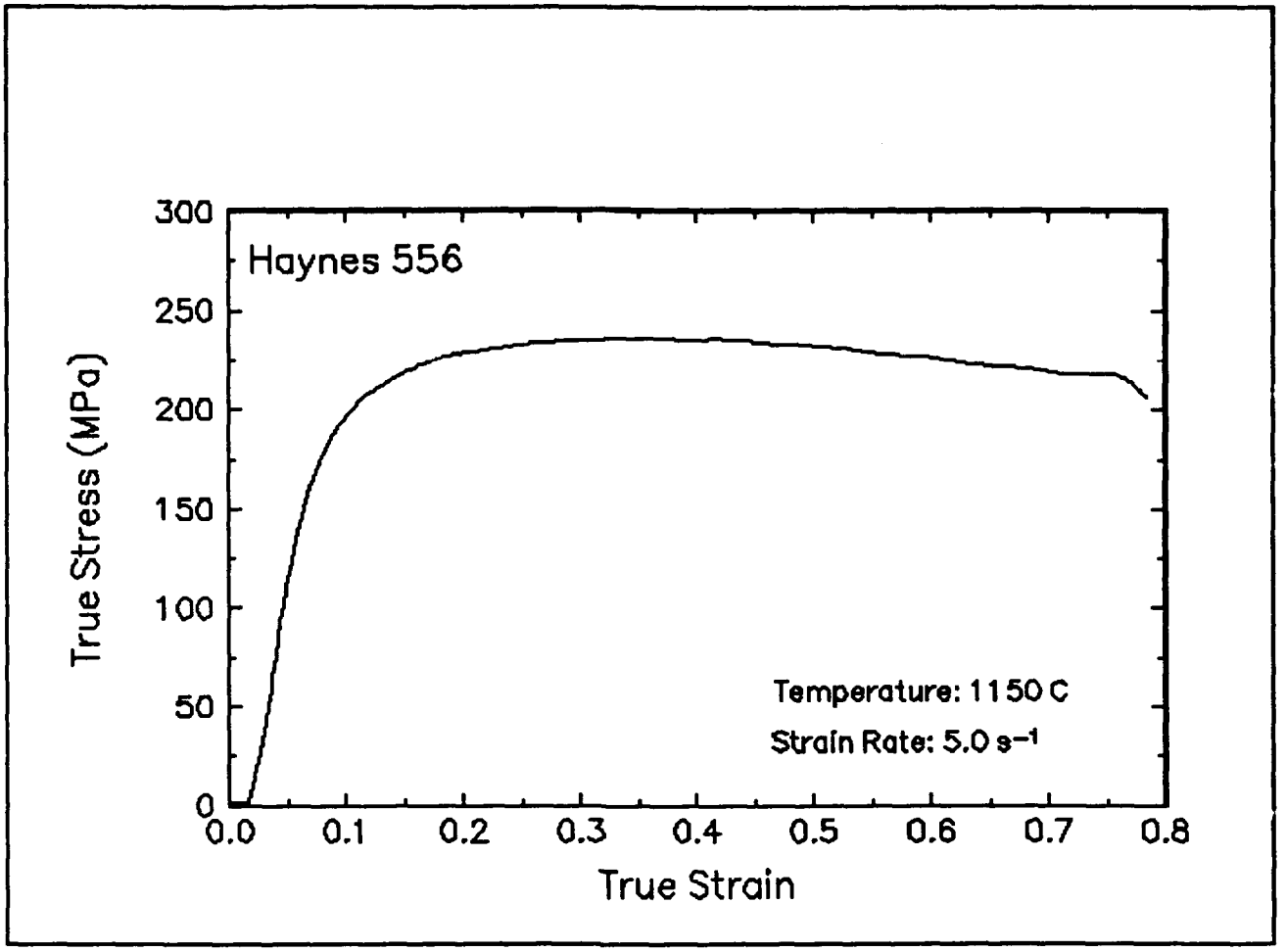

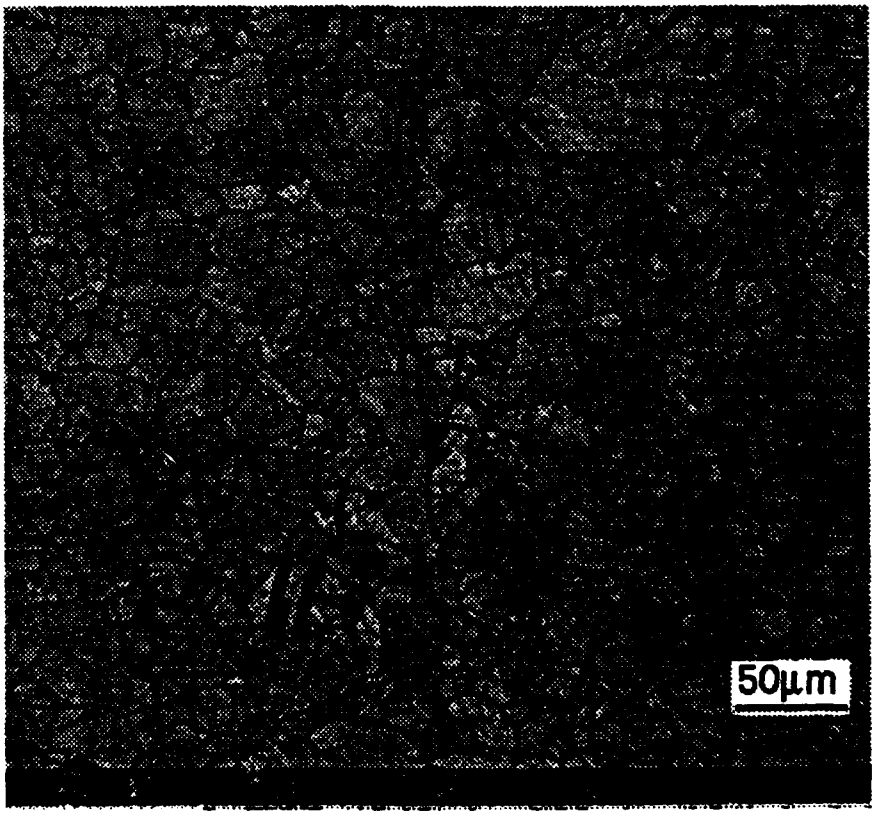

Figure 40. True stress-true strain curve and an optical micrograph from the center of the compressed sample cut through the compression axis, 1150 C and 5 s^{-1}.

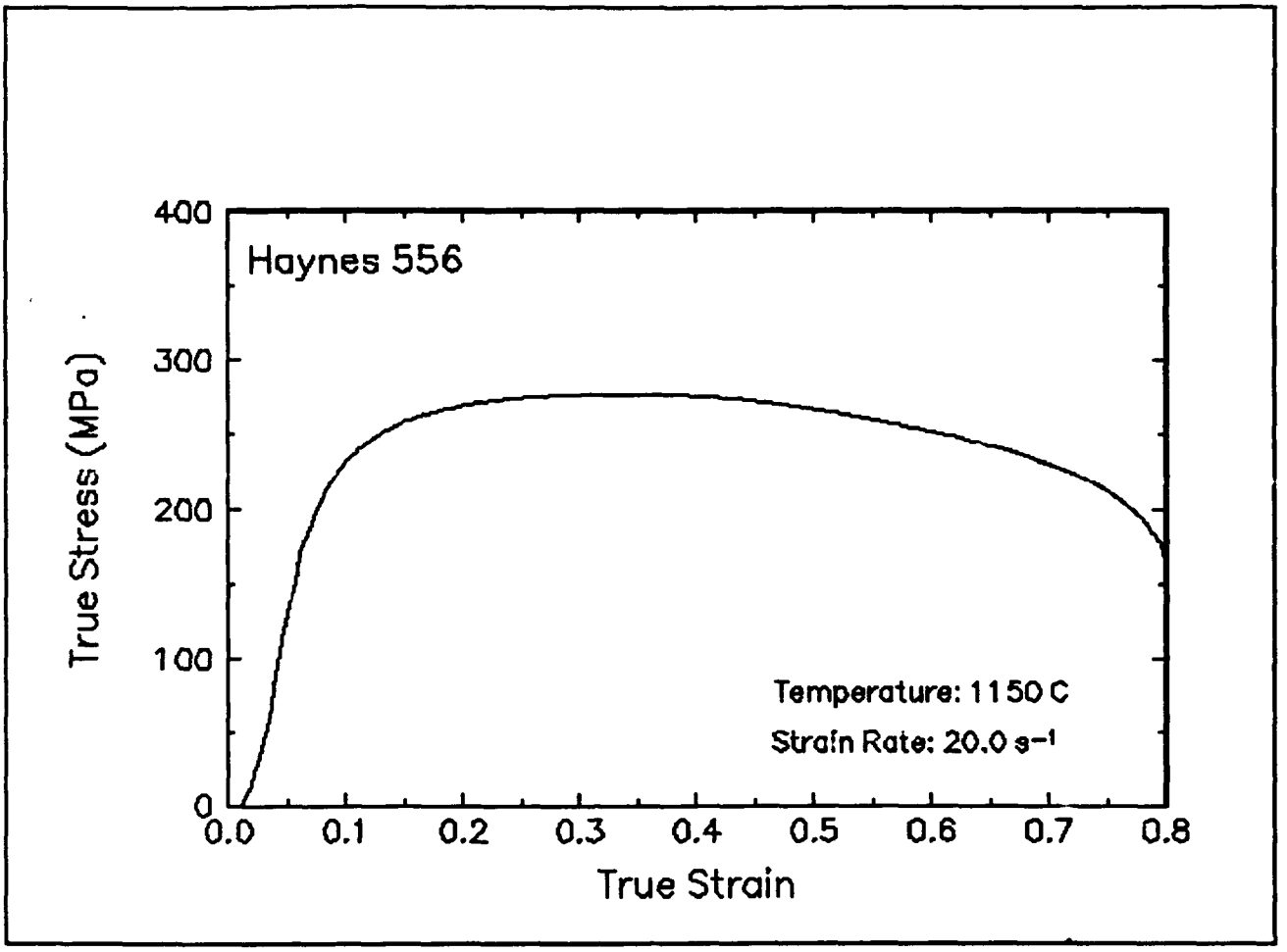

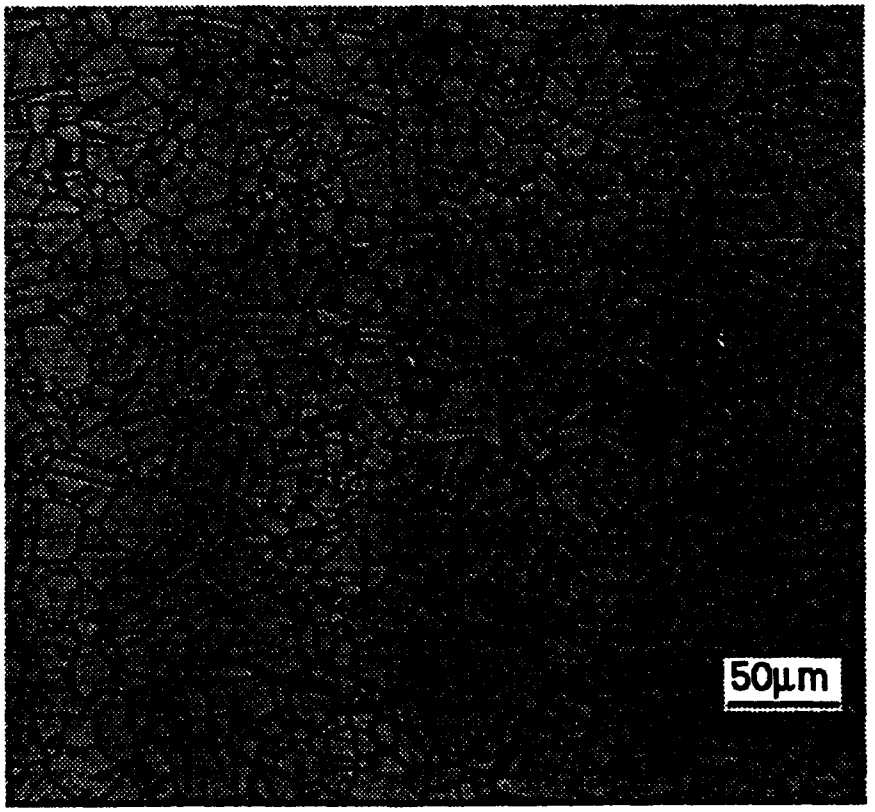

Figure 41. True stress-true strain curve and an optical micrograph from the center of the compressed sample cut through the compression axis, 1150 C and 20 s^{-1}.

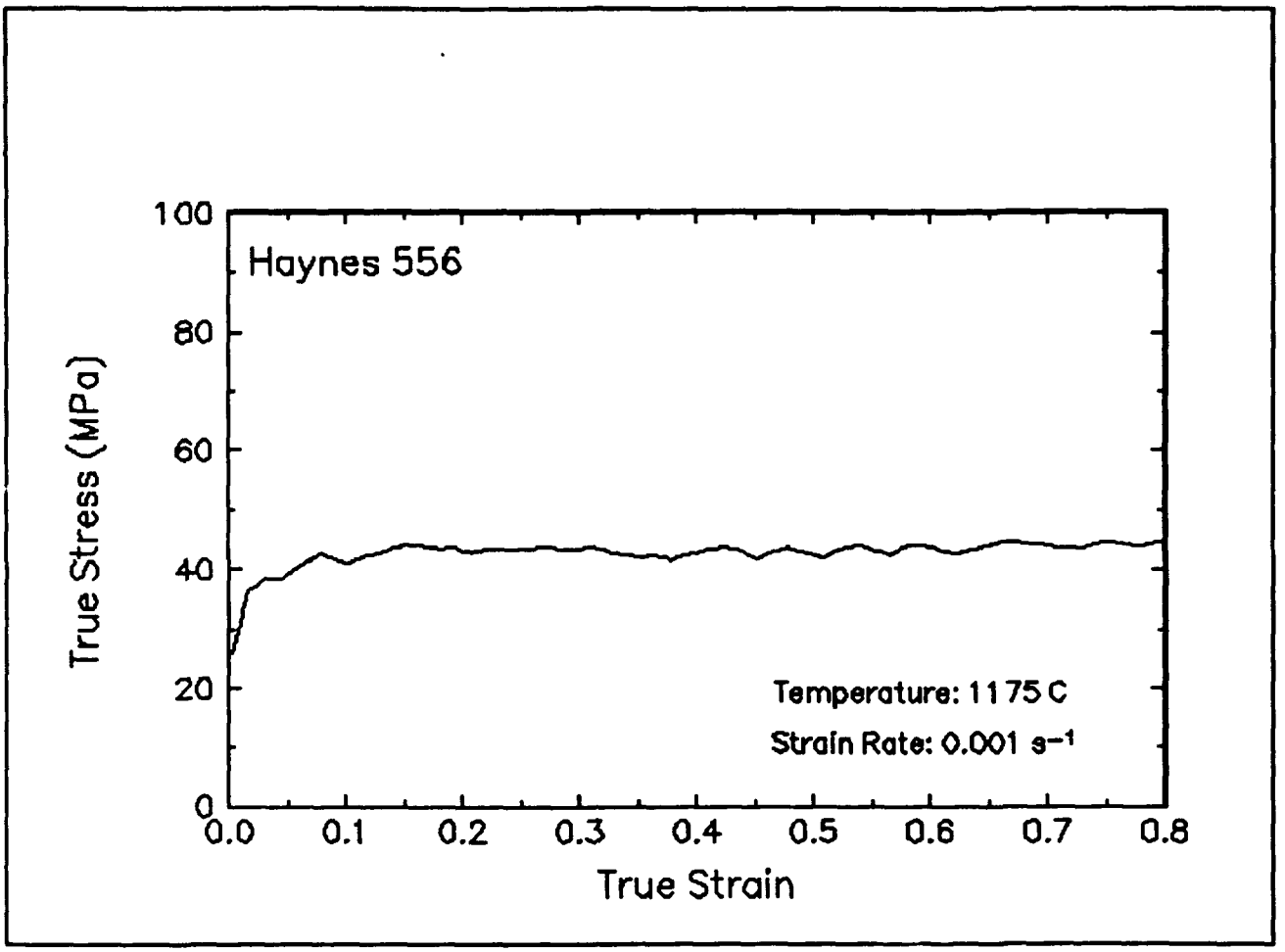

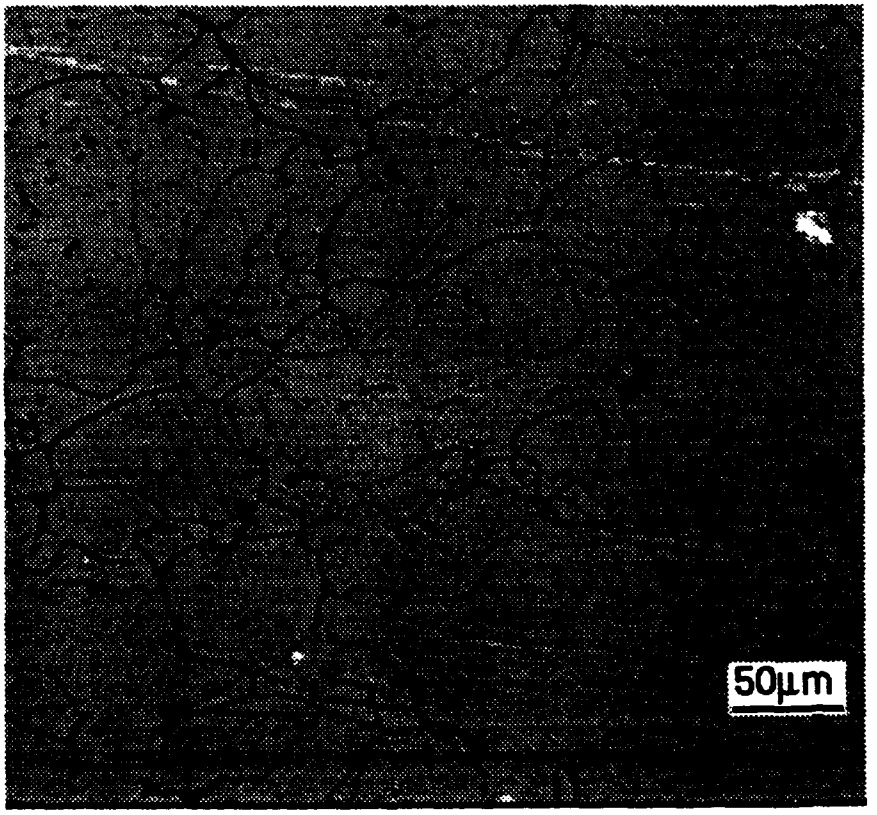

Figure 42. True stress-true strain curve and an optical micrograph from the center of the compressed sample cut through the compression axis, 1175 C and 0.001 s^{-1}.

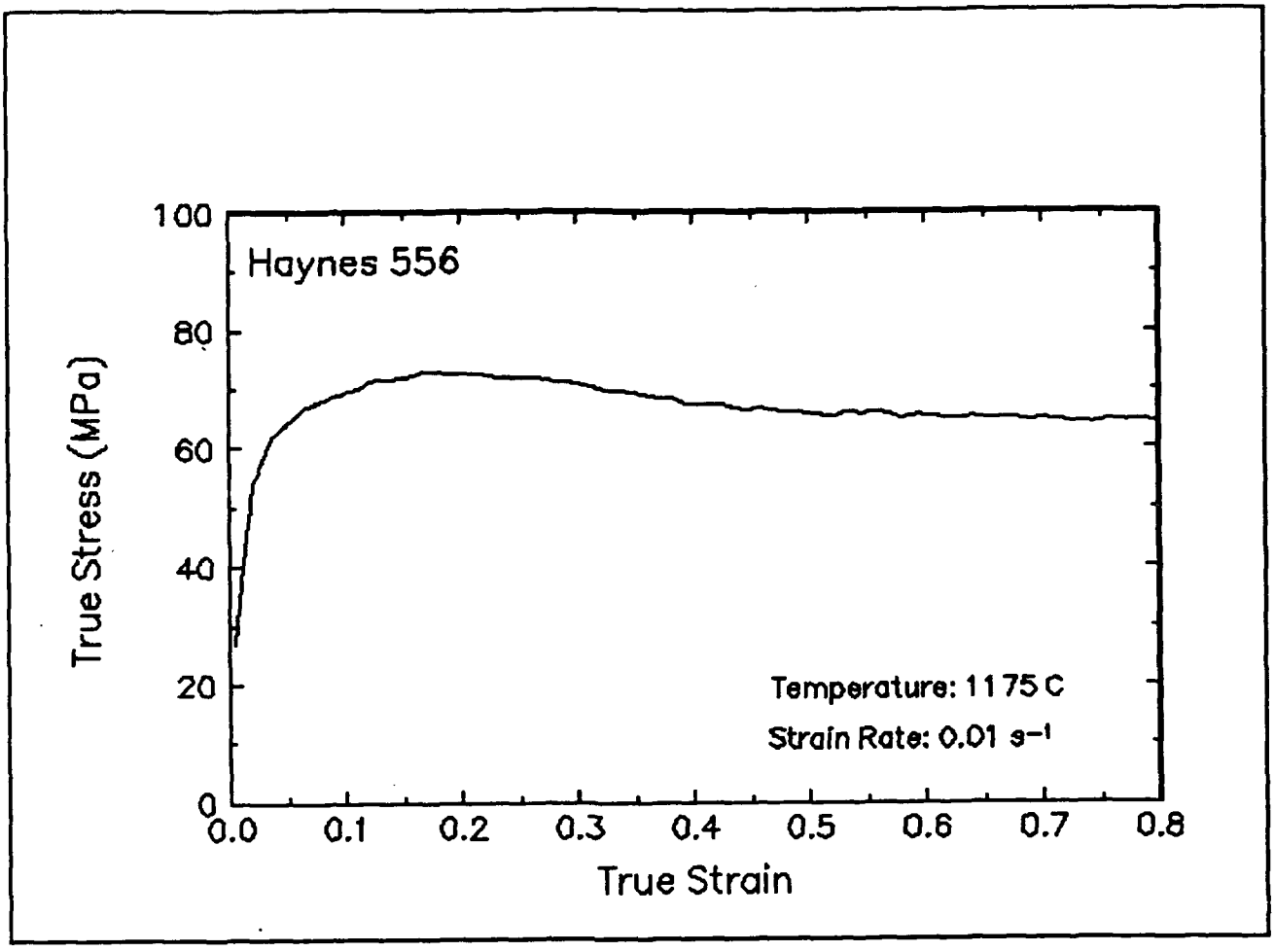

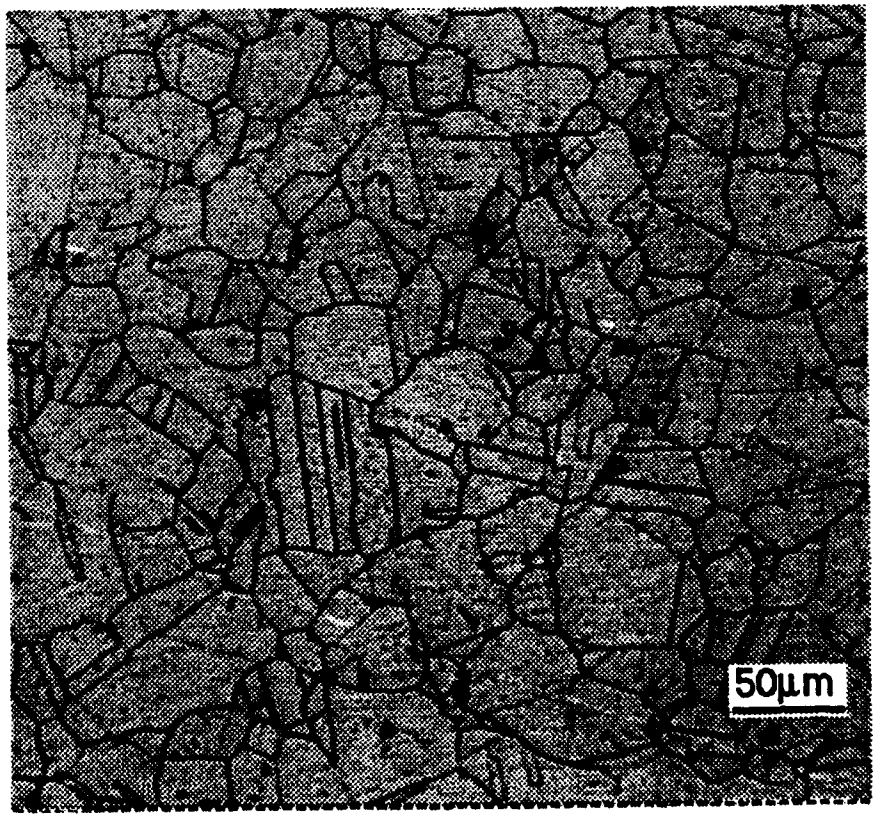

Figure 43. True stress-true strain curve and an optical micrograph from the center of the compressed sample cut through the compression axis, 1175 C and 0.01 s^{-1}.

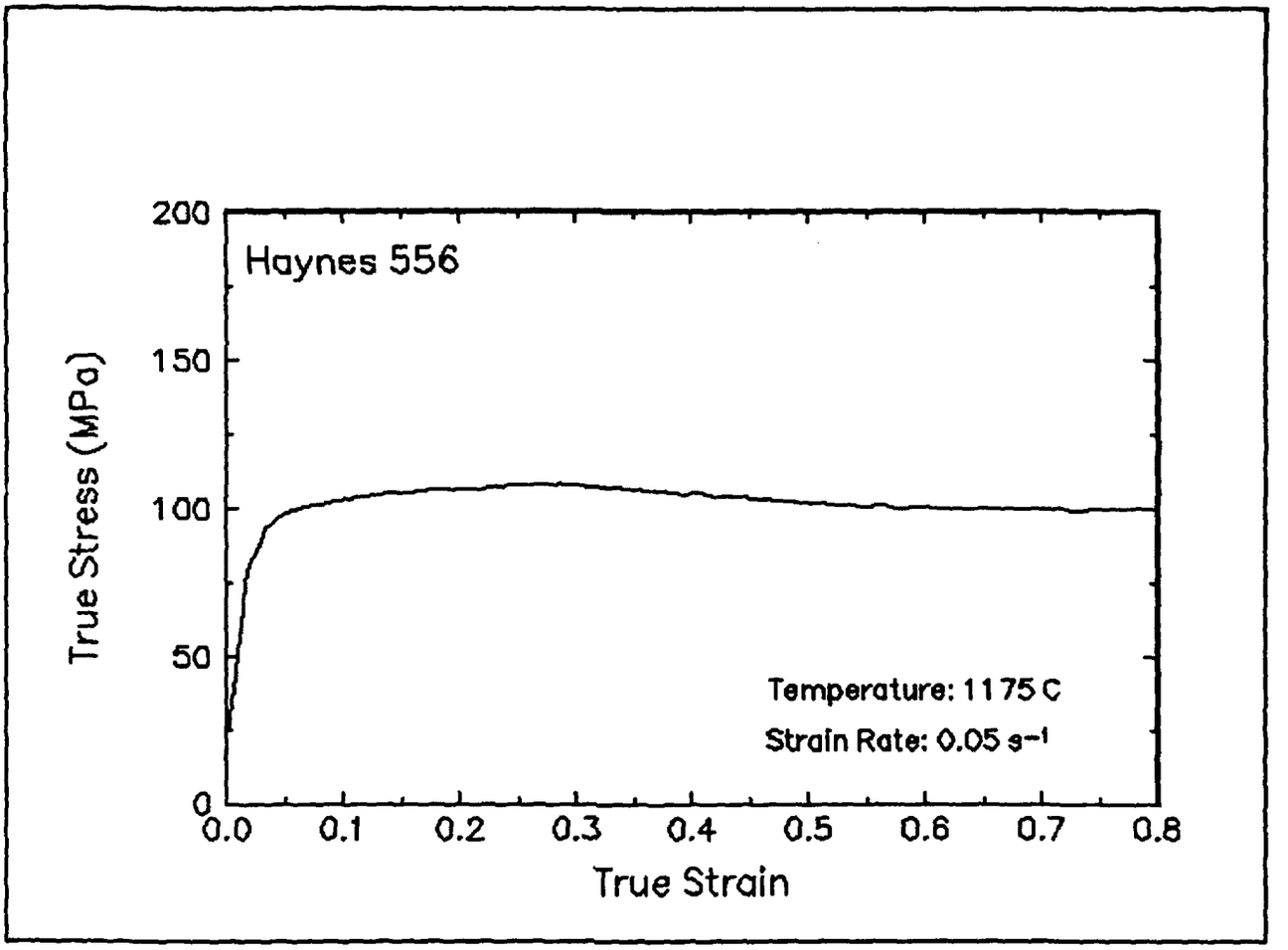

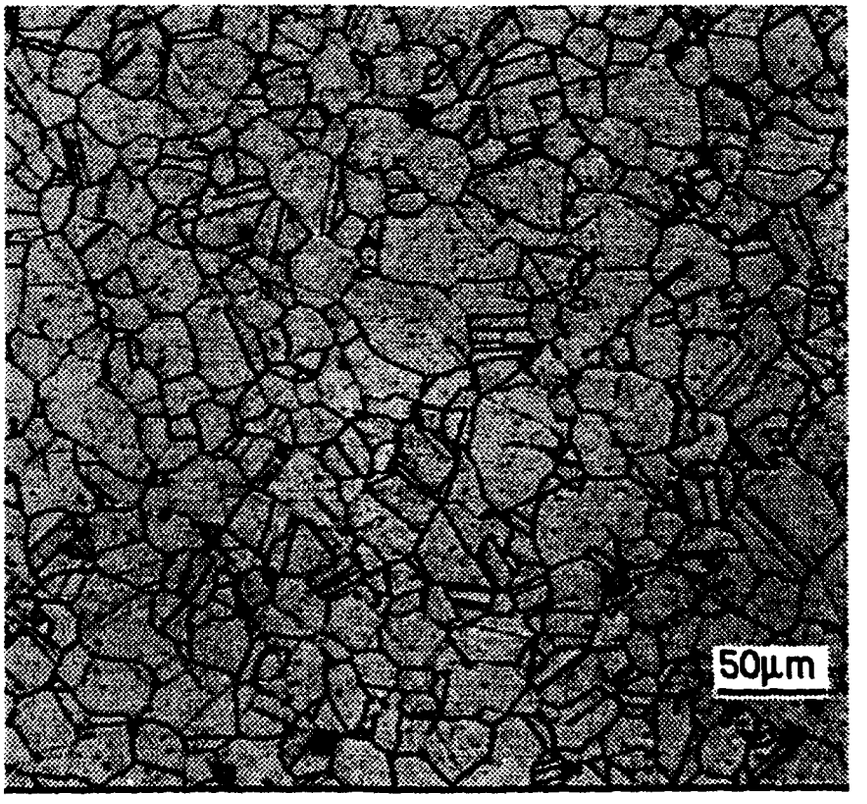

Figure 44. True stress-true strain curve and an optical micrograph from the center of the compressed sample cut through the compression axis, 1175 C and 0.05 s^{-1}.

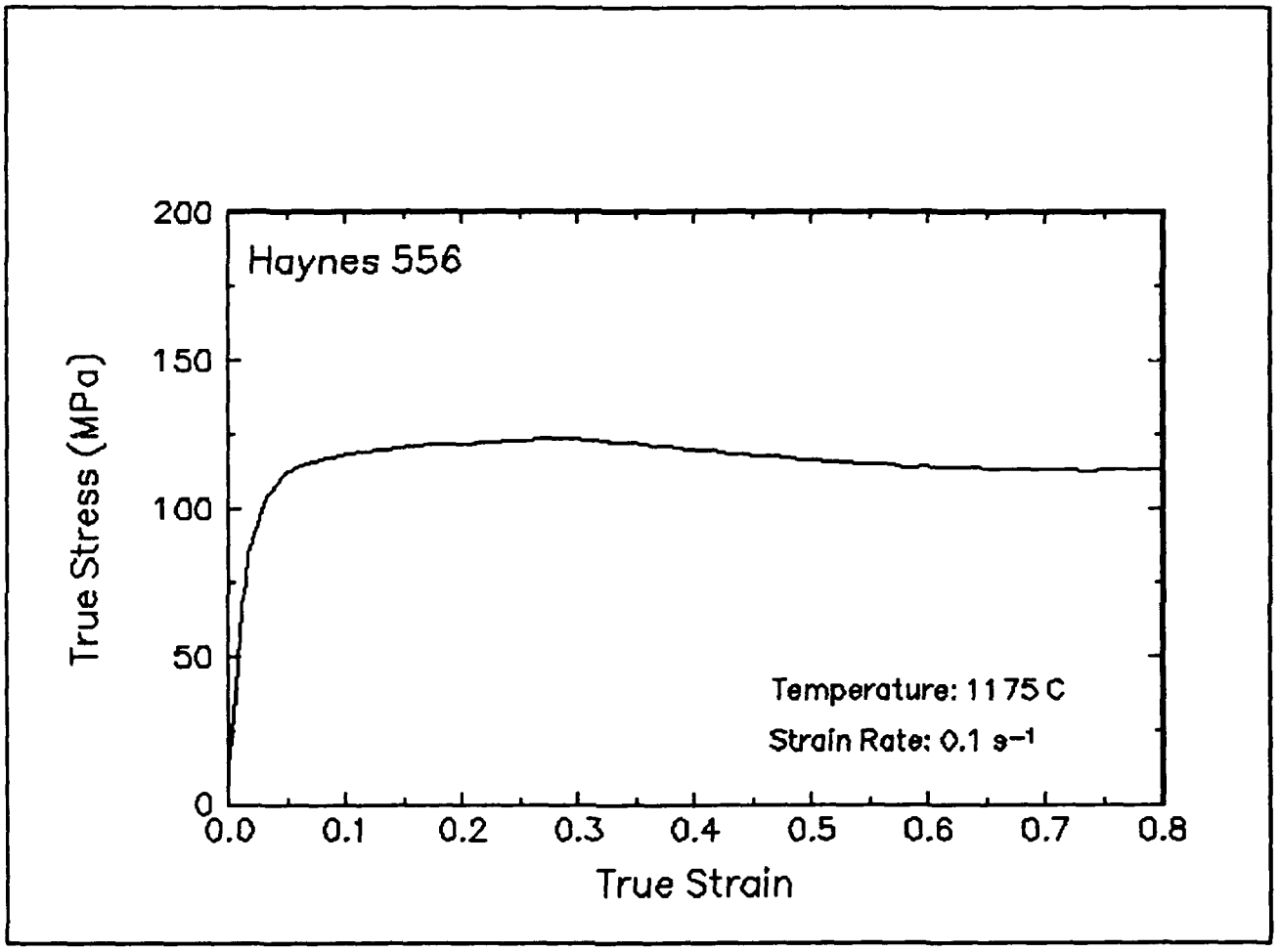

Figure 45. True stress-true strain curve, 1175 C and 0.1 s^{-1}.

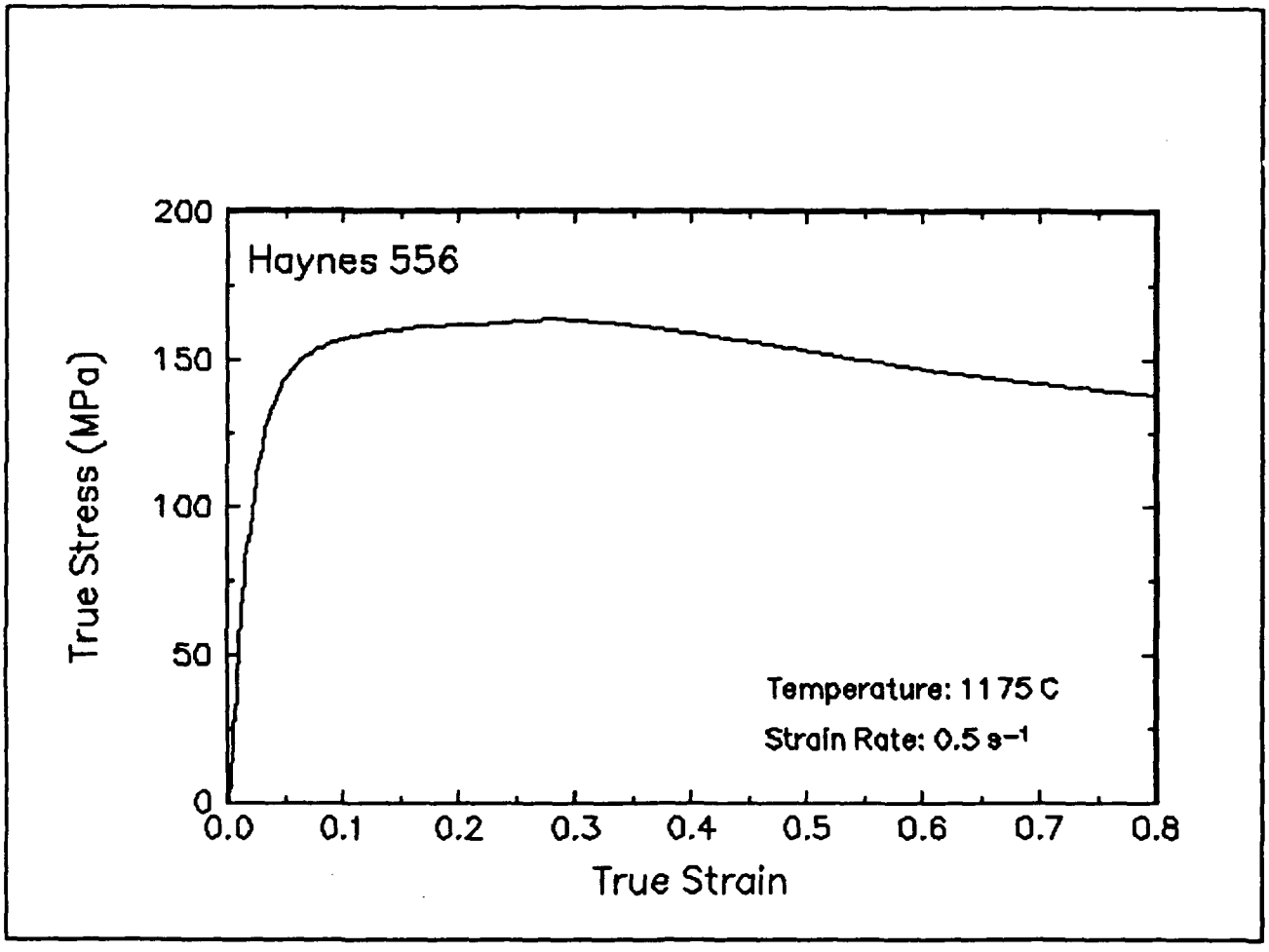

Figure 46. True stress-true strain curve, 1175 C and 0.5 s^{-1}.

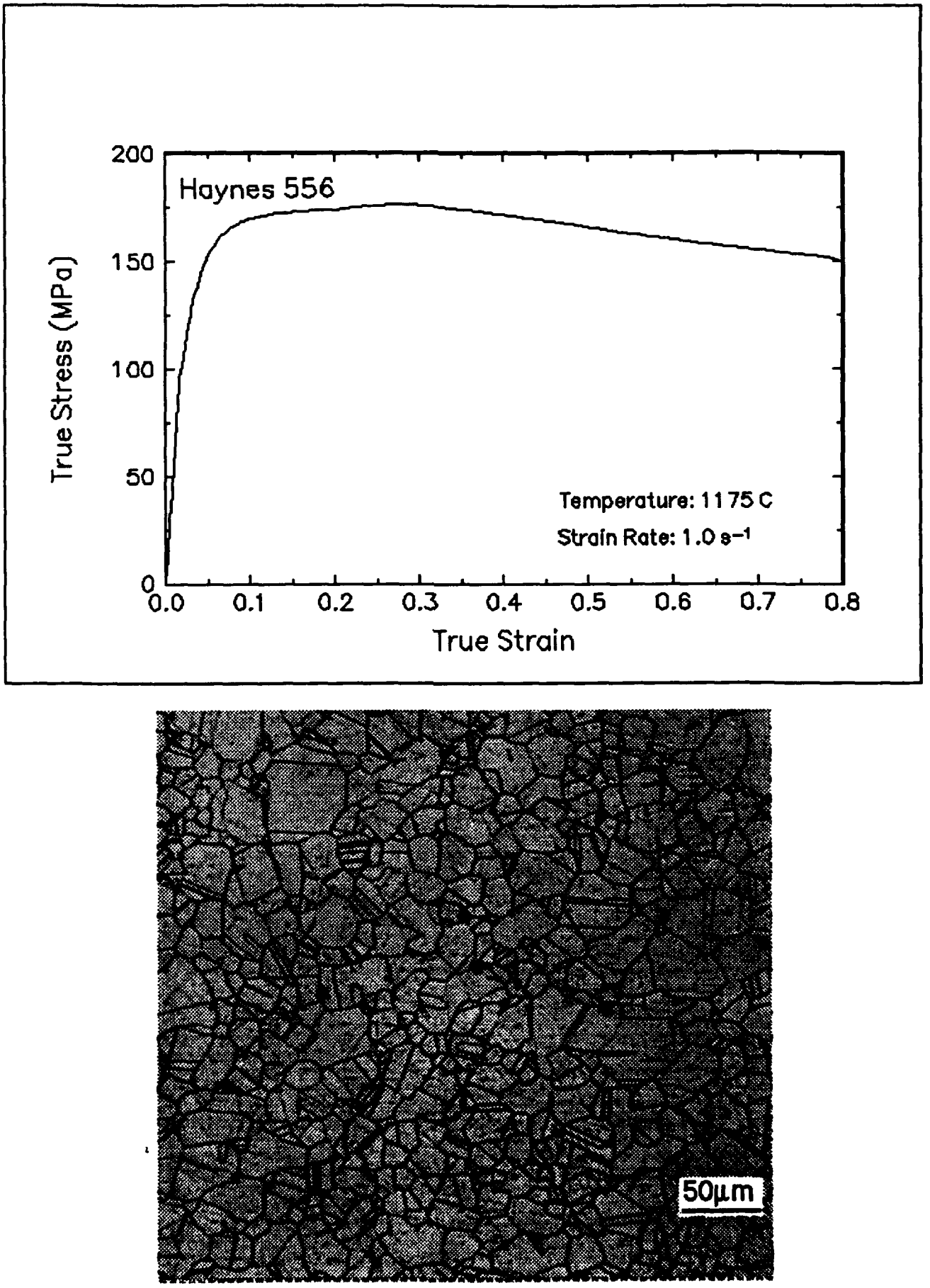

Figure 47. True stress-true strain curve and an optical micrograph from the center of the compressed sample cut through the compression axis, 1175 C and 1 s^{-1}.

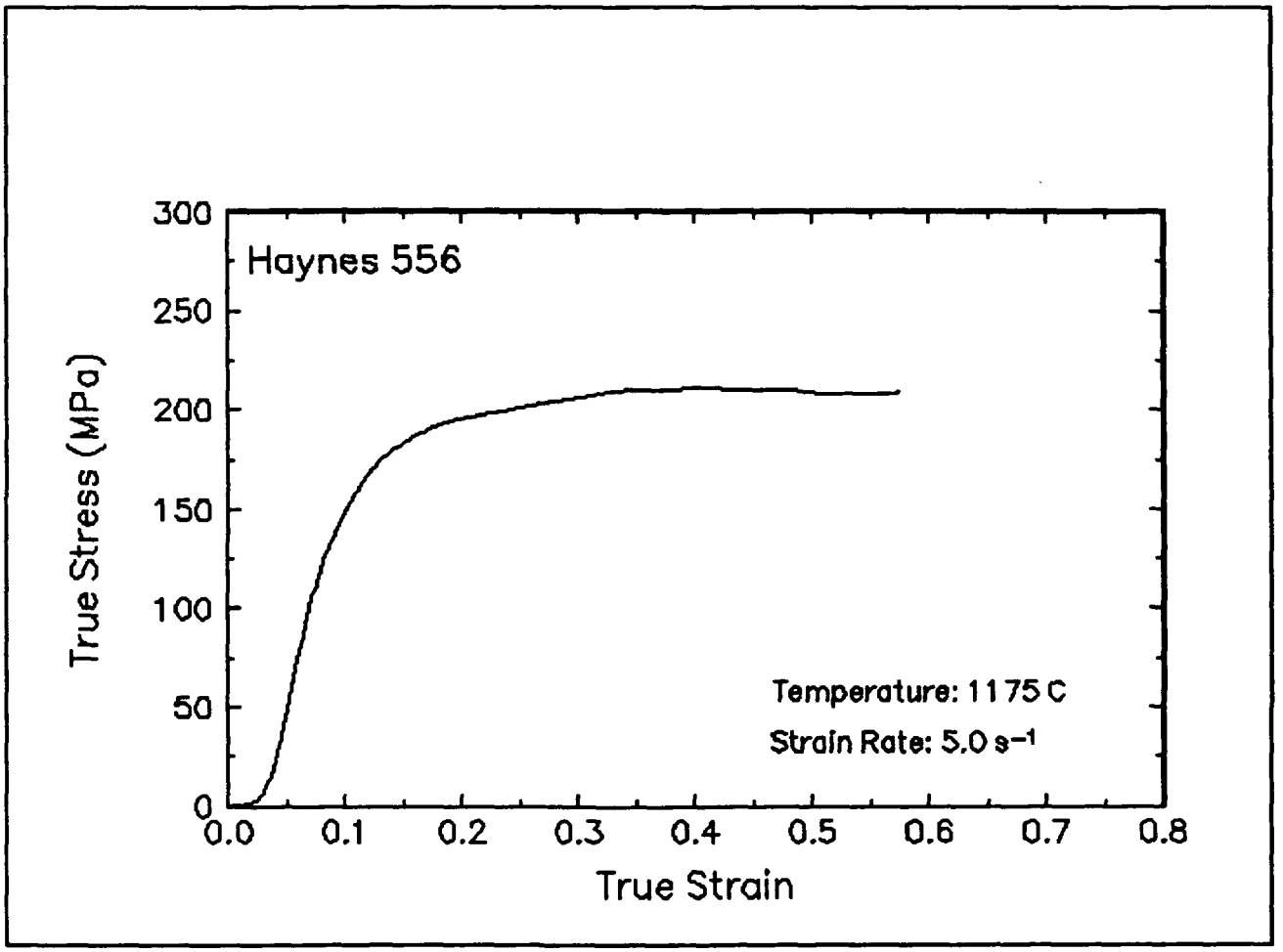

Figure 48. True stress-true strain curve, 1175 C and 5 s^{-1}.

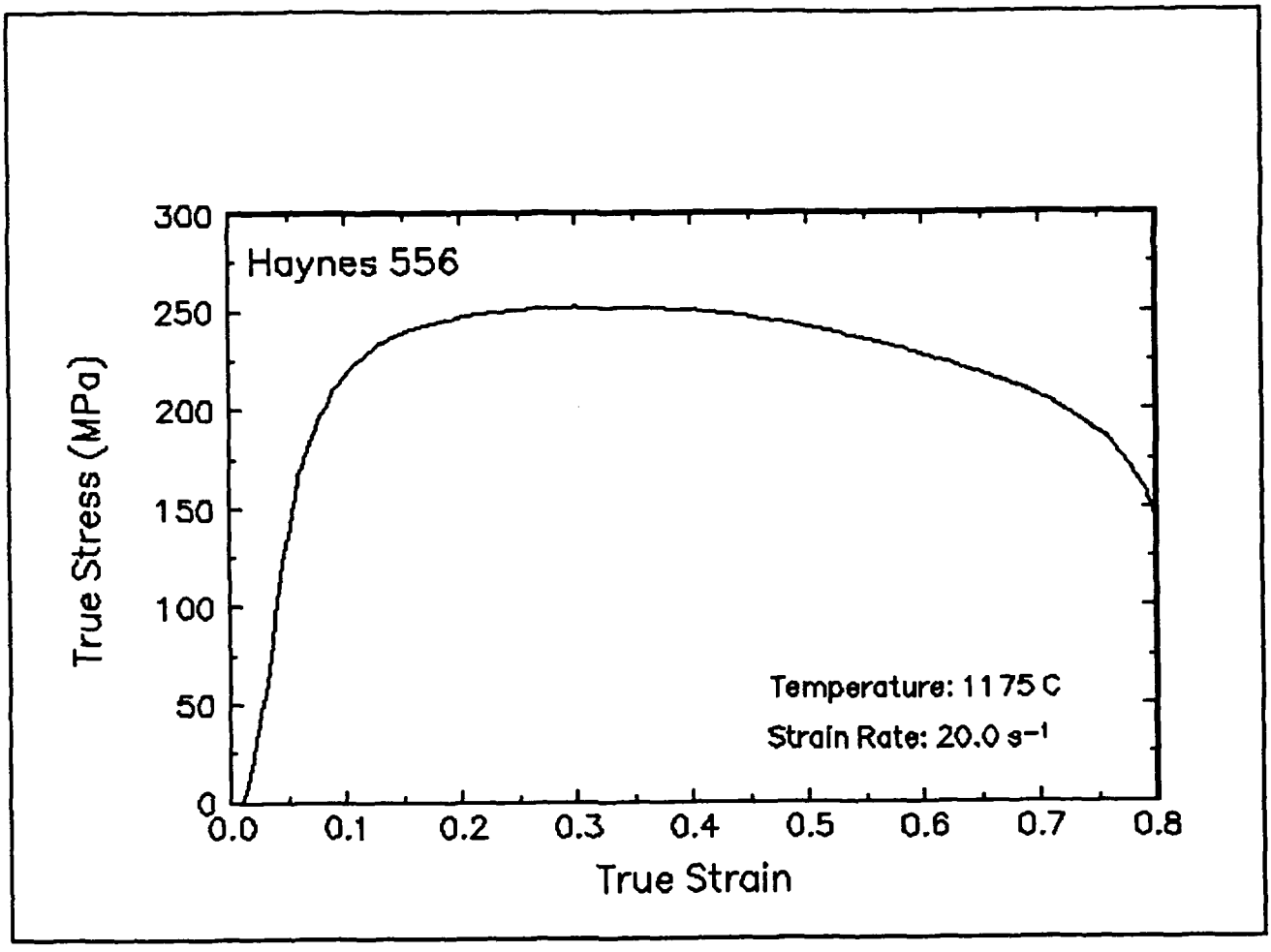

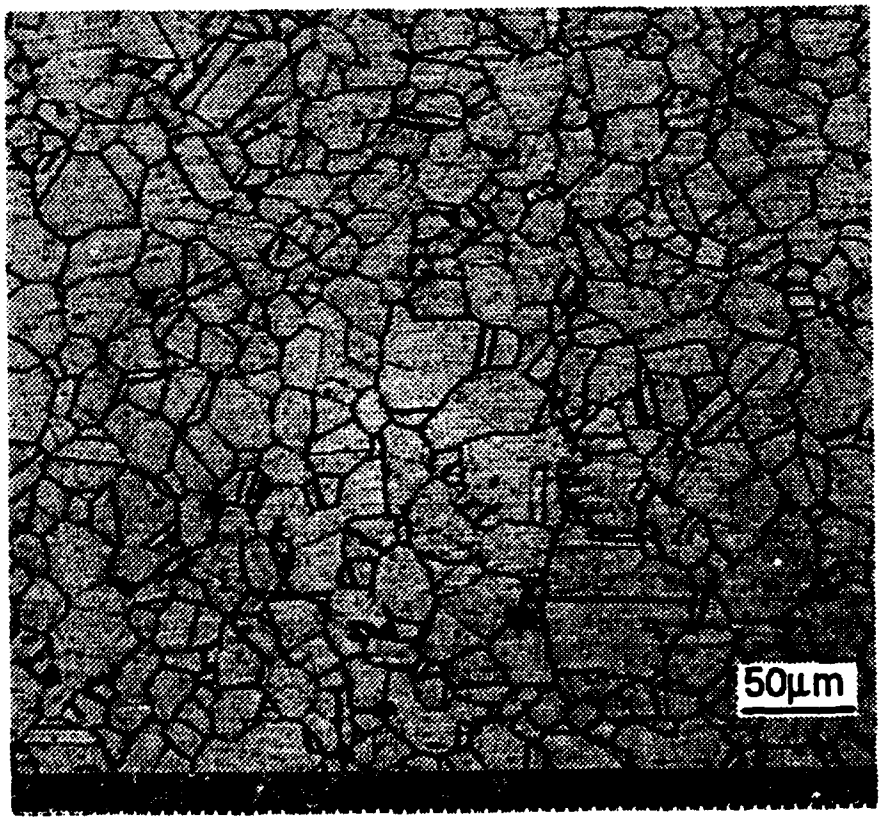

Figure 49. True stress-true strain curve and an optical micrograph from the center of the compressed sample cut through the compression axis, 1175 C and 20 s^{-1}.

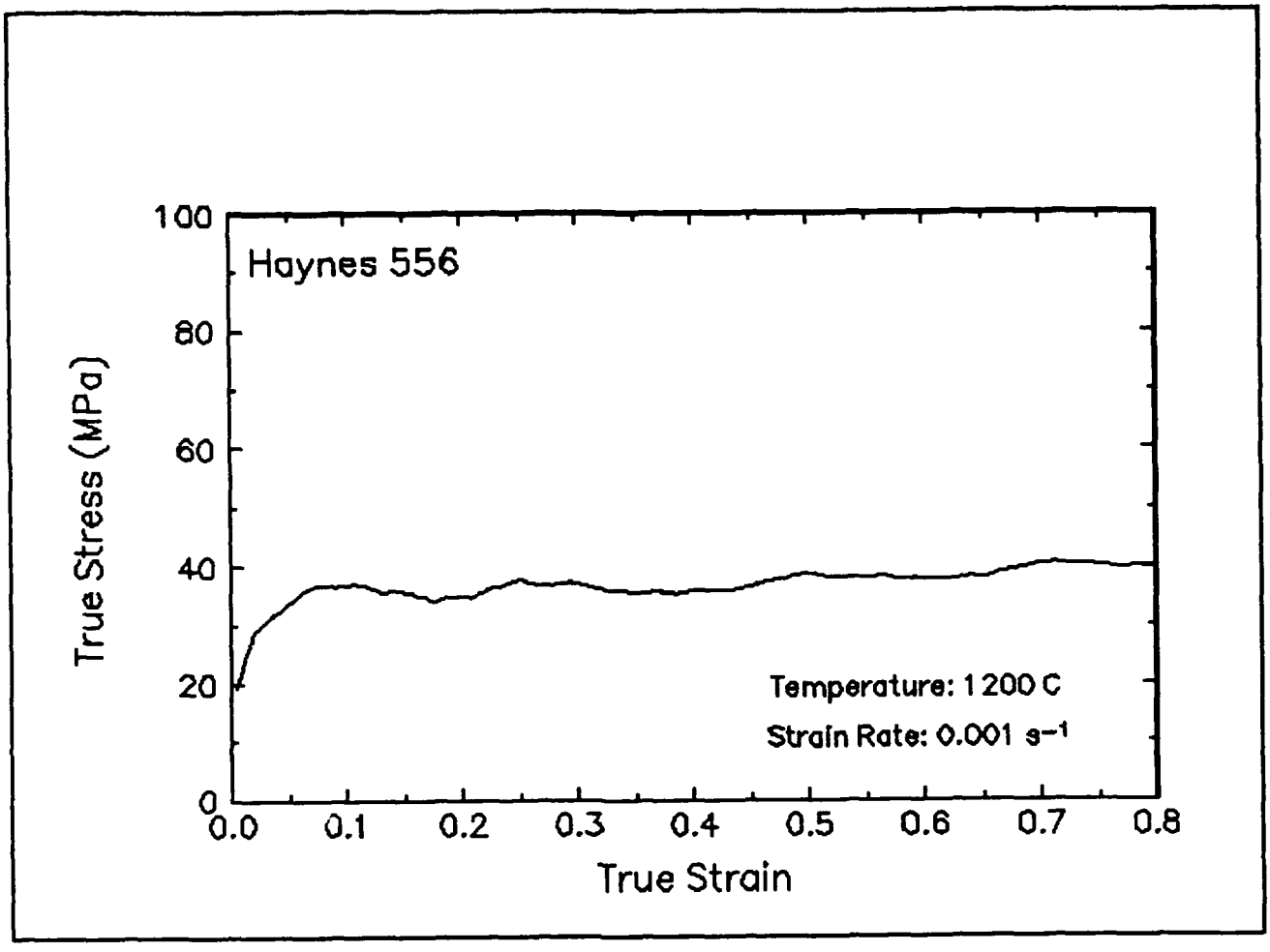

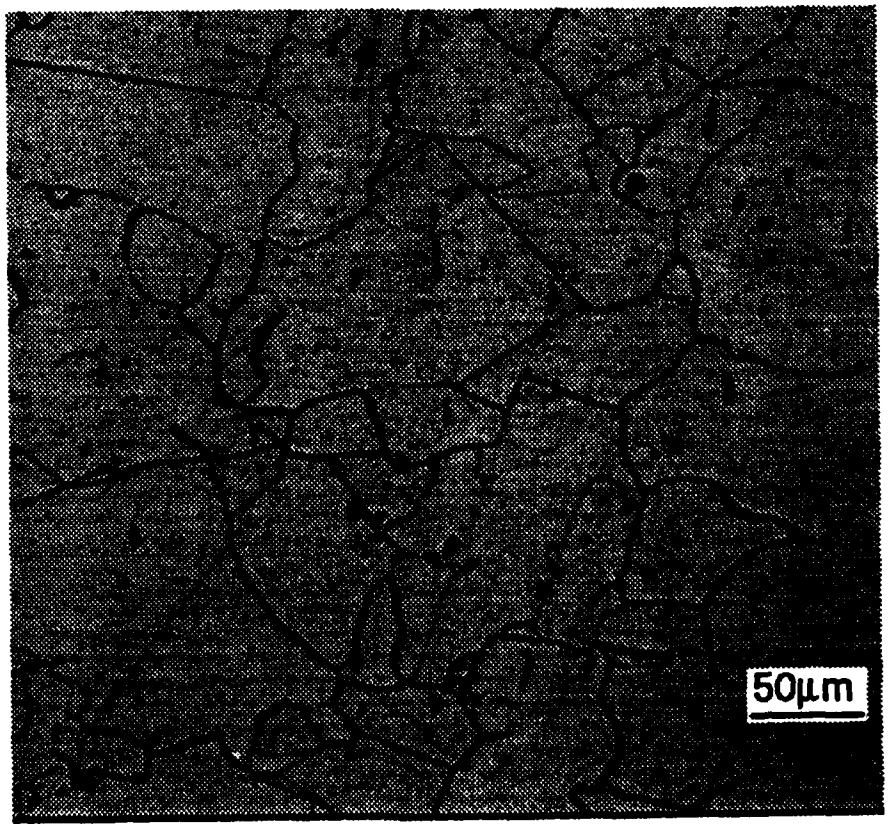

Figure 50. True stress-true strain curve and an optical micrograph from the center of the compressed sample cut through the compression axis, 1200 C and 0.001 s^{-1}.

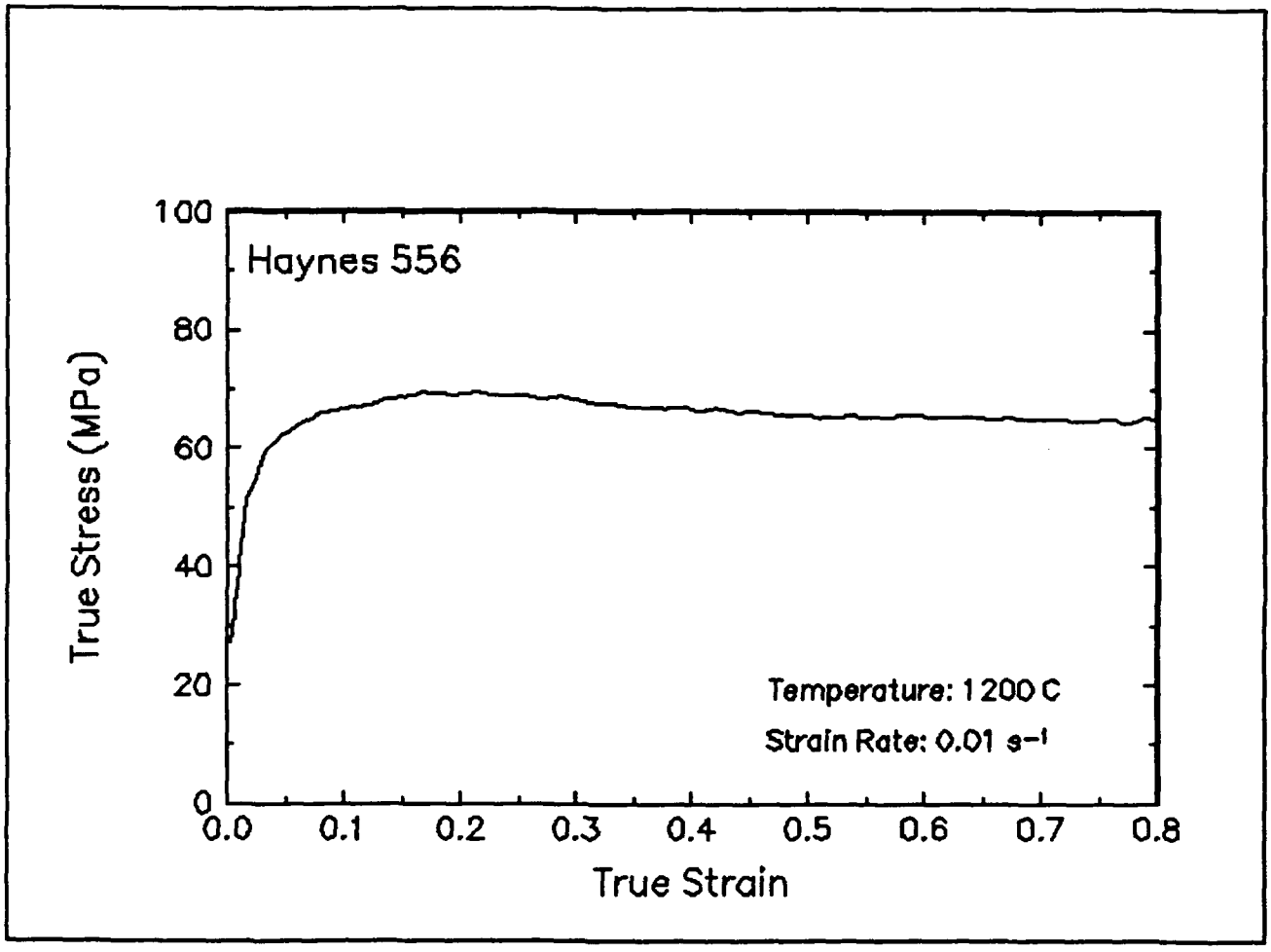

Figure 51. True stress-true strain curve, 1200 C and 0.01 s^{-1}.

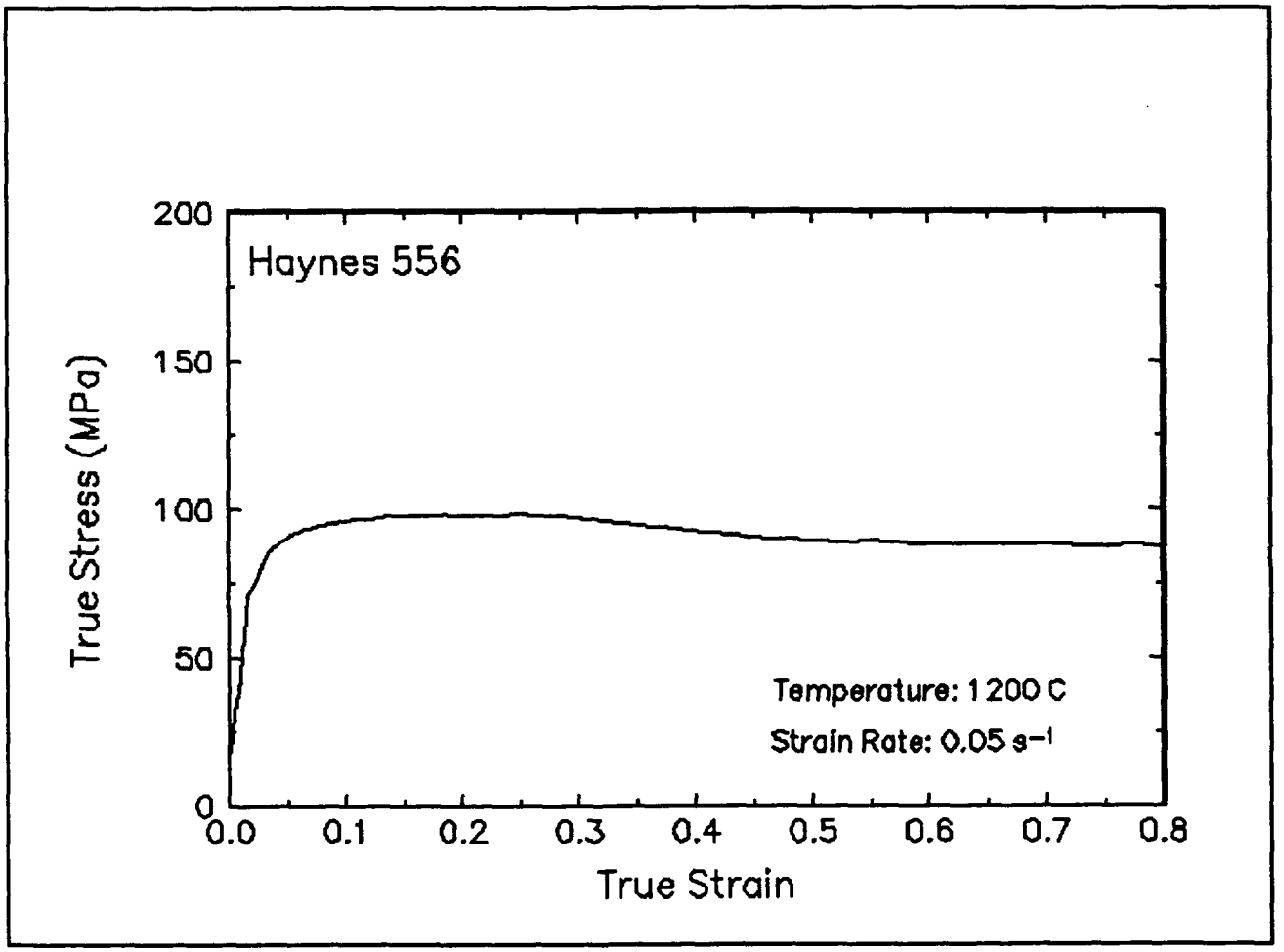

Figure 52. True stress-true strain curve, 1200 C and 0.05 s^{-1}.

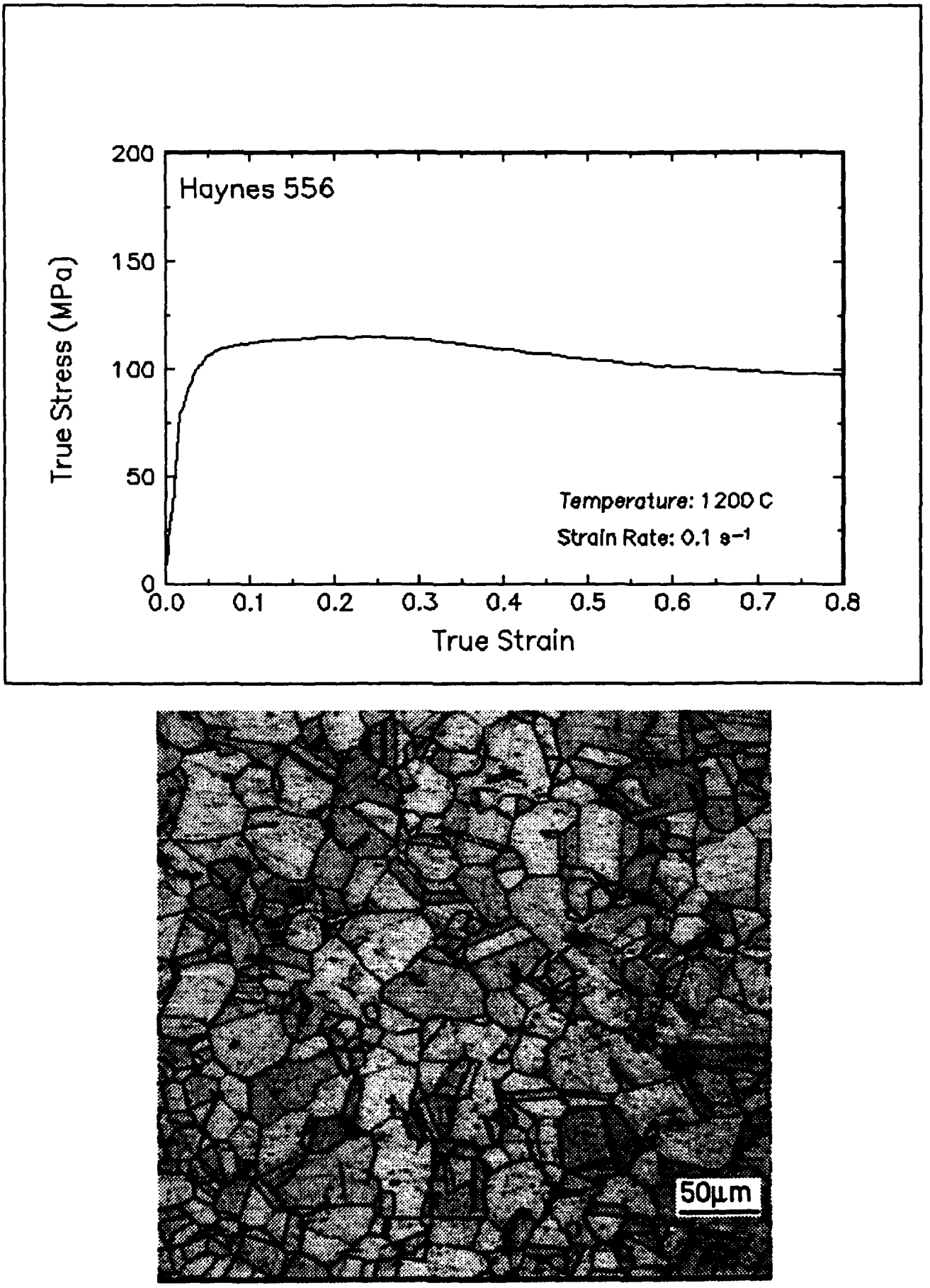

Figure 53. True stress-true strain curve and an optical micrograph from the center of the compressed sample cut through the compression axis, 1200 C and 0.1 s^{-1}.

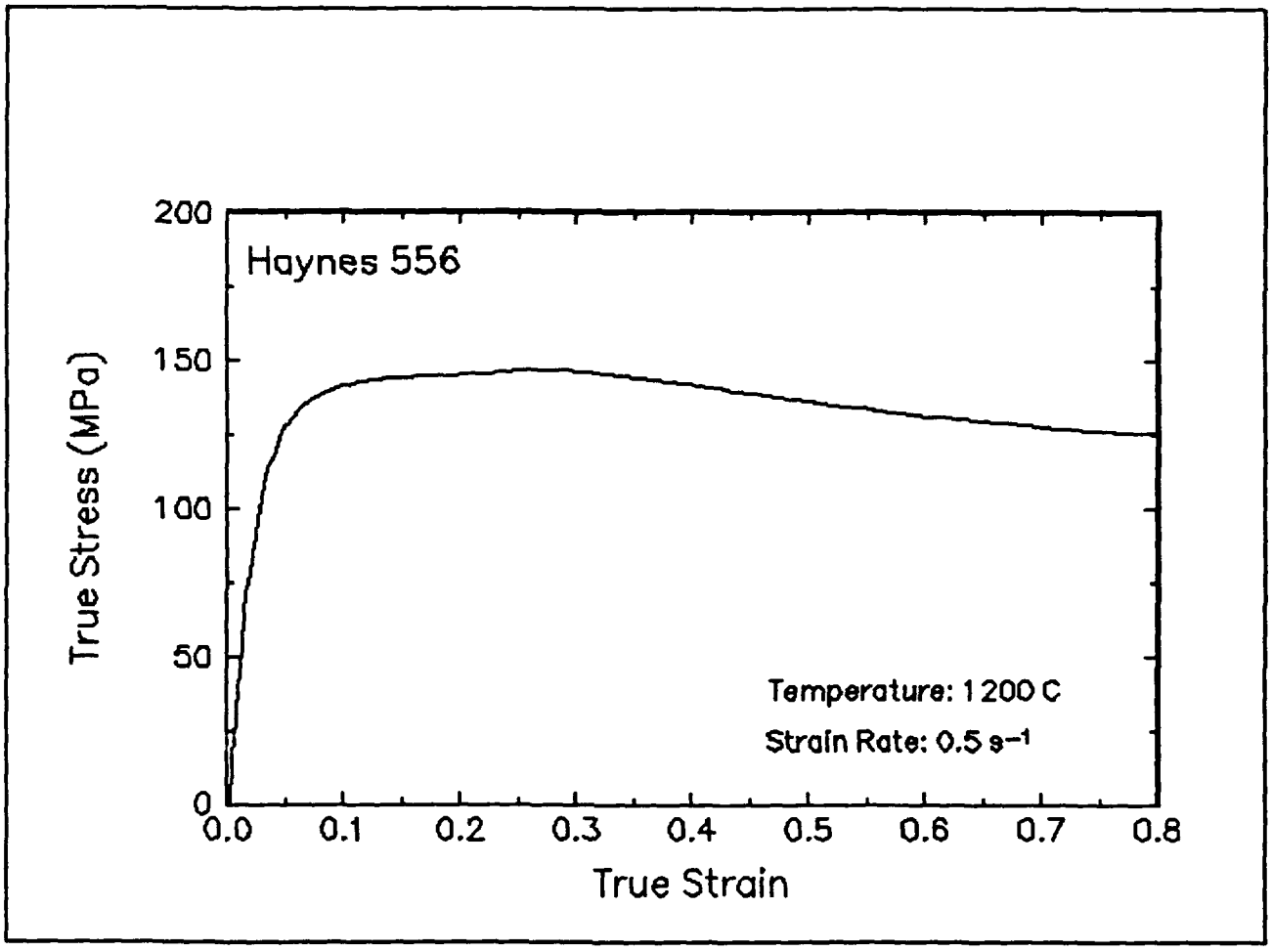

Figure 54. True stress-true strain curve, 1200 C and 0.5 s^{-1}.

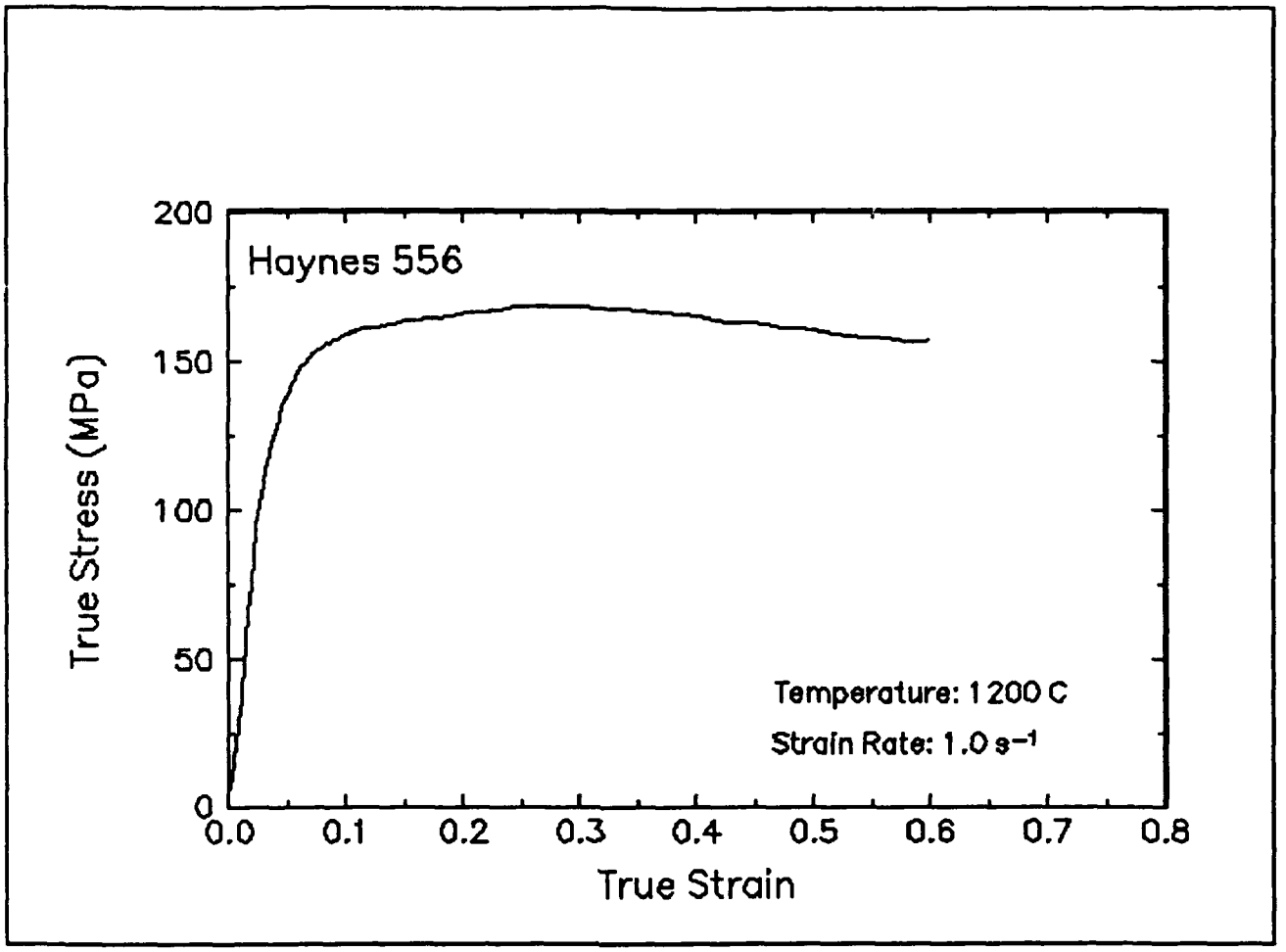

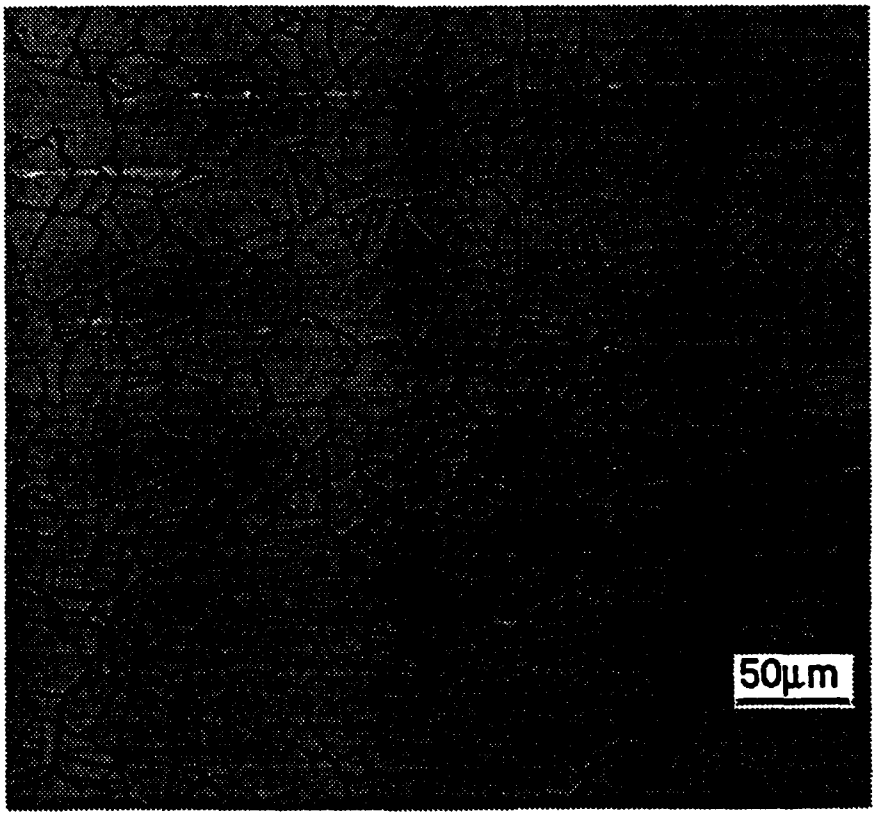

Figure 55. True stress-true strain curve and an optical micrograph from the center of the compressed sample cut through the compression axis, 1200 C and 1 s^{-1}.

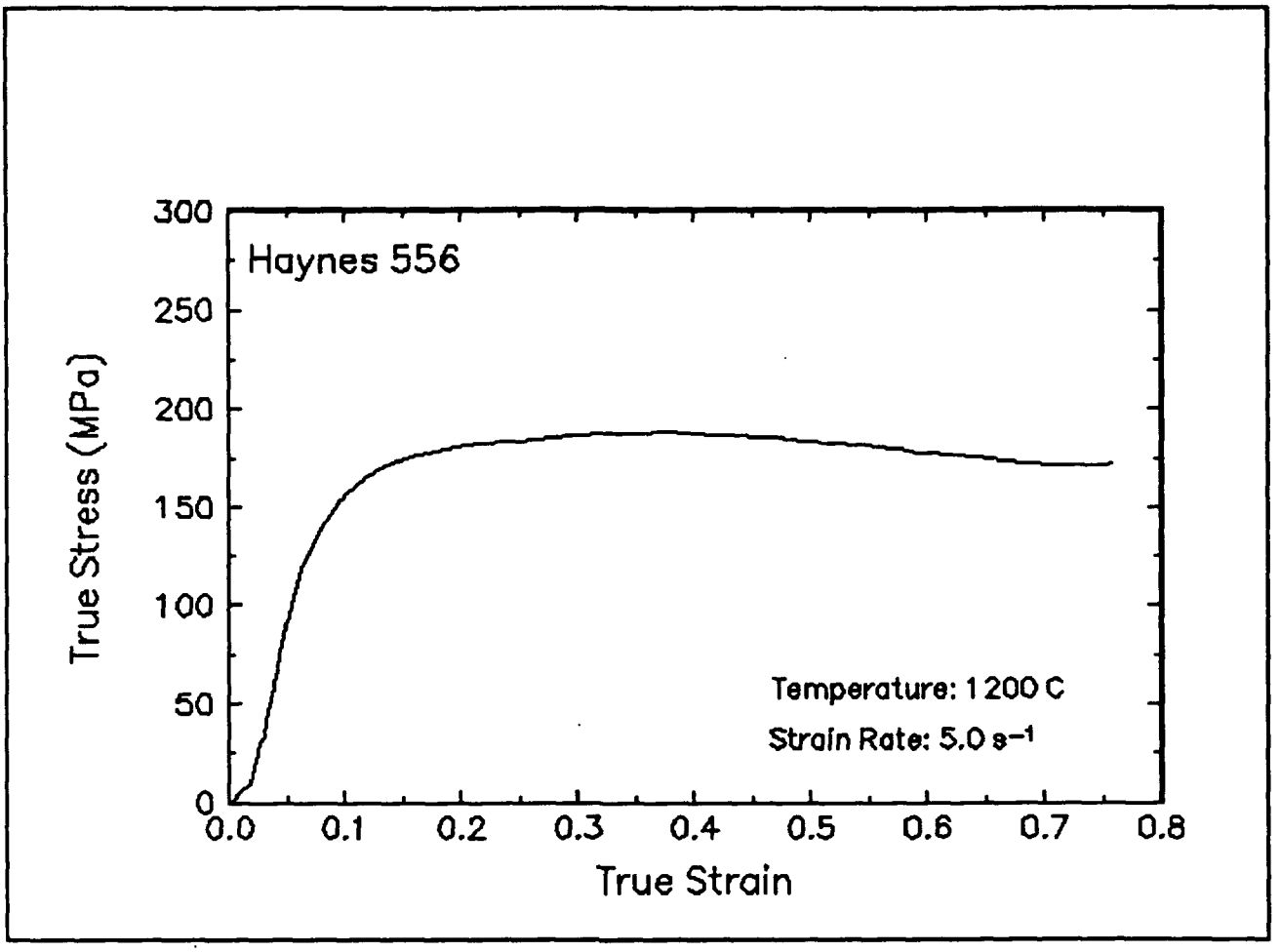

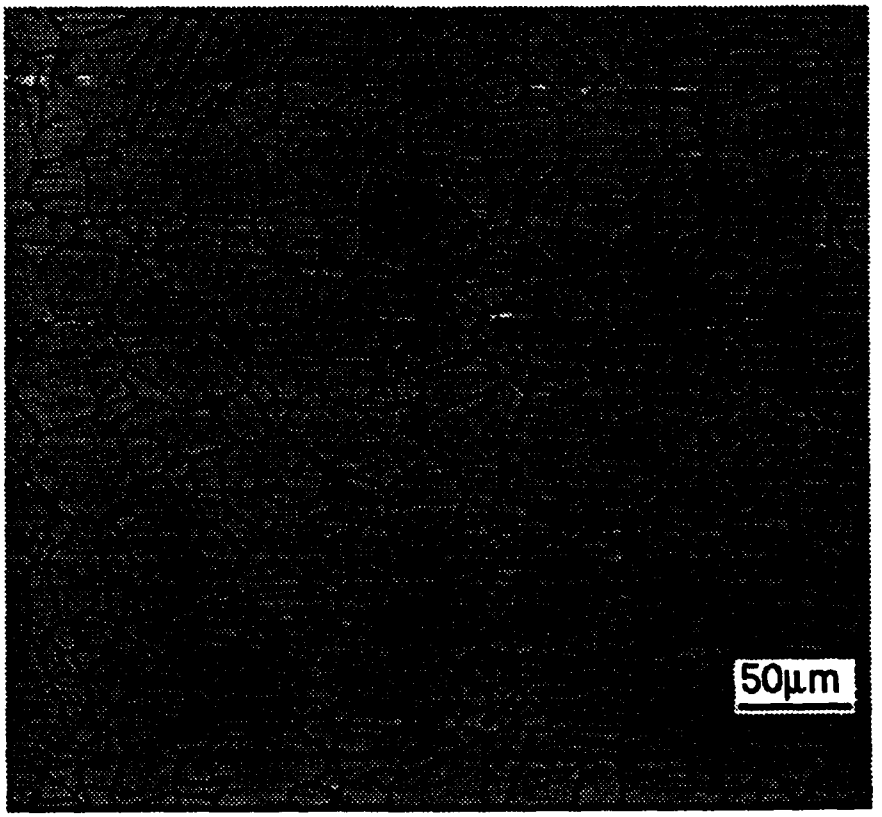

Figure 56. True stress-true strain curve and an optical micrograph from the center of the compressed sample cut through the compression axis, 1200 C and 5 s^{-1}.

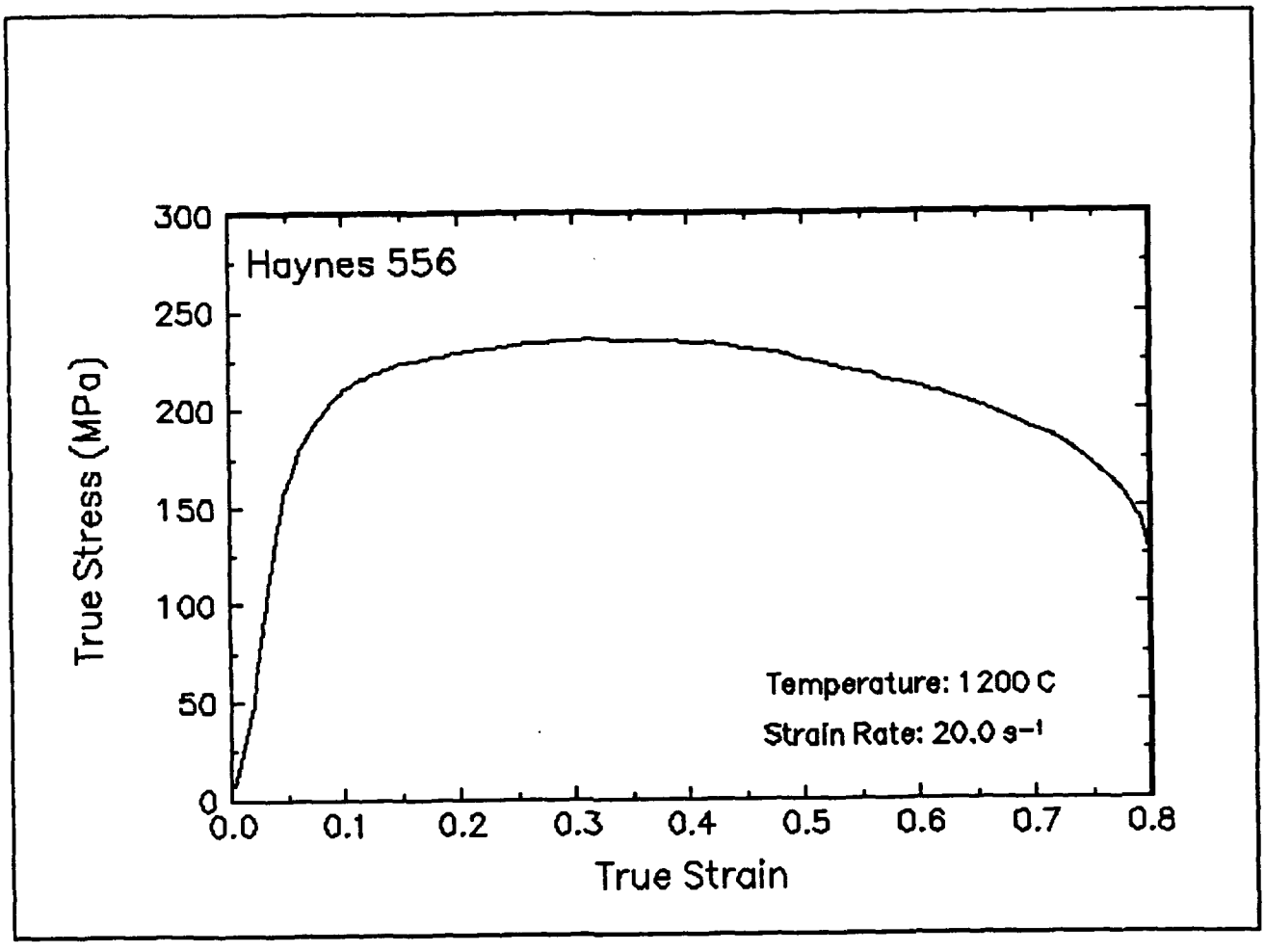

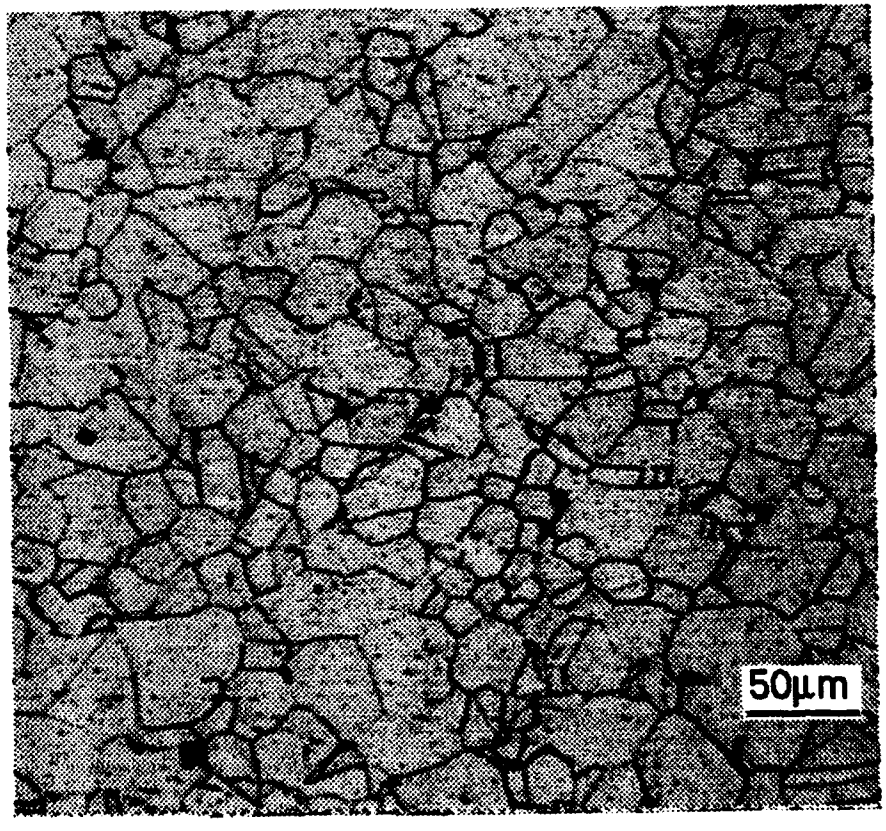

Figure 57. True stress-true strain curve and an optical micrograph from the center of the compressed sample cut through the compression axis, 1200 C and 20 s^{-1}.

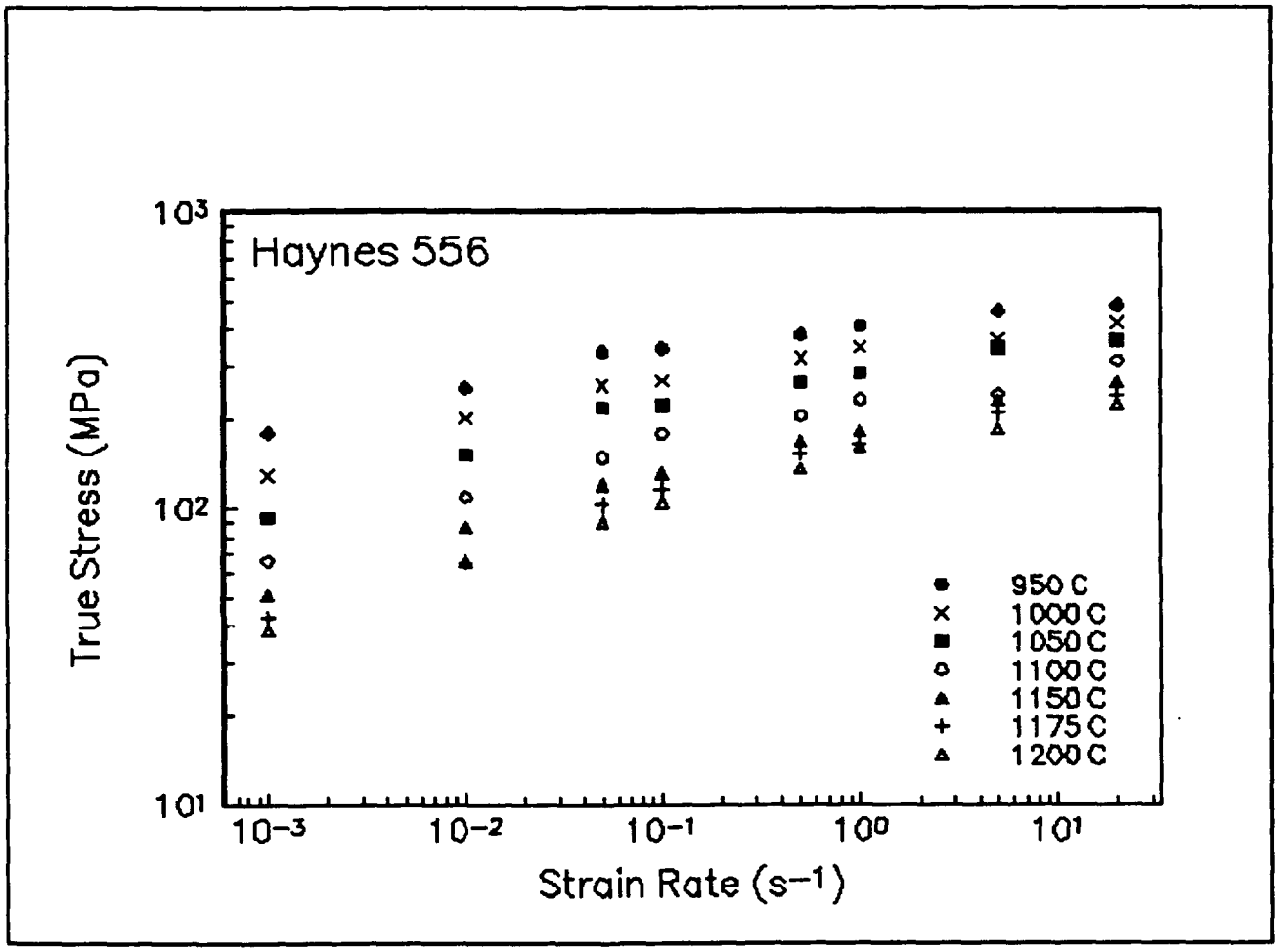

Figure 58. Effect of strain rate on stress in log-log scale at a true strain of 0.5 for Haynes 556.

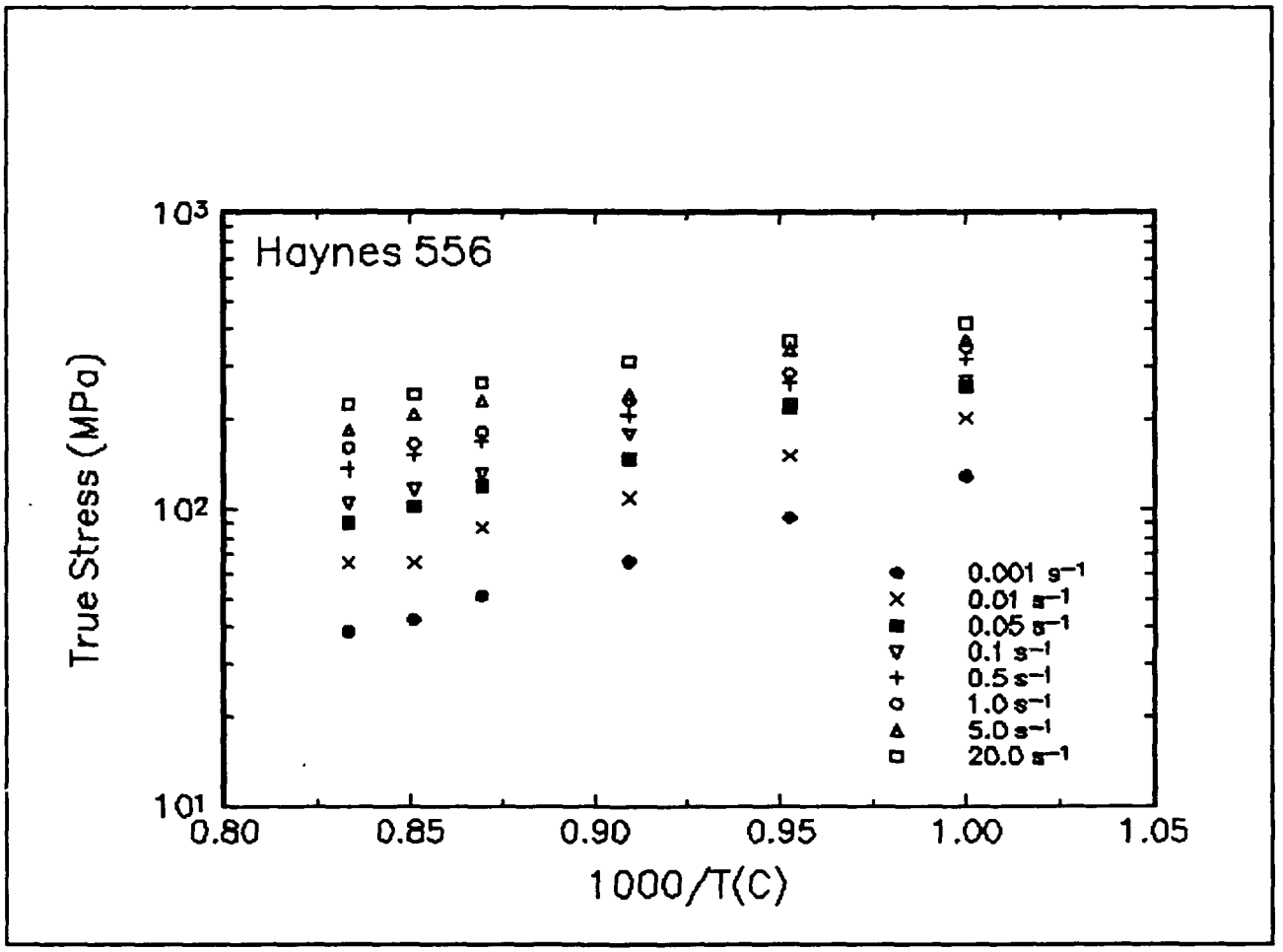

Figure 59. Effect of temperature on stress at a true strain of 0.5 for Haynes 556.

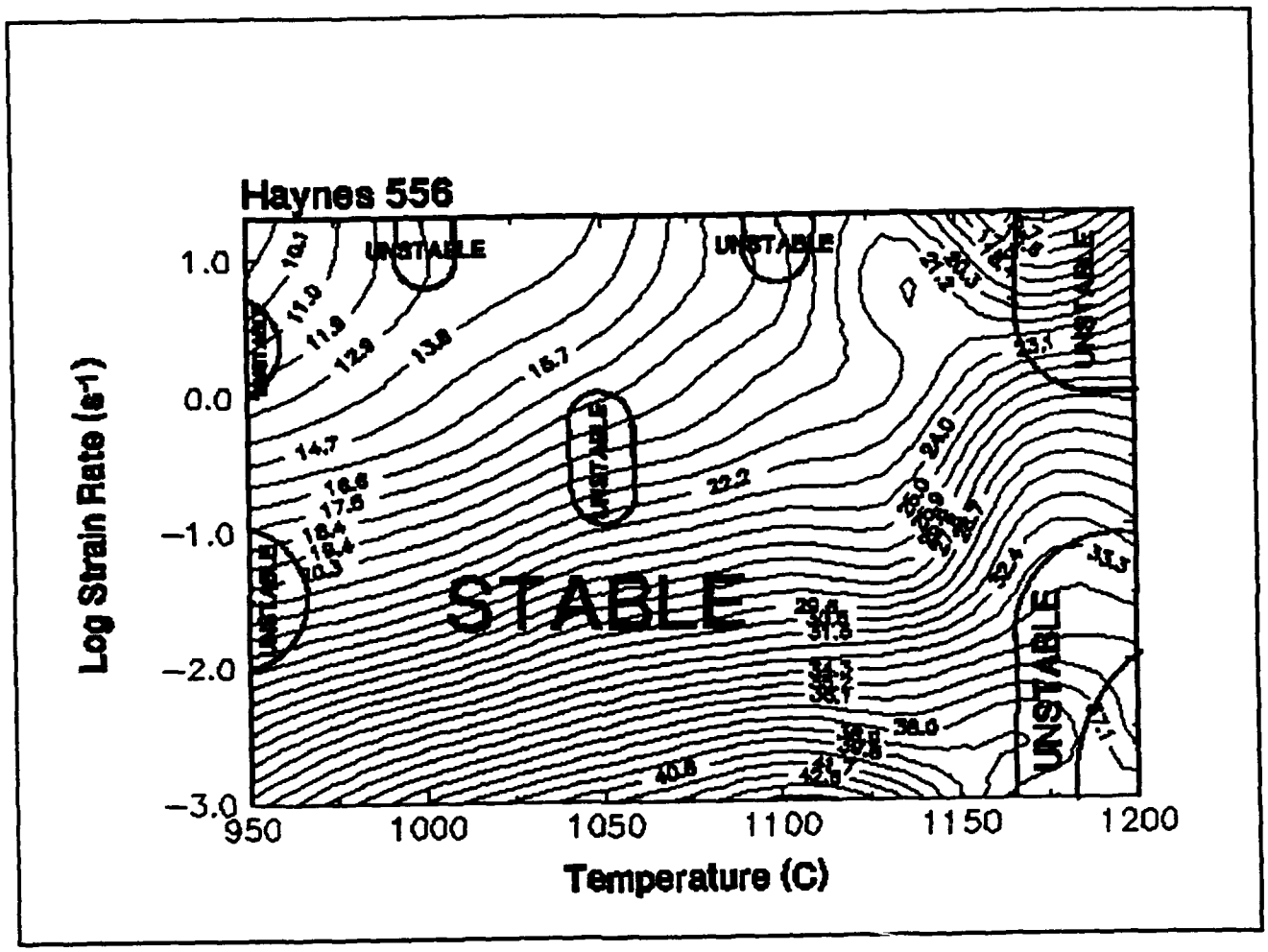

Figure 60. Processing map of Haynes 556 at a true strain of 0.5.

Summary

Compression tests have been performed on Haynes 556 over a wide range of temperatures and strain rates. The experimental conditions used in this work are representative of those used in metalforming practices. From the true stress-true strain curves, the flow behavior was characterized and a processing map indicating the optimum processing condition was generated. This condition is 1106 C and 0.001 s^{-1}.

The deformed microstructures were characterized from the quenched specimens by optical microscopy and are presented for selective testing conditions together with the stress-strain curves.

Implementation of Data Provided by the Atlas of Formability

The Atlas of Formability program provides ample data on flow behavior of various important engineering materials in the temperature and strain rate regime commonly used in metalworking processes. The data are valuable in design and problem solving in metalworking processes of advanced materials. Microstructural changes with temperature and strain rates are also provided in the Bulletin, which helps the design engineer to select processing parameters leading to the desired microstructure.

The data can also be used to construct processing map using dynamic material modeling approach to determine stable and unstable regions in terms of temperature and strain rate. The temperature and strain rate combination at the highest efficiency in the stable region provides the optimum processing condition. A processing map has been developed in this Bulletin. In some metalworking processes such as forging, strain rate varies within the workpiece. An analysis of the process with finite element method (FEM) can ensure that the strain rates at the processing temperature in the whole workpiece fall into the stable regions in the processing map. Furthermore, FEM analysis with the data from the Atlas of Formability can be coupled with fracture criteria to predict defect formation in metalworking processes.

Using the data provided by the Atlas of Formability, design of metalworking processes, dynamic material modeling, FEM analysis of metalworking processes, and defect prediction are common practice in *Concurrent Technologies Corporation*. Needs in solving problems related to metalworking processes can be directed to Dr. Prabir K. Chaudhury, Manager of Forming Department, by calling (814) 269-2594.